NAVAL POSTGRADUATE SCHOOL
Monterey, California

THESIS

FREE ELECTRON AND SOLID STATE LASERS DEVELOPMENT FOR NAVAL DIRECTED ENERGY

by

Aristeidis Kalfoutzos

December 2002

Advisor: William B. Colson
Co-Advisor: Phillip E. Pace

Approved for public release; distribution is unlimited

THIS PAGE INTENTIONALLY LEFT BLANK

REPORT DOCUMENTATION PAGE			Form Approved OMB No. 0704-0188
Public reporting burden for this collection of information is estimated to average 1 hour per response, including the time for reviewing instruction, searching existing data sources, gathering and maintaining the data needed, and completing and reviewing the collection of information. Send comments regarding this burden estimate or any other aspect of this collection of information, including suggestions for reducing this burden, to Washington headquarters Services, Directorate for Information Operations and Reports, 1215 Jefferson Davis Highway, Suite 1204, Arlington, VA 22202-4302, and to the Office of Management and Budget, Paperwork Reduction Project (0704-0188) Washington DC 20503.			
1. AGENCY USE ONLY *(Leave blank)*	**2. REPORT DATE** December 2002	**3. REPORT TYPE AND DATES COVERED** Master's Thesis	
4. TITLE AND SUBTITLE: Free Electron and Solid State Lasers Development For Naval Directed Energy			**5. FUNDING NUMBERS**
6. AUTHOR: Aristeidis Kalfoutzos			
7. PERFORMING ORGANIZATION NAME(S) AND ADDRESS(ES) Naval Postgraduate School Monterey, CA 93943-5000			**8. PERFORMING ORGANIZATION REPORT NUMBER**
9. SPONSORING /MONITORING AGENCY NAME(S) AND ADDRESS(ES) N/A			**10. SPONSORING/MONITORING AGENCY REPORT NUMBER**
11. SUPPLEMENTARY NOTES The views expressed in this thesis are those of the author and do not reflect the official policy or position of the Department of Defense or the U.S. Government.			
12a. DISTRIBUTION / AVAILABILITY STATEMENT Approved for public release; distribution is unlimited			**12b. DISTRIBUTION CODE**

13. ABSTRACT ***(maximum 200 words)***

A MW level FEL is being designed with a short a Rayleigh length resonator to increase the spot size at the mirrors and to avoid mirror damage. In this thesis, it is found that it is desirable to focus the electron beam to improve the FEL extraction efficiency. Three-dimensional simulations show that the focused electron beam increases the extraction efficiency far beyond the required value of 0.7%. It is also found in this thesis that shifting the electron beam off-axis less than 0.3 mm, the efficiency remains above the required value. The proposed FEL design uses high power, short optical pulses whose spectrum may cover many absorption lines. The absorbed laser energy can heat up the air resulting in defocusing the laser beam (thermal blooming). This thesis shows that thermal blooming is not an issue for a moderate clear atmosphere when the stagnation zone size remains less than 10 m. A transitional step for the development of a MW level FEL weapon is the proposed 100 kW upgrade of the Thomas Jefferson National Accelerator Facility's FEL. It has also been shown in this thesis that the use of a step-taper undulator slightly improves the performance of the FEL. Finally, the potential of various high average power solid-state laser designs are reviewed.

14. SUBJECT TERMS Free Electron Laser, Propagation of High Power Free Electron Laser Pulses, Thermal Blooming, Focused Electron and Optical Beams, Desynchronism, Step-taper Undulator, High Power Solid-state Laser			**15. NUMBER OF PAGES** 128
			16. PRICE CODE
17. SECURITY CLASSIFICATION OF REPORT Unclassified	**18. SECURITY CLASSIFICATION OF THIS PAGE** Unclassified	**19. SECURITY CLASSIFICATION OF ABSTRACT** Unclassified	**20. LIMITATION OF ABSTRACT** UL

NSN 7540-01-280-5500 Standard Form 298 (Rev. 2-89)
Prescribed by ANSI Std. 239-18

THIS PAGE INTENTIONALLY LEFT BLANK

Approved for public release; distribution is unlimited

FREE ELECTRON AND SOLID STATE LASERS DEVELOPMENT FOR NAVAL DIRECTED ENERGY

Aristeidis Kalfoutzos
Lieutenant, Hellenic Navy
B.S., Hellenic Naval Academy, 1993

Submitted in partial fulfillment of the
requirements for the degrees of

MASTER OF SCIENCE IN APPLIED PHYSICS
and
MASTER OF SCIENCE IN ELECTRICAL ENGINEERING

from the

NAVAL POSTGRADUATE SCHOOL
December 2002

Author: Aristeidis Kalfoutzos

Approved by:

William B. Colson
Principal Advisor

Phillip E. Pace
Co-Advisor

Joseph Blau
Second Reader

William B. Maier
Chairman, Department of Physics

John P. Powers, Chairman, Department of Electrical and Computer Engineering

THIS PAGE INTENTIONALLY LEFT BLANK

ABSTRACT

A MW level FEL is being designed with a short a Rayleigh length resonator to increase the spot size at the mirrors and to avoid mirror damage. In this thesis, it is found that it is desirable to focus the electron beam to improve the FEL extraction efficiency. Three-dimensional simulations show that the focused electron beam increases the extraction efficiency far beyond the desired value of 0.7%. It is also found in this thesis that shifting the electron beam off-axis less than 0.3 mm, the efficiency remains above the required value. The proposed FEL design uses high power, short optical pulses whose spectrum may cover many absorption lines. The absorbed laser energy can heat up the air resulting in defocusing the laser beam (thermal blooming). This thesis shows that thermal blooming is not an issue for a moderate clear atmosphere when the stagnation zone size remains less than 10 m. A transitional step for the development of a MW level FEL weapon is the proposed 100 kW upgrade of the Thomas Jefferson National Accelerator Facility's FEL. It has also been shown in this thesis that the use of a step-taper undulator slightly improves the performance of the FEL. Finally, the potential of various high average power solid-state laser designs are reviewed.

THIS PAGE INTENTIONALLY LEFT BLANK

TABLE OF CONTENTS

LIST OF FIGURES

LIST OF TABLES

THIS PAGE INTENTIONALLY LEFT BLANK

LIST OF SYMBOLS

$\vec{\mathrm{A}}$	Magnetic vector potential
A_{21}	Einstein coefficient for spontaneous emission
a	Dimensionless optical field
a_o	Initial dimensionless optical field
$\hat{a}$	Peak amplitude of optical field signal
a_r	Cavity losses coefficient
a_b	Absorption coefficient
a_e	Extinction coefficient
$\vec{B}_u$	Undulator magnetic field
$\vec{B}_s$	Optical magnetic field
B	Amplitude of undulator magnetic field
B_{12}	Einstein coefficient for absorption
B_{21}	Einstein coefficient for stimulated emission
$\vec{b}$	Dimensionless relativistic electron velocity
$\vec{b}_\perp$	Dimensionless relativistic electron velocity in the transverse direction
c	Speed of light in vacuum
$c(t)$	Cosine pulse shape function
C_v	Specific heat of air
g	Lorentz factor

$g(f)$ Gain coefficient

d Dimensionless value of desynchronism

df_s Dimensionless value of stagnation zone strength

Δ Step taper rate

$d(t)$ Dirac delta function

e Electron charge

$\vec{E}_s$ Optical electric field

E Amplitude of optical electric field

E_i i-th energy level

$\hat{e}_i$ i-th unit vector

e_n Electron beam emittance

f Frequency

f_o Frequency of optical wave

$f(v)$ Electron phase velocity distribution

f Initial phase of optical wave

F Laser flux density

G Optical field single-pass gain

$G(f)$ Total optical gain

$g_{1,2}$ Degeneracy parameters

$g(f)$ Lineshape function

h Planck's constant

h	Single-pass extraction efficiency
$\hat{h}$	Peak single-pass extraction efficiency
$\hat{I}$	Peak current
$\overline{I}$	Average current
I_f	Optical intensity at frequency f
I_s	Saturation optical intensity
J	Current density
$\vec{J}_\perp$	Transverse current density
j	Dimensionless current density
k	Optical wavenumber
k_o	Undulator wavenumber
K	Undulator parameter
K_e	Kinetic energy of the electron beam
l_e	Electron pulse length
L	Undulator length
l	Optical wavelength
l_o	Undulator wavelength
M	Beam quality factor
m_e	Electron mass
N	Number of undulator periods
N_e	Number of electrons
N_i	Population density of the i-th state

n Index of refraction

$\vec{v}_e$ Electron velocity

v Dimensionless electron phase velocity

v_o Initial dimensionless electron phase velocity

v_c Speed of light in air

P Average optical power

P_R Average optical power of the laser beam after traveling distance R through the atmosphere

P_{crit} Critical power

P_e Electron beam power

$P_a(f)$ Power spectral density function

$\Pi(t)$ Rectangular pulse shape function

Q_n Resonator quality factor

q Electron bunch charge

R Distance

R_i Pumping rate of the i-th state

r Roll-off factor

$\vec{r}_i$ Position of the i-th electron

r_e Electron beam radius

r_c Dimensionless radius of curvature

r_m Dimensionless mirror radius

r	Electron density
$r(f)$	Spectral energy density
s	Optical path
S	Resonator cavity length
s_e	Dimensionless electron beam radius
s_G	Electron phase velocity spread due to Gaussian energy spread
$s_{q_{x,y}}$	Electron phase velocity spread due to Gaussian angular spread in x and y directions
s_z	Dimensionless electron pulse length
$s(f)$	Stimulated emission cross section area
t	Time
T	Optical pulse period
T_1	Half pulse width
T_e	Aerial temperature
t	Dimensionless time
t_w	Dimensionless position of optical waist
t_b	Dimensionless position of electron beam focusing
t_c	Dimensionless position of stagnation zone
t_p	Photon lifetime
V	Volume
w	Dimensionless optical mode radius
W	Optical mode radius

w_o Dimensionless optical waist radius

W_o Optical waist radius

w Angular frequency

w_b Dimensionless betatron frequency

Ω Pulse repetition rate

$\Theta(z)$ Step function

q_n Random phase of the n-th optical micropulse

q_{x_o} Initial electron beam tilt with respect the x-axis

q_{y_o} Initial electron beam tilt with respect the y-axis

q_o Initial electron beam tilt with respect the x-axis and y-axis

y Phase of the optical wave

x, y, z Space coordinates

$\vec{x}$ Unit vector on the xy-plane

y_o Initial electron beam off-axis shift

z_o Dimensionless Rayleigh length

Z_o Rayleigh length

z Dimensionless electron phase

ACKNOWLEDGMENTS

I would first like to thank Professor Bill Colson to whom I am especially grateful for his assistance and guidance throughout this project. I also want to thank Professor Joe Blau for his advice and support. Finally I would like to thank my parents, Loukas and Evangelia, for instilling in me the confidence to pursue my dreams.

THIS PAGE INTENTIONALLY LEFT BLANK

EXECUTIVE SUMMARY

At the Naval Postgraduate School, a high power (MW level) FEL for naval applications is being designed. The proposed FEL uses a short Rayleigh undulator, which increases the spot size of the optical beam at the mirrors and leaves a small optical mode waist in the center of the cavity.

This thesis shows that the small optical mode waist implies that an electron beam shift that is induced vibrationally may reduce the overlap between the electrons and the optical mode in the interaction region and thus result in lower gain and efficiency. Multimode simulations show that the electron beam shift can change the optical wavelength. The peak extraction efficiency steadily decreases as the electron beam is offset further from the undulator axis. But when the electron beam shift is less than 0.3 mm, it is found that the extraction efficiency remains above the goal value of 0.7% for the 1 MW output power. This value of the electron beam shift is well beyond the experimental design tolerance of 0.01 mm shift.

In this thesis the electron beam focusing was also studied, by varying the electron waist radius while keeping the total current fixed. This process improves the overlap between the electron beam and the optical mode and increases the extraction efficiency far beyond the desired value of 0.7%. This indicates that it may be possible to obtain MW operation at a lower average current. The induced electron energy spread is increased slightly but remains within the design goal of 15%.

The proposed FEL uses high power optical micropulses 1 ps long and a pulse repetition frequency of $\Omega = 750$ Mhz. The pulse mode of operation leads to frequency spread depending on the FEL pulse shape in the time domain. The spectrum may cover many absorption lines. The absorbed laser energy heats the air resulting in local modification of the refractive index, and causing defocusing of the laser beam (thermal blooming). It is found that thermal blooming is not an issue for a moderately clear atmosphere when the stagnation zone size remains less than 10 m.

A transitional step for the development of a MW level FEL weapon is the proposed 100 kW upgrade of the Thomas Jefferson National Accelerator Facility's FEL. It has been shown in this thesis that there is a slight improvement in efficiency with the use of a small negative step-tapered undulator, while the induced energy spread stays well below the 15% limit.

The solid-state laser also offers significant potential for a directed energy weapon system. This type of laser has already demonstrated a kW level average output power. However, in order for solid state lasers to realize their potential for directed energy weapons application, technological advances are required in both the supporting technologies and the laser itself. In order to make progress, promising laser designs, such as the fiber, continuously cooled, and heat capacity lasers, must develop independent technologies dealing with the pump process, cost reduction of the diode pump. Laser materials, thermal management, and beam control will play critical roles in the weapon design.

I. INTRODUCTION

The requirement for supporting new warfare concepts over a wide range of missions has prioritized the development and availability of directed-energy weapons (DEW). The potential for a speed-of-light response can add new dimensions and improve numerous aspects of military operations, from initial target detection and identification, to battle damage assessment after the attack. DEW advantages include speed-of-light engagement, high-probability hard kill with unique damage mechanisms and multiple target engagement capability.

An example of a DEW is a high-energy laser. High-energy lasers (HELs) are extremely fast and extremely precise. They begin their attack within seconds of the target's detection and complete its destruction a few seconds later. This enables them to execute multiple shots in order to destroy the target or engage multiple targets. In addition, HELs can engage with smaller bursts of energy as needed for non-lethal attacks, offering the potential of an intermediate response option as a complement to existing weapon systems.

In principle, these weapons can be used in either offensive or defensive applications, though the predominant role has been defensive. The potential missions include ballistic missile defense, air defense, attack against ground and maritime targets, maritime self-defense, space control, urban operations, clearance of exposed mines, surveillance and counter-surveillance. The platforms can be ships, large or tactical aircraft including helicopters, ground vehicles, ground bases and spacecraft.

A laser beam delivers its energy either in a continuous wave mode (CW) or in a pulsed mode to a relatively small spot on the target. The incident intensity can be sufficient to melt through a missile body in a few seconds. Moreover, if the heated area is under stress (aerodynamic or static pressure load), the lethal effects to the target system occur more quickly. The beam aims at specific points of the target's body that are known to be vulnerable such as fuel tanks and aerodynamic control surfaces of a missile.

A HEL weapon system requires more than just a laser device with a specific power level. It also requires command, control, communication and intelligence subsystems, which control and monitor the weapon. The system should be able to provide battle management, including target acquisition, engagement control, kill assessment communication and compatibility with other assets or weapon systems of the carrier unit.

The laser device produces high-energy light at a particular wavelength or small set of wavelengths. Different device technologies will produce widely different power levels and beam quality, which is a measure of how effective the laser is in putting its light into a desired spot size at the target. For HEL weapons, good beam quality is as important as high power. Once the laser has produced high power, the energy must be transmitted to the target. The beam director directs the laser power toward the target in such a way that the laser beam can deliver a lethal intensity on the target. A schematic of the system integration into the host platform of a ship is shown in Figure 1.

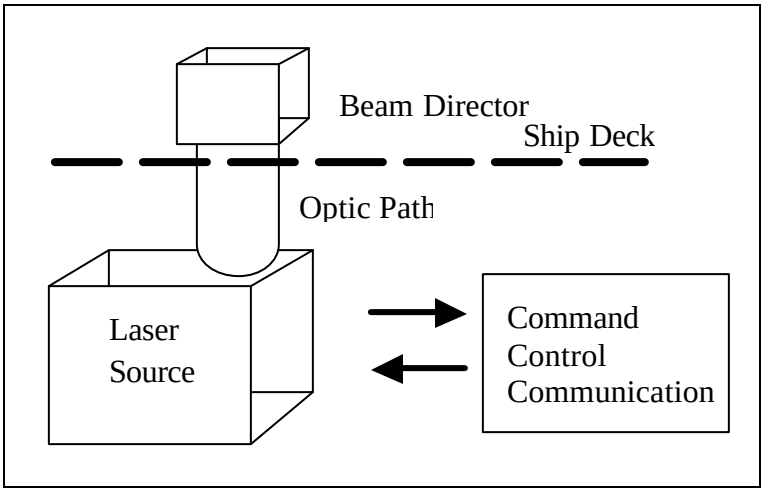

Figure 1. Schematic of a Ship-Based HEL Weapon System. (After [Ref. 1]).

When a laser beam propagates through the atmosphere, molecular constituents and air density fluctuations cause scatter and absorption. Absorption can initiate thermal blooming if the power density is high enough, and air density and thermal gradients can cause turbulence. These effects may attenuate and spread the beam. The effects are typically worse near the surface of the earth than at high altitudes. Figure 2 shows an

example of a maritime environment in which the high-energy laser weapon system has to operate. Nevertheless, three fundamental parameters affect the beam on its way to the target:

- **Wavelength**: Shorter wavelength light is less affected by diffraction but can be more strongly affected by device optical imperfections, turbulence and other atmospheric effects.

Figure 2. A Day at Sea. (From [Ref. 1]).

- **Transmitter diameter**: A large transmitter is able to produce a small spot on the target when the beam is diffraction-limited, and conversely, a small transmitter can produce only a larger spot. Down to a certain target dependent limit, small spots are desirable because they have higher power density and can be more lethal to a target.
- **Range**: The distance of the target from the HEL weapon system is a critical parameter that strongly influences system design. Destruction of distant targets requires much tighter beam control tolerances.

The three kinds of laser devices that are candidates for HEL weapons are:

- **Chemical lasers**. Chemical lasers produce radiation from excited atomic or molecular species resulting from chemical reactions. Weapon class chemical lasers include hydrogen and deuterium fluoride (HF and DF) and chemical oxygen/iodine lasers (COIL). These devices have achieved megawatt power levels with good beam quality. [Ref. 2, 3].

- **Solid-state lasers**. Solid-state lasers produce radiation from excited atomic or ionic species of a solid-state material. The atomic excitation succeeds by providing a power supply to the solid-state material. Solid-state lasers include heat capacity, fibers and continuously-cooled lasers and have produced high average power, at the kilowatt level with good beam quality. [Ref. 2, 3].
- **Free Electron Lasers (FEL).** Free electron lasers produce radiation by passing a relativistic electron beam through an alternating magnetic field. These devices have produced kilowatts of average power with good beam quality. [Ref. 2].

Currently, each of these device types has limitations, such as the limited magazine size of current chemical lasers, the strong thermal management and power supply requirements of current solid-state lasers, and the large size and weight of current free electron lasers.

In the maritime environment, the threats include high speed, high maneuvering anti-ship cruise missiles (ASCMs) and fast attack boats. Navy units are currently able to engage these threats using kinetic kill systems. The effectiveness of these weapons against the potential threat can be severely reduced by the decreased reaction time available, especially in littoral operations. A HEL has the potential to engage over a wide spectrum of threats with precision, accuracy and almost zero reaction time, as shown in Figure 3.

Figure 3. A Ship in Self-Defense Using HEL Weapon Systems. (From [Ref. 3])

Given the electrical power availability on modern navy ships, the FEL and the solid state laser are logical candidates for maritime HEL weapon systems, even though only the chemical lasers have demonstrated weapon-level powers. A significant advantage of FELs and SSLs is that they do not generate the toxic effluents of chemical lasers. The issue of handling the chemical laser on board is serious since the crew could be harmed and equipment damaged. Another disadvantage is the need for a logistics supply of hazardous and toxic chemicals. Furthermore, the chemical lasers are large and heavy, which makes them difficult to exist on a compact configuration.

Chapter II gives an overview of the theoretical background and discusses the physics behind the FEL. Starting from the Lorentz force equation the dimensionless pendulum equation is obtained, which describes the electron phase space evolution. In this way information about the electrons' energy exchange with the optical wave is provided. Additionally, beginning from the Maxwell's wave equation the optical wave equation is obtained. The optical wave equation explains the light wave propagation through the undulator.

Chapter III of this thesis describes the propagation consequences of short pulse free electron lasers. Specifically, the propagation issue of thermal blooming related to the power spread in the frequency domain that is caused by the pulse format of the FEL weapon system will be discussed.

Chapter IV describes the results of simulations for the proposed 1 MW FEL weapon system, using a short Rayleigh length undulator. Three-dimensional simulations are used to study the effects of varying the electron beam radius and angular spread to enhance FEL gain and efficiency. Additionally, the effects of off-axis shifting of the electron beam are studied.

Chapter V presents the simulation results of the upgraded to 100 kW Thomas Jefferson National Accelerator Facility (TJNAF) FEL using a step-tapered undulator.

Chapter VI discusses the physics behind the solid-state lasers and presents their potential to be developed as directed energy weapon systems.

Chapter VII summarizes the results found in the present study.

II. FEL THEORY

A. INTRODUCTION

An FEL is a device that extracts kinetic energy from a relativistic electron beam and converts it into coherent electromagnetic radiation. The radiation can be over a large part of the spectrum, even at wavelengths that conventional sources cannot operate. Therefore, the FEL is an important tool for materials science research, chemical technology, biophysical science, medical, and military applications.

Lasing occurs by sending the relativistic free electrons through a periodic magnetic field called a wiggler or undulator. The wiggler induces transverse forces on the electrons which undergo a wiggling motion as they travel through it. This results in electromagnetic radiation emitted in the forward direction of the electron beam. The wiggler and the radiation can be combined to produce a beat wave, called a ponderomotive wave, that travels slower than the radiation and can be in synchronism with the electrons.

The basic elements of a typical FEL are displayed in Figure 4. The injector generates short periodic bursts of electrons from a photocathode, which is illuminated by a drive laser. Typical peak injector currents are in the range of 1 to 100 amps with pulse widths ranging from 1 to 50 ps [Ref. 2]. The injected electrons are fed into the accelerator, where they are accelerated by an electric field to nearly the speed of light. Thus, the electron obtains kinetic energy,

$$K_e = (g - 1)m_e c^2, \tag{2.1}$$

$$g = \frac{1}{\sqrt{1-(\vec{v}_e/c)^2}} = \frac{1}{\sqrt{1-\vec{b}\cdot\vec{b}}}, \tag{2.2}$$

where g is the Lorentz factor, $\vec{v}_e$ is the electron velocity, c is the speed of light in vacuum, $\vec{b} = \vec{v}_e/c$ is the dimensionless electron velocity, m_e is the electron rest mass, and $m_e c^2 = 0.511$ MeV is the electron rest energy. Typical accelerators operate in the range of 20 MeV to 500 MeV where g ranges from 40 to 1000 [Ref. 2]. The most

common electron accelerators are the radio frequency linear accelerator (RF Linac) and the superconducting RF Linac. The latter operates at the liquid Helium temperature of 2^0K and is used at the Jefferson Lab FEL.

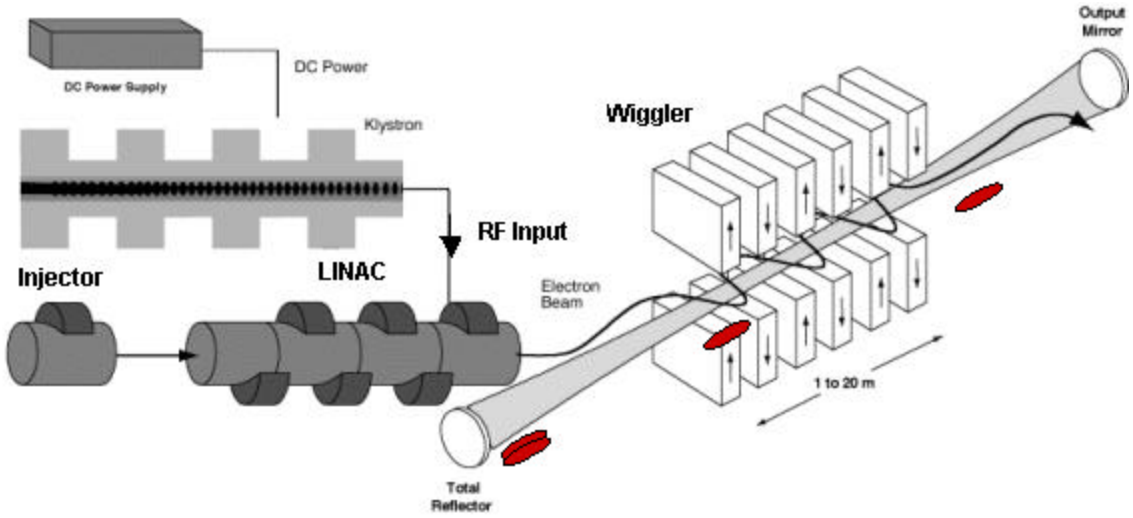

Figure 4. Major FEL Components. (From [Ref. 4]).

The next step is to guide the accelerated electrons into the wiggler with the help of bending magnets. The interaction between the relativistic electron beam and the periodic magnetic field of the wiggler creates and amplifies the optical field. Alternating the polarity of a series of permanent magnets or electromagnets produces the periodic magnetic field. The wiggler is oriented along the *z*-axis, with the magnets parallel to the *y*-axis.

The wiggler is characterized by the dimensionless undulator parameter *K* given by [Ref. 5]

$$K = \frac{eB_{rms}\, l_o}{2p\, m_e c^2}, \tag{2.3}$$

where $l_o = L/N$ is the undulator wavelength, L is the undulator length, N is the number of undulator periods, e is the electron charge magnitude, and B_{rms} is the rms undulator field strength.

Only a small portion of the electron energy is converted to optical energy. When the electron beam exits the wiggler it must either be dumped in a radiation shielded dump or fed back into the accelerator to return its excess energy back to the system. For the latter case, the accelerator is properly phased to decelerate and capture the kinetic energy of the electron beam which can be reused to accelerate other electrons. This process is called energy recovery and is shown in the schematic of the Jefferson Lab FEL oscillator, Figure 5.

The last major component is the resonator cavity. It is oriented along the wiggler axis and consists of an evacuated optical cavity bounded by two mirrors. One of the mirrors is partially transmitting to outcouple optical energy from the FEL. The optical beam is amplified during successive passes through the wiggler, while a fraction of it is allowed to escape. For maximum coupling efficiency between the light and the electrons, the optical beam within the resonator should match the electron beam size.

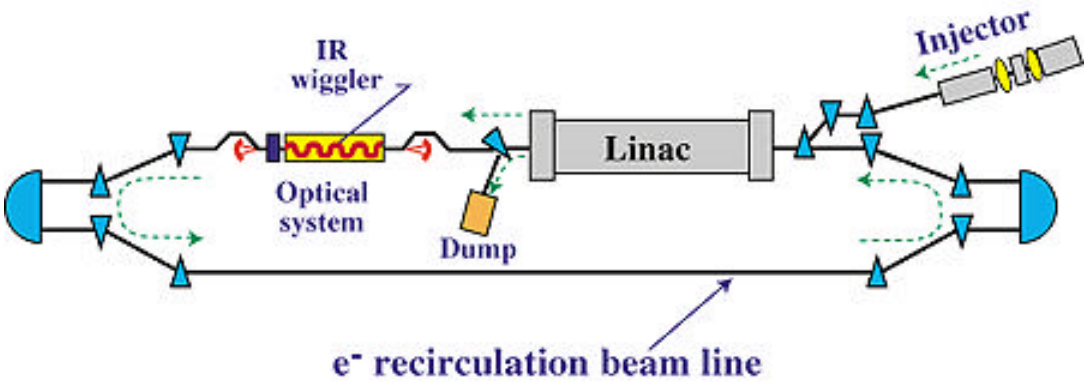

Figure 5. Jefferson Lab Oscillator FEL Using Energy Recovery. (From [Ref. 4])

B. FEL INTERACTION – RESONANCE

The undulator induces small transverse accelerations of the electrons, which results in radiation in the forward direction of the beam. The radiation is a small percentage of the electron energy and has the form of a narrow cone of width on the order of g^{-1} [Ref. 6]. This process is referred to as spontaneous emission and is essential for the start-up of an FEL oscillator.

In the presence of an optical wave, the wiggler mediates the interaction between the electrons and the light. The combination of the relativistic electrons, the magnetic

field of the wiggler and the optical wave produces a ponderomotive wave. This beat wave travels slower than the optical wave and, if it is in resonance with the electrons, there can be energy exchange. The ponderomotive wave, which has the same frequency as the radiation, causes some electrons to speed up and others to slow down. Thus, the ponderomotive wave causes the electrons to bunch. The bunching is critical, as stimulated emission occurs when electrons form coherent bunches within an optical wavelength.

At resonance, the optical wave overtakes the electron beam by one optical wavelength l while the electron travels over one undulator period l_o. Thus, in a given time interval Δt, the light travels a distance

$$l + l_o = c\Delta t, \tag{2.4}$$

while an electron travels

$$l_o = cb_z \Delta t, \tag{2.5}$$

where cb_z is the speed that the electron travels along the undulator z-axis. Combining the last two equations, the optical wavelength is

$$l = \frac{1 - b_z}{b_z} l_o . \tag{2.6}$$

Rewriting Equation (2.2),

$$g^2 = \frac{1}{1 - b^2} = \frac{1}{1 - b_z^2 - b_\perp^2}, \tag{2.7}$$

where $\vec{b}_\perp = \left(b_x, b_{y,} 0\right)$ is the transverse dimensionless electron velocity component. As seen later, the transverse electron velocity can be written

$$\vec{b}_\perp = -\frac{K}{g}(\cos k_0 z, \sin k_0 z, 0) \;\Rightarrow\; b_\perp^2 = \frac{K^2}{g^2} . \tag{2.8}$$

Combining the last three equations, the optical wavelength becomes

$$l = \frac{\frac{1+K^2}{2g^2}}{1-\frac{1+K^2}{2g^2}}\, l_o . \tag{2.9}$$

Since we are dealing with highly relativistic electrons where $g >> 1$ and K is usually on the order of unity, the optical wavelength of the FEL at resonance can be expressed as a function of the undulator period and the energy of the relativistic electron beam as

$$l = \frac{1+K^2}{2g^2}\, l_o \approx \frac{l_o}{g^2}. \tag{2.10}$$

This equation is often referred to as the resonance condition.

C. ELECTRON DYNAMICS

1. Pendulum Equation

This section examines how the ponderomotive wave affects the electron motion through the undulator. Relativistic electrons are injected in the z direction and interact with a helical undulator magnetic field and the fields of a circular polarized optical plane wave, which are described as follows

$$\begin{aligned} \vec{B}_u &= B(\cos k_0 z, \sin k_0 z, 0), \\ \vec{B}_s &= E(\sin y, \cos y, 0), \\ \vec{E}_s &= E(\cos y, -\sin y, 0), \end{aligned} \tag{2.11}$$

where B is the magnetic field amplitude of the undulator, $k_o = 2p/l_o$ is the undulator wavenumber, E is the electric and magnetic field amplitude of the optical wave in cgs units, and y is the phase of the optical wave given by

$$y = kz - wt + f, \tag{2.12}$$

where $k = w/c$ is the optical wavenumber and f is the initial optical phase.

The Coulomb forces between the electrons can be ignored since the beam energy is large. Thus, the total force acting on each electron is approximated by the Lorentz force equation [Ref. 6]

$$\frac{d(g\vec{b})}{dt} = -\frac{e}{m_e c}\left[\vec{E}_s + \vec{b}\times\left(\vec{B}_s + \vec{B}_u\right)\right]. \tag{2.13}$$

Based on the Equation (2.11), the second term in the brackets of the last equation can be written

$$\begin{aligned}\vec{b}\times\left(\vec{B}_s + \vec{B}_u\right) = \hat{x}\left(-Bb_z \sin k_0 z - Eb_z \cos y\right) + \\ \hat{y}\left(Bb_z \cos k_0 z + Eb_z \cos y\right) + \\ \hat{z}\left(Bb_x \sin k_0 z - Bb_y \cos k_0 z + Eb_x \sin y - Eb_y \cos y\right).\end{aligned} \tag{2.14}$$

Then, the *x* component of Equation (2.13) can be written,

$$\frac{d(gb_x)}{dt} = -\frac{e}{m_e c}\left[E\left(1-b_z\right)\cos y - Bb_z \sin k_0 z\right]. \tag{2.15}$$

For relativistic electrons, $b_z \approx 1$ so that $E\left(1-b_z\right) << Bb_z$. So the last equation can be simplified to

$$\frac{db_x}{dt} \approx \frac{eBb_z}{g m_e c}\sin k_0 z\,. \tag{2.16}$$

Following the same steps for the *y* component

$$\frac{db_y}{dt} \approx -\frac{eBb_z}{g m_e c}\cos k_0 z\,. \tag{2.17}$$

The last two equations can be written together as

$$\frac{d\vec{b}_\perp}{dt} \approx -\frac{eBb_z}{g m_e c}\left(-\sin k_0 z, \cos k_0 z, 0\right), \tag{2.18}$$

which by integration verifies Equation (2.8), assuming that the electron injection is perfect so that the constant of integration is zero.

From Equation (2.13), with light present, the electron energy exchange is given by

$$\frac{dg}{dt} = \dot{g} = -\frac{e}{m_e c}\vec{b}\cdot\vec{E}_s = -\frac{e}{m_e c}E\left(b_x \cos y - b_y \sin y\right), \tag{2.19}$$

and by using Equation (2.18), this becomes

$$\dot{g} = \frac{eKE}{m_e cg}\cos\left(k_o z + y\right) = \frac{eKE}{m_e cg}\cos\left(z + f\right), \tag{2.20}$$

where $z = \left(k + k_o\right) z - wt$ is defined as the electron phase with respect to the ponderomotive wave. By differentiating the electron phase twice, a relation for the time derivative of the fractional electron velocity in *z* direction is obtained,

$$\dot{z} = \left(k + k_o\right) \dot{z} - w = \left(k + k_o\right) b_z c - w, \tag{2.21}$$

$$\ddot{z} = \left(k + k_o\right) \dot{b}_z c \;\Rightarrow\; \dot{b}_z = \frac{\ddot{z}}{\left(k + k_o\right) c}. \tag{2.22}$$

Combining Equations (2.7) and (2.8) and then taking the time derivative on both sides, we obtain

$$g^{-2}\left(1 + K^2\right) = 1 - b_z^2 \;\Rightarrow\; \frac{\dot{g}}{g} = \frac{g^2 b_z \dot{b}_z}{1 + K^2}. \tag{2.23}$$

Inserting Equation (2.22) into Equation (2.23) we find

$$\frac{\dot{g}}{g} = \frac{g^2 b_z \ddot{z}}{\left(1 + K^2\right)\left(k + k_o\right) c}, \tag{2.24}$$

and since we are dealing with relativistic electrons where $b_z \approx 1$ and $k >> k_o$ this becomes

$$\frac{\dot{g}}{g} = \frac{g^2 \ddot{z}}{\left(1 + K^2\right) kc} = \frac{l g^2 \ddot{z}}{\left(1 + K^2\right) 2pc}. \tag{2.25}$$

This can be simplified further by using Equation (2.10) near resonance so that Equation (2.25) becomes

$$\frac{\dot{g}}{g} = \frac{l_o \ddot{z}}{4p\, c}. \tag{2.26}$$

Finally, combining with Equation (2.22) and solving for the second derivative of the electron phase gives

$$\ddot{z} = \frac{2w_o eKE}{m_e c g^2}\cos\left(z + f\right). \tag{2.27}$$

Equation (2.27) has the form of a simple pendulum equation and represents the electron phase dynamics. This can be simplified further by introducing the dimensionless time $t \equiv ct/L$ and the dimensionless derivatives $\overset{\circ}{(...)} = d(...)/dt$,

$$\overset{\circ}{v} = \overset{\circ\circ}{z} = |a|\cos(z + f), \tag{2.28}$$

where $|a| = 4p\,NKLE/g^2 m_e c^2$ is the dimensionless optical field amplitude [Ref. 5] and v is the dimensionless electron phase velocity

$$v = \overset{\circ}{z} = L\left[(k + k_0)b_z - k\right]. \tag{2.29}$$

For $v = 0$ we have exact resonance as shown in Equation (2.6).

At resonance, b_z can be written as

$$b_z = 1 - \frac{1 + K^2}{2g^2} \ . \tag{2.30}$$

Substituting b_z into Equation (2.29) and differentiating, a change in phase velocity Δv related to a change in electron energy Δg is

$$\Delta v = 4p\,N\left(\frac{\Delta g}{g}\right). \tag{2.31}$$

The FEL pendulum equation is used to describe the microscopic motion of each electron over an optical wavelength. The cosine term determines whether each electron gains or loses energy. The electrons with phase in the range $[-p/2, p/2]$ absorb energy from the optical field and speed up, while those with phase in the range $[p/2, 3p/2]$ transfer energy to the optical field and slow down. This results in electron bunching in each optical wavelength. The other factor of pendulum equation, the dimensionless optical field strength, expresses the rate of the electron bunching. For $|a| >> p$, the optical field is strong and the bunching occurs quickly, while for $|a| << p$, the optical field is weak and the change of the electron phase is small.

2. Extraction Efficiency

The single-pass extraction efficiency h of an FEL can be defined as the fraction of the electron beam energy converted to laser light during one passage through the undulator,

$$h = -\frac{\langle \Delta g \rangle m_e c^2}{g\, m_e c^2} = -\frac{\langle \Delta g \rangle}{g}, \tag{2.32}$$

where $\langle \Delta g \rangle$ represents the average energy change of all the electrons after a single pass through the undulator.

From Equations (2.31) and (2.32), the extraction efficiency can be expressed as the change of the average electron phase velocity $\langle \Delta v \rangle$ over a single pass through the undulator,

$$h = -\frac{\langle \Delta v \rangle}{4p\, N} \ . \tag{2.33}$$

For a typical FEL the change of the average electron phase velocity is $\langle \Delta v \rangle \approx 2p$, so the single pass extraction efficiency becomes $h \approx 1/2N$.

D. OPTICAL WAVE EQUATION

The light wave propagation through the undulator is described by Maxwell's wave equation in the Coulomb gauge,

$$\left(\nabla^2 - \frac{1}{c^2}\frac{\partial^2}{\partial t^2} \right) \vec{\mathrm{A}} = -\frac{4p}{c} \vec{J}_\perp , \tag{2.34}$$

where $\vec{J}_\perp$ is the transverse current density. The vector potential $\vec{\mathrm{A}}$ is related to the circularly polarized plane optical wave of Equation (2.11) by

$$\vec{B}_s = \vec{\nabla} \times \vec{\mathrm{A}} , \tag{2.35}$$

and can be written as a function of z and t as

$$\vec{\mathrm{A}}(z,t) = \frac{E(z,t)}{k} (\sin y , \cos y , 0). \tag{2.36}$$

Making the assumption that the amplitude and the phase of the optical field are slowly varying both in time and space over an optical wavelength, then

$$\begin{aligned} \frac{\partial E}{\partial t} &<< wE, \quad \frac{\partial f}{\partial t} << wf, \\ \frac{\partial E}{\partial z} &<< kE, \quad \frac{\partial f}{\partial z} << kf, \end{aligned} \tag{2.37}$$

and Equation (2.34) can be simplified to

$$2\left(\frac{\partial E}{\partial z}+\frac{1}{c}\frac{\partial E}{\partial t}\right)(\cos y,-\sin y,0)-2E\left(\frac{\partial f}{\partial z}+\frac{1}{c}\frac{\partial f}{\partial t}\right)(\sin y,\cos y,0)\approx-\frac{4p}{c}\vec{J}_{\perp},$$

or,

$$\begin{aligned} \left(\frac{\partial E}{\partial z}+\frac{1}{c}\frac{\partial E}{\partial t}\right) &\approx -\frac{2p}{c}\vec{J}_{\perp}\cdot\hat{e}_1, \\ \left(\frac{\partial f}{\partial z}+\frac{1}{c}\frac{\partial f}{\partial t}\right)E &\approx \frac{2p}{c}\vec{J}_{\perp}\cdot\hat{e}_2, \end{aligned} \tag{2.38}$$

where $\hat{e}_1,\hat{e}_2$ are defined as unit vectors,

$$\begin{aligned} \hat{e}_1 &= (\cos y,-\sin y,0), \\ \hat{e}_2 &= (\sin y,\cos y,0). \end{aligned} \tag{2.39}$$

The transverse current can be expressed as the sum of each electron charge having transverse velocity $b_{\perp}c$

$$\vec{J}_{\perp}=-ec\sum_i \vec{b}_{\perp}d^3\left(\vec{x}-\vec{r}_i\right)=ec\sum_i\frac{K}{g}(\cos k_o z,\sin k_o z,0)d^3\left(\vec{x}-\vec{r}_i\right), \tag{2.40}$$

where $\vec{r}_i$ is the position of the i-th electron. If the number of undulator periods is assumed to be large, we can replace the summation over all the electrons with the volume element electron density r multiplied by the average phase of the electrons in that volume element. Then, from the last two equations, we obtain

$$\begin{aligned} \vec{J}_{\perp}\cdot\hat{e}_1 &= \frac{ecKr}{g}\left\langle\cos\left(y+k_o z\right)\right\rangle, \\ \vec{J}_{\perp}\cdot\hat{e}_2 &= \frac{ecKr}{g}\left\langle\sin\left(y+k_o z\right)\right\rangle, \end{aligned} \tag{2.41}$$

where the notation $\langle ... \rangle$ corresponds to an average over all the electrons as before.

Now, combining Equations (2.38) and (2.41) using $z + f = y + k_o z$ gives a complex form of the optical wave equation

$$\left(\frac{\partial}{\partial z} + \frac{1}{c}\frac{\partial}{\partial t} \right) E e^{if} = -\frac{2p\, eK\, r}{g} \left\langle e^{-iz} \right\rangle . \tag{2.42}$$

For the case of a long FEL electron pulse, there is no spatial dependence in the *z* direction and the last equation simplifies to

$$\frac{1}{c}\frac{\partial}{\partial t} E e^{if} = -\frac{2p\, eK\, r}{g} \left\langle e^{-iz} \right\rangle ,$$

which by using dimensionless variables takes the final form of

$$\overset{\circ}{a} = \frac{d\left(|a| e^{if} \right)}{dt} = -j \left\langle e^{-iz} \right\rangle , \tag{2.43}$$

where $|a| = 4p\, NKLE / g^2 m_e c^2$ is the dimensionless optical field amplitude, and $j = 8N \left(ep\, KL \right)^2 r / g^3 m_e c^2$ is the dimensionless electron beam current.

Equation (2.43) is known as the FEL optical wave equation. This equation expresses the dependence of the rate of change in the optical field with the dimensionless current and the average electron phase changes.

E. PHASE SPACE ANALYSIS

The phase space evolution of sampled electrons can be used to describe the motion of the electrons within an optical wavelength. A change in electron phase velocity is related to a change in electron energy. Therefore, the phase space evolution plot can provide information about the electrons' energy exchange with the optical wave.

The pendulum equation, which describes the electron phase space evolution, and the optical wave equation are coupled together through the dimensionless current density j. If $j < p$, the FEL gain is low, and if $j >> p$, the FEL gain is high. The phase space evolution can be obtained by solving these two equations numerically for a sample number of electrons.

Suppose a sample of electrons from a monoenergetic electron beam is injected into the undulator with a uniformly distributed initial phase z_o from $-p/2$ to $3p/2$. Moreover, the sample electrons are injected at resonance $(v_o = 0)$, and the electron beam has low current $(j = 1)$ at the upper limit of the weak field regime where $a_o \approx p$. Thus, at the beginning of the undulator $(t = 0)$, the initial conditions for the electron phase z_o and the phase velocity v_o are,

$$\begin{aligned} z[i] &= -\frac{p}{2} + i\frac{2p}{N_e}, \\ v[i] &= v_o = 0, \end{aligned} \tag{2.44}$$

where the index *i* indicates the *i*-th electron of the total N_e sample electrons. Now integration of the pendulum Equation (2.28) gives the phase space evolution in (z, v) of the sample electrons.

The electron evolution in the phase-space plane is shown in Figure 6. The electrons appear as colored dots and their evolution is denoted by the change of the color from yellow $(t = 0)$ to red $(t = 1)$. For this case, they follow closed orbits inside the separatrix, which is defined by $v_s^2 = 2|a|[1 + \sin(z_s + f)]$ [Ref. 5]. The sample electrons with initial phase z_o between $[-p/2, p/2]$ gain energy from the optical field and move up in phase velocity $(v > v_o)$, while an equal number of electrons with initial phase between $[p/2, 3p/2]$ transfer some of their energy to the optical field and move down in phase velocity $(v < v_o)$. This results in a bunching near the relative phase $z = p/2$ and a zero net energy transfer to the optical field. This is also obvious on the top right plot of the same figure, which indicates the optical gain $G(t)$ evolution. The gain at time t is defined as

$$G(t) = \frac{P(t) - P(t = 0)}{P(t = 0)}, \tag{2.45}$$

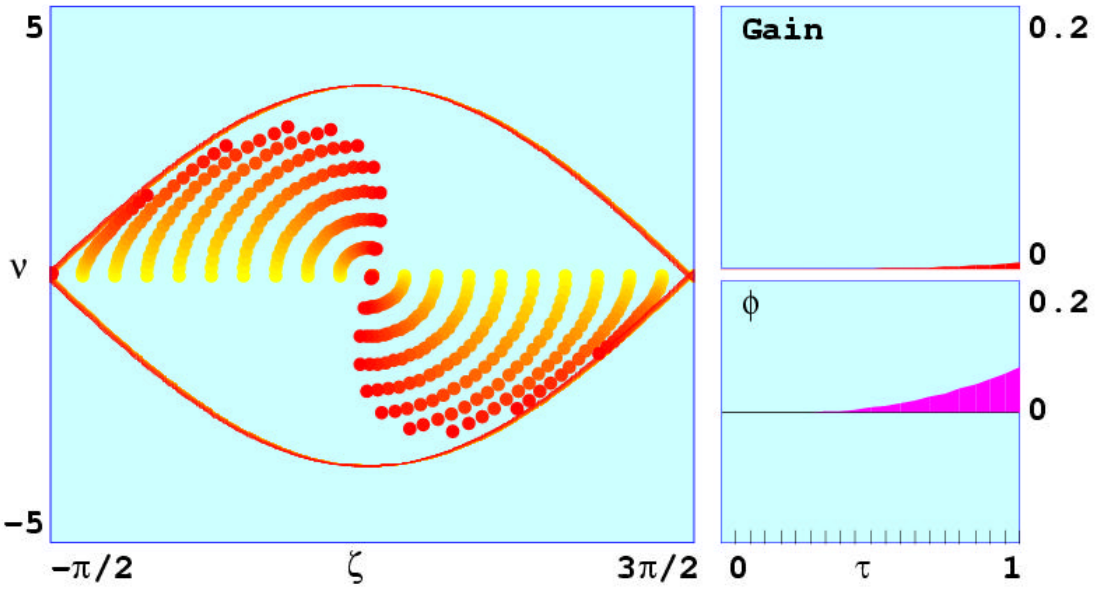

Figure 6. Phase-Space Electron Evolution at Resonance.

where $P(t) \propto |a(t)|^2$ is the optical power at time t, and $P(t=0) \propto a_o^2$ is the initial optical power. Furthermore, the gain in the weak field, low current regime can be expressed as a function of the dimensionless current j and the initial velocity v_o [Ref. 5]

$$G(t) = j\frac{2-2\cos(v_o t) - v_o t \sin(v_o t)}{v_o^3}. \tag{2.46}$$

The last plot of Figure 6 shows the optical phase evolution $f(t)$.

The final gain spectrum at $t = 1$, during one passage through the undulator for $j = 1$, versus the initial velocity v_o, is shown in Figure 7. The horizontal axis of v_o can be considered a function of the electron beam energy Δg, given by Equation (2.31) and centered about the resonant energy $g = \left[l_o\left(1+K^2\right)/2l \right]^{1/2}$, or a function of the optical wavelength $\Delta l = l\Delta v_o / 2pN$ centered about the resonant wavelength given by Equation (2.10). The gain plot indicates that the gain spectrum is anti-symmetric about $v_o = 0$ and

shows that for a resonant electron beam there is a zero net energy transfer to the optical field.

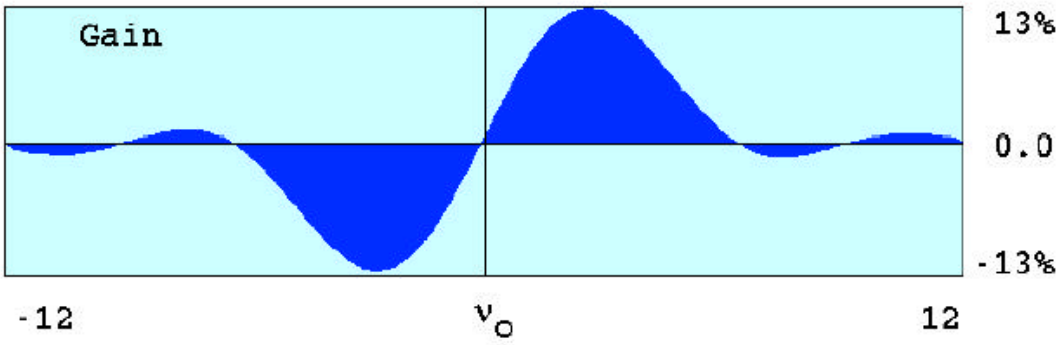

Figure 7. Weak Field Low Current Gain Spectrum.

In addition, the same plot indicates that the maximum gain (13%) for $j = 1$ is achieved slightly above resonance at $\nu_o = 2.6$, while the maximum loss for the optical field occurs for $\nu_o \approx -2.6$.

The electron evolution in the phase-space plane for an electron beam injected at $\nu_o = 2.6$ is shown in Figure 8. Now, the electrons above the separatrix follow open orbits. At the end of the undulator, the electrons tend to bunch near $z = p$ and the majority of them move down in phase velocity losing energy. This results in a net energy transfer to the optical field. The top right gain evolution plot shows significant energy exchange to the light wave, where the gain has reached the value of 13%.

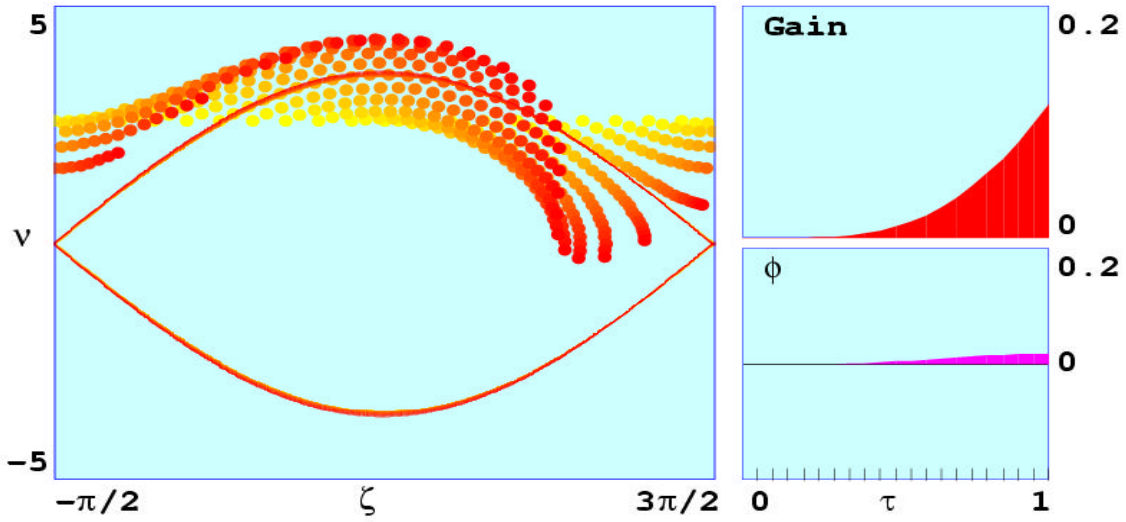

Figure 8. Phase-Space Electron Evolution with Electrons Injected Slightly Above Resonance at $v_o \approx 2.6$.

F. SHORT PULSES

The resonance condition states that the optical wave overtakes the electron beam by one optical wavelength l over one undulator period l_o. At the end of the undulator, the light wave will be ahead of an electron by Nl, which is called the slippage distance. The pulses are defined as short pulses in the case where the electron pulse length is comparable to or less than the slippage distance.

Due to spontaneous emission, short optical pulses are produced that bounce between the mirrors. The FEL interaction takes places between the stored optical pulse bouncing between mirrors and every new electron pulse coming into the undulator. The optical pulse and the electron pulse may enter the undulator simultaneously at exact synchronism. Otherwise, any displacement between these two pulses defines the desynchronism *d*.

Suppose a short electron pulse, with the pulse length of the order of the slippage distance, enters the undulator in exact synchronism with the optical pulse. Since the relativistic electrons travel slightly slower than the speed of light, the optical pulse will be ahead of the electron pulse by Nl at the end of the undulator. Consequently, the light amplification occurs mostly for the trailing portion of the optical pulse, which makes the

centroid of the optical pulse travel slower than the speed of light. After some oscillations, the optical pulse falls behind the electron pulse and no interaction takes place. Finally, the optical power starts to decay due to the cavity loses and the FEL becomes unstable.

This process can be overcome if the optical pulse arrives slightly before the electron pulse at the beginning of the undulator. By adjusting the mirrors position using a piezoelectric crystal, the path inside the cavity can be reduced by ΔS. The displacement of the mirrors relative to the slippage distance is the desynchronism, defined by $d = -2\Delta S / Nl$. Typical values for peak steady-state power are $d \approx 0.01$.

Less power but more stability is obtained by further increasing desynchronism. The final optical pulse width will be longer than the electron pulse, which leads to a narrower power spectral density. For even larger values of desynchronism $(d >> 0.1)$, there will not be sufficient overlap between the two pulses and consequently, the FEL steady-state power decreases to zero.

G. DIFFRACTION

Now suppose that the amplitude of the optical electric field additionally has *x* and *y* dependence. The optical vector potential of Equation (2.36) can be written as

$$\vec{A}\left(\vec{x},t\right) = \frac{\vec{E}\left(\vec{x},t\right)}{k}\left(\sin y, \cos y, 0\right). \tag{2.47}$$

Beginning again with Maxwell's wave equation in the Coulomb gauge and following the same steps as in paragraph D, we obtain

$$\left[\frac{1}{2}\vec{\nabla}_{\perp} + ik\left(\frac{\partial}{\partial z} + \frac{1}{c}\frac{\partial}{\partial t}\right)\right]Ee^{if} = -\frac{2p\,eKr}{g}\left\langle e^{iz}\right\rangle, \tag{2.48}$$

where $\vec{\nabla}_{\perp} = \frac{\partial^2}{\partial x^2} + \frac{\partial^2}{\partial y^2}$.

Now, we introduce the dimensionless time, $t = z/L \approx ct/L$, and normalize the transverse coordinates *x* and *y* to the characteristic mode radius, $\sqrt{Ll/p}$. The wave Equation (2.48) takes the form of the parabolic wave equation, where the optical wave is driven by the dimensionless electron beam current

$$\left[-\frac{i}{4}\vec{\nabla}_{\perp}^{2}+\frac{\partial}{\partial t}\right]a(x,y,t)=-j\left\langle e^{-iz}\right\rangle. \tag{2.49}$$

The operator $-\vec{\nabla}_{\perp}^{2}\, i/4$ describes the diffraction of the optical beam. In the case where the optical beam propagates in free space, $j=0$ and Equation (2.49) becomes the parabolic wave equation for free space

$$\frac{\partial a(x,y,t)}{\partial t}=\frac{i}{4}\vec{\nabla}_{\perp}^{2}a(x,y,t), \tag{2.50}$$

where the dimensionless time $t=(z/R)=0\rightarrow 1$ is now the time of evolution of the wavefront along the range *R*. Equation (2.50) indicates that the diffraction is important when $(\Delta t/4\Delta x^{2})\rightarrow 1$, where Δx represents a structure size of the wavefront. Over the full range *R*, $\Delta t=1$, a large size wavefront $(\Delta x\geq 1/2)$ will not be severely affected by diffraction, while a wavefront with a small size $(\Delta x\leq 1/2)$ will be affected by diffraction.

1. Rayleigh Length

A solution of Equation (2.50) determines the fundamental optical mode inside the laser cavity. Typically, the fundamental mode has a Gaussian shape and is determined by the cavity mirrors. If W_o is the radius of the Gaussian optical mode waist, then

$$Z_o\, l=p\,W_o^{2}, \tag{2.51}$$

where Z_o is the characteristic spread distance called the Rayleigh length. As the beam propagates along *z*, the spot size $W(z)$ becomes larger in accordance with

$$W^{2}(z)=W_o^{2}\left[1+\left(\frac{z}{Z_o}\right)\right]. \tag{2.52}$$

From the last equation, it is obvious that the laser beam spreads out by diffraction and the wavefront area of the optical mode is doubled at a distance equal to the Rayleigh length. For $Z_o=L$, Equation (2.51) gives the characteristic mode radius $\sqrt{L\,l/p}$, which is used for normalizing the *x* and *y* coordinates.

The mode waist is usually located close to the cavity center. According to Equation (2.51) by making Z_o very small (short Rayleigh length), the mode waist becomes small and the beam expands rapidly due to diffraction as it moves to the mirrors. However, the small optical beam waist may reduce the overlap between the optical wave and the narrow electron beam, which leads to gain reduction. If Z_o is too large, however, the mode waist becomes large and the beam does not expand as much as before while moving to the mirrors. In this case, a large mode waist leads to gain reduction as it reduces the overlap between the optical wave and the narrow electron beam in the center of the undulator. Thus, the value of the Rayleigh length is critical for gain optimization. In order to minimize the optical mode volume around a smaller electron beam, the Rayleigh length should be $Z_o \approx L/\sqrt{12}$ [Ref. 5]. This is the typical FEL case.

2. Gaussian Beams

An optical wave with a Gaussian transverse shape everywhere, and also a solution of Equation (2.50), is given by [Ref. 7]

$$a(r,t) = \frac{a_o}{w(t)} e^{-r^2/w^2(t)z_o} e^{if(t)}, \tag{2.53}$$

where a_o is the amplitude of the field at the beam waist which is located at $t = t_w$, f is the optical phase that is given by

$$f(r,t) = -\tan^{-1}\left(\frac{t - t_w}{z_o}\right) + \frac{r^2(t - t_w)}{z_o^2 + (t - t_w)^2}, \tag{2.54}$$

and

$$w^2(t) = 1 + \frac{(t - t_w)^2}{z_o^2}, \tag{2.55}$$

where $z_o = Z_o/L$ is the normalized Rayleigh length, and $r^2 = x^2 + y^2$ is the transverse position related to the normalized *x, y* coordinates. The beam spreads out by diffraction as it moves away from the position of beam waist t_w. From the last equation, it is obvious that the area of the beam doubles when $t = t_w + z_o$.

This Chapter presented an overview of the physics behind the FEL. The equation referred to as the resonance condition was first obtained. This equation expresses the optical wavelength of the FEL as a function of the undulator period and the energy of the relativistic electron beam. The dimensionless pendulum equation, which describes the electron phase space evolution and provides information about the electrons' energy exchange with the optical wave, was also obtained. Additionally, the optical wave equation was derived. The optical wave equation explains the light wave propagation.

Based on the physics behind the FEL, the propagation consequences of short pulses from free electron lasers will be discussed in the Chapter that follows. Specifically, the propagation issue of thermal blooming related to the power spread in the frequency domain that is caused by the pulse format of the FEL will be discussed.

THIS PAGE INTENTIONALLY LEFT BLANK

III. PROPAGATION CONSEQUENCES OF SHORT PULSES FROM FREE ELECTRON LASERS

A high-energy laser weapon system operating in a maritime environment faces several challenges due to atmospheric effects. The propagation of a light wave through the atmosphere just above sea level requires a proper selection of wavelength, power level, pulse format, and beam control so that a lethal amount of energy can be delivered to the target.

The primary propagation issues that need to be considered are the absorption and scattering. At lower power levels, these effects are linear which means that an increase in power at the origin results in an increase in power delivered at the target. However, for high power levels, absorption leads to non-linear effects, such as thermal blooming, where an increase in power from the laser results in a decreasing intensity at the target. Thermal blooming is a result of the atmospheric heating due to absorption, which creates a negative lens in the atmosphere and spreads the beam's core. There is an upper limit on power that can be delivered by a laser without reducing the amount of energy on the target. This is known as the critical power, P_{crit}. The value of P_{crit} depends on the laser-operating wavelength.

The atmospheric transmittance over a wavelength range is a complex problem and crucial to directed energy because it determines the choice of a proper wavelength. Figure 9 demonstrates the dependence of the absorption coefficient on the wavelength. On the horizontal and the vertical axis of that figure are illustrated, in logarithmic scale, the wavelength and the absorption coefficient respectively. The wavelengths from different kinds of lasers are indicated by red lines. The primary windows with low absorption are located at 2.2, 1.6, 1.3 microns (μm), and the lowest one is close to 1.0 μm (1.029-1.064 μm). Thus, the thermal blooming induced by absorption is minimal at this wavelength. However, the scattering increases with decreasing wavelengths since it is dependent on the refractive index and the mean particle size in the atmosphere. The result is that the total loss due to absorption and scattering is about equal across the four windows. However, simulations using the MOLLY code have shown that P_{crit} has a value of about

10 MW at 1.0 μm for distances of up to a few kilometers while at 1.6 μm is in the neighborhood of 3 MW [Ref. 1]. Therefore, if the decision is based on operating the laser at megawatts level of power in the maritime environment, the 1.0 μm wavelength should be chosen. Of course, the 1.6 μm wavelength may be preferable since it falls in the region of the spectrum considered "eye-safe".

In reality, the atmospheric conditions of a maritime environment are a function of a particular area at a particular time of day. Thus, more than one wavelength may be proper to overcome the propagation issues due to the variety of the atmospheric conditions. This requirement implies that the free electron laser is the most logical candidate for maritime high-energy weapons. FELs have the ability to select a wavelength of operation in some bandwidth range, which is a significant advantage compared to the chemical or solid state lasers operating in the maritime environment. Equation (2.10) indicates that the wavelength of the FEL optical beam l is controlled by the undulator period l_o, the undulator parameter K, and the Lorentz factor of the relativistic electron beam g,

$$l = \frac{l_o\left(1+K^2\right)}{2g^2} .$$

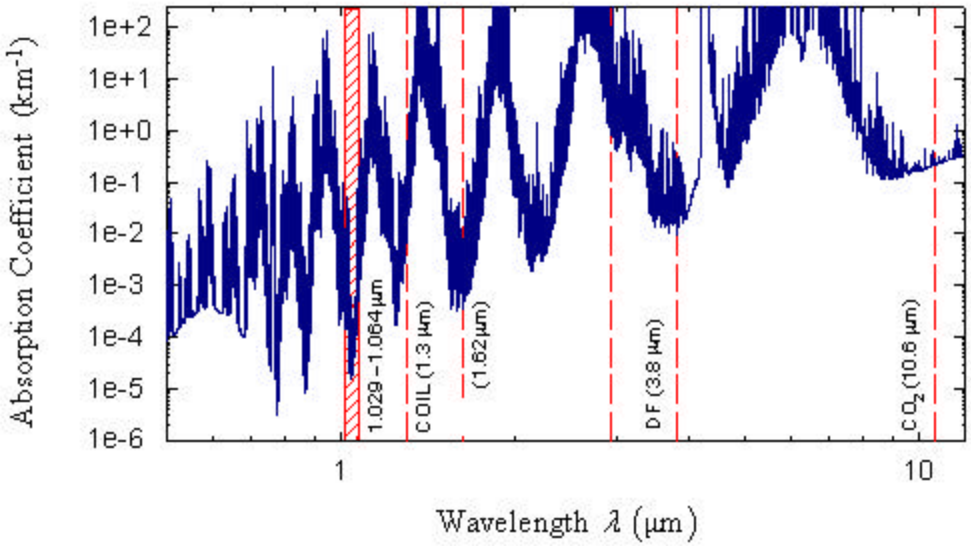

Figure 9. Absorption Coefficient Profile for Maritime Environment. (From [Ref. 4].

A. WHY A MW POWER LEVEL OUTPUT IS REQUIRED

The kill mechanism of a laser is based on delivering a sufficient amount of energy to a relatively small spot on the target. The incident intensity of light should be enough to melt through a missile body during the engagement time so that the missile will finally break up due to aerodynamic stress. Experiments have shown that a flux density of 10 kW/cm^2 is sufficient to melt typical missile materials in a dwell time of a couple of seconds [Ref. 8].

To estimate the required laser output power, examine a typical missile engagement scenario. In order to destroy an incoming missile, the laser flux density on the missile surface should be $F = 10\ \mathrm{kW/cm^2}$ over a radius spot $w = 5\ \mathrm{cm}$, with an engagement dwell time of 3 seconds. Therefore, the average power delivered on the missile's surface is

$$P_R = F p w^2 = \left(10\mathrm{kW/cm^2}\right) p\, 25\mathrm{cm^2} \approx 800\mathrm{kW}\ . \tag{3.1}$$

The major limitations of transfer of laser energy from the source to the target are the absorption and the scattering of the light traveling through the atmosphere. The following exponential law describes the power removed from the beam

$$P_R = P e^{-a_e R}, \tag{3.2}$$

where a_e is the extinction coefficient due to aerosols at sea level, P is the average power of the light beam that leaves the ship, and P_R is the average power of the light beam after traveling distance R through the atmosphere. By supposing a typical value for $a_e \approx 0.05\mathrm{km^{-1}}$ and the missile is located at distance R = 6 km, then the average laser power that must leave the ship, according to the Equation (3.2), is

$$P = P_R e^{a_e R} = \left(800\mathrm{kW}\right) e^{\left(0.05\mathrm{km^{-1}} 6\,\mathrm{km}\right)} \approx 1\mathrm{MW}\ . \tag{3.3}$$

Equation (3.3) indicates that the required power at the ship is well within the capability of an FEL with an average power of 1 MW.

B. POWER SPECTRAL DENSITY (PSD) OF A SHORT PULSE FEL

Free electron lasers, as seen earlier, produce their energy by passing a relativistic electron beam through a structured magnetic field. Electrons accelerated during passage through a magnetic field create the optical radiation. The proposed FEL weapon design uses micropulses of relativistic electrons. The electron micropulses have been accelerated by an accelerator with RF frequency Ω. Thus, the FEL operates in a pulsed mode, producing an output light beam with pulse repetition frequency Ω.

The FEL used for this study has an average power $P = 1$ MW, optical wavelength $l = 1.0\,\mu$m, pulse repetition frequency $\Omega = 750$MHz, and pulse duration of 1 ps. A representation of the light pulses with a rectangular pulse shape in the time domain is shown in Figure 10, where $2T_1$ is the pulse duration, $T = \Omega^{-1}$ is the pulse period, and $\hat{a}$ is the peak amplitude of the light electric field in a micropulse.

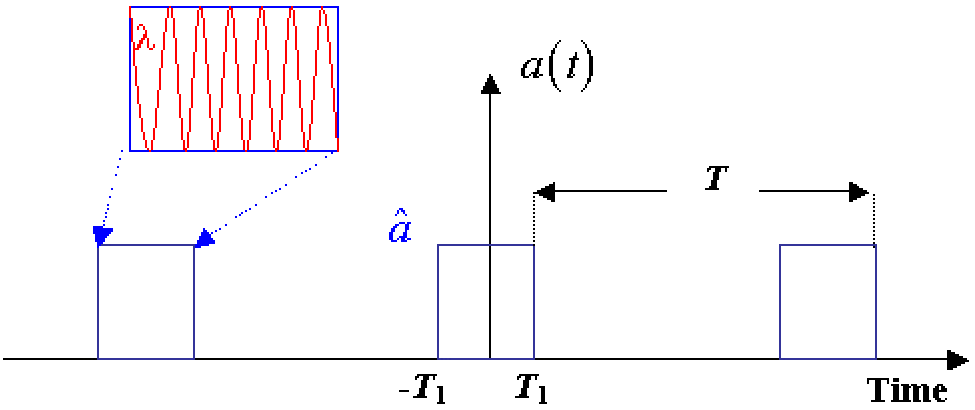

Figure 10. Short Pulse Free Electron Laser.

As seen in the previous section, the dwell time of a single engagement is 3 sec. Thus, for a single engagement, the beam consists approximately of 2 billion pulses. This is a very large number, and in order to simplify our analysis, a single engagement is considered to contain an infinite number of pulses. Using this approximation, the following equation describes the light signal in the time domain,

$$a(t) = \sum_{n=-\infty}^{n=\infty} \hat{a}\cos(2p\, f_o t + q_n)\prod(t - nT), \tag{3.4}$$

where f_o is the light frequency that satisfies $c = l\, f_o$, c is the speed of light, q_n is the random phase of each optical micropulse, and $\Pi(t)$ is the function describing a rectangular pulse shape,

$$\prod(t) = \begin{cases} 0, & |t| > T_1 \\ 1, & |t| \le T_1 \end{cases} . \tag{3.5}$$

In reality, each pulse would have a smooth bell shape and not the idealized rectangular shape described in Equation (3.4). In order to be more accurate in our analysis, the following cosine function $c(t)$ is used to approximate the shape of each pulse,

$$c(t) = \begin{cases} 1, & |t| < T_1(1-r) \\ 1/2\left[1+\cos\left(p\,\dfrac{r-1+\dfrac{|t|}{T_1}}{2r}\right)\right], & T_1(1-r) \le |t| \le T_1(1+r) \\ 0, & |t| > T_1(1+r), \end{cases} \tag{3.6}$$

where r is a roll-off factor which ranges between 0 and 1. When r equals zero, the function $c(t)$ represents a rectangular pulse shape. Normalized pulse shapes for $r = 0$, $r = 0.5$, and $r = 1$ are shown in Figure 11.

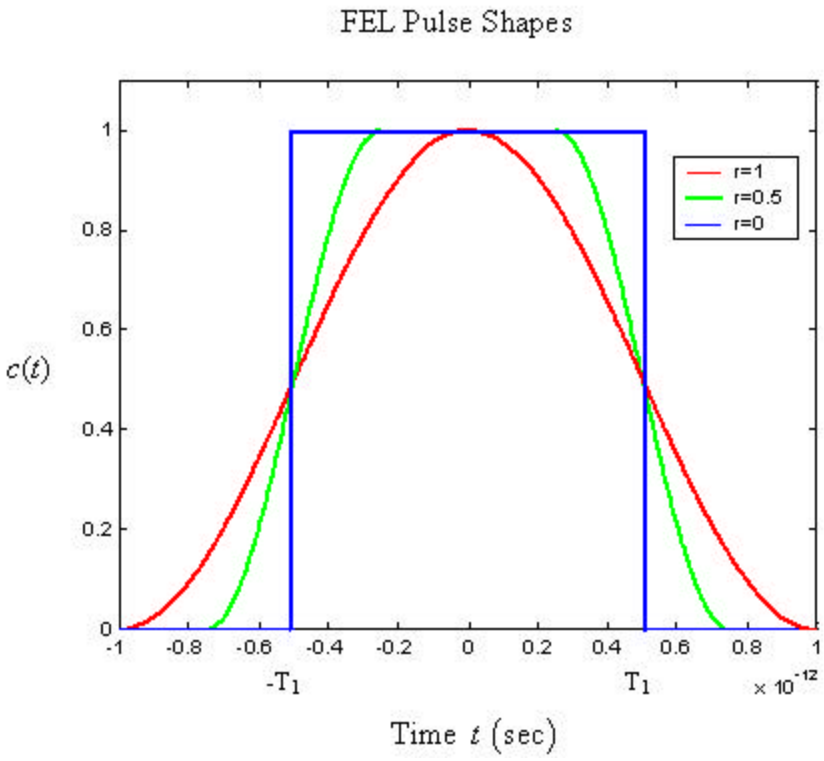

Figure 11. Plot of Equation (3.6) for $r=0$, $r=0.5$, $r=1$, and T_1=0.5 ps.

The Fourier transform of Equation (3.6) is given by [Ref. 9]

$$C(f)=\frac{\sin(2p\,fT_1)}{p\,f}\frac{\cos(2p\,rfT_1)}{1-(4rfT_1)^2}=2T_1\mathrm{sinc}(2p\,fT_1)\frac{\cos(2p\,rfT_1)}{1-(4rfT_1)^2}. \quad (3.7)$$

Replacing the function $\Pi(t)$ with $c(t)$, Equation (3.6) becomes,

$$a(t)=\sum_{n=-\infty}^{n=\infty}\hat{a}\cos(2p\,f_o t+q_n)c(t-nT), \quad (3.8)$$

which is truncated in order to be able to evaluate the power spectral density (PSD) for $a(t)$ [Ref. 10]

$$a_{T'}(t)=\begin{cases}\sum_{n=-N}^{n=N} a\cos(2p\,f_o t+q_n)C(t-nT), & |t|<\frac{1}{2}T'\\ 0, & \text{otherwise,}\end{cases} \quad (3.9)$$

where the subscript T' denotes the truncated version of $a(t)$, equals to $T'=2(N+1/2)T$, and N is an integer.

The average power *P* of the FEL pulse train is given by [Ref. 10]

$$P = \frac{1}{T}\int_{-T/2}^{T/2} a^2(t)\,dt = \int_{-\infty}^{\infty}\left[\lim_{T'\to\infty}\frac{1}{T'}\overline{\left|A_{T'}(f)\right|^2}\right]df = 1\text{MW}, \tag{3.10}$$

where the bar represents the frequency average, $a(t)$ is given by Equation (3.8), T has the value defined earlier, and $A_{T'}(f)$ is the Fourier transform of $a_{T'}(t)$. By combining Equations (3.8), (3.10), and solving the latter, the amplitude $\hat{a}$ of each pulse is obtained,

$$\hat{a} = \sqrt{\frac{PT}{T_1}\frac{1}{1-r/4}}\ . \tag{3.11}$$

In order to evaluate the PSD of the FEL short pulse train, the Fourier transform of Equation (3.9), $A_{T'}(f)$, is first obtained

$$A_{T'}(f) = \mathrm{F}\left[a_{T'}(t)\right] = \frac{\hat{a}}{2}\sum_{n=-N}^{n=N}\left[e^{iq_n}d(f-f_o) + e^{-iq_n}d(f+f_o)\right] * C(f)e^{-i2p\,fnT},$$

or,

$$A_{T'}(f) = \frac{\hat{a}}{2}\sum_{n=-N}^{n=N}\left\{e^{-i\left[2pn(f-f_0)T-q_n\right]}C(f-f_o) + e^{-i\left[2pn(f+f_0)T+q_n\right]}C(f+f_o)\right\}, \tag{3.12}$$

where the notation $x * y$ represents the convolution between *x* and *y*, $C(f)$ is the Fourier transform of Equation (3.6) and is given by Equation (3.7). Then the PSD of $a(t)$ becomes [Ref. 10]

$$P_a(f) = \lim_{T'\to\infty}\left(\frac{\overline{\left|A_{T'}(f)\right|^2}}{T'}\right). \tag{3.13}$$

The substitution of Equation (3.12) into Equation (3.13) yields the final form of the single-sided PSD of $a(t)$

$$P_a(f) = \frac{\hat{a}^2}{2T}\left[C(f-f_o)\right]^2,$$

and by using Equation (3.7),

$$P_a(f) = \frac{2\hat{a}^2 T_1^2}{T}\left\{\text{sinc}\left[2p\,(f - f_o)T_1\right]\frac{\cos\left[2p\,r(f - f_o)T_1\right]}{1-\left[4r(f - f_o)T_1\right]^2}\right\}^2, \qquad (3.14)$$

where the amplitude $\hat{a}$ is given by Equation (3.11). Now it is possible to calculate the average power of the FEL short pulse train $a(t)$ in a finite frequency band $[f_1, f_2]$ of the spectrum as,

$$P_{f_1 \to f_2} = \int_{f_1}^{f_2} P_a(f)\,df\ . \qquad (3.15)$$

Figure 12 represents the distribution of power in the pulse train as a function of frequency according to Equation (3.14), for a frequency range from f = 2.97×10^{14} Hz to f = 3.03×10^{14} Hz. The spectrum is plotted for three values of the roll-off factor: $r = 0$ (rectangular pulse shape), $r = 0.5$, and $r = 1$ (cosine bell shaped pulse).

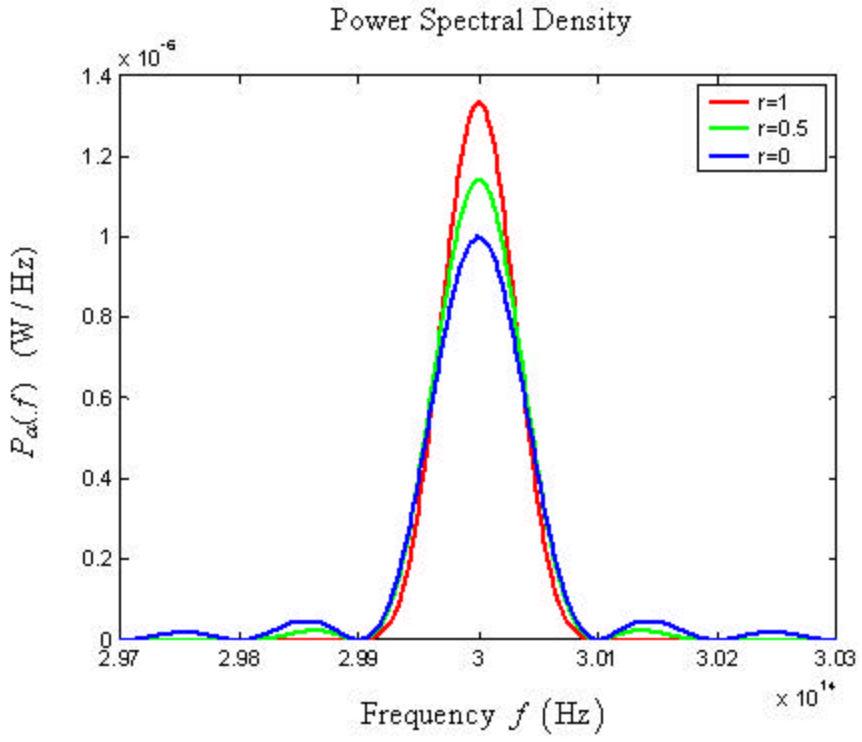

Figure 12. Power Spectral Density for an FEL Operating in Pulse Mode.

From Figure 12, it is obvious that the PSD for both the rectangular and the bell-shape pulses is centered at the fundamental frequency $f_o = 3\times10^{14}\,\text{Hz}$ or $l = 1\mu\text{m}$. However, it can be seen that the rectangular pulse shape (r =0) spreads the power in the spectrum much more than the latter ones. The calculated average power that is contained in the fundamental lobe, which corresponds to the spectrum [2.99×10^{14} Hz, 3.01×10^{14} Hz], is 90% of the total average power for the rectangular case, while for the bell shaped cases, it is more than 99.9%. Thus, the cosine bell-shaped pulse decreases the sidelobes of the power distribution in the frequency domain and concentrates most of the power in the main lobe close to the fundamental frequency, which is desirable for laser beam propagation through narrow transmission windows in the atmosphere.

In conclusion, the FEL operation in pulse mode leads to power spread in the frequency domain, depending on the FEL pulse shape in the time domain. The propagation through the atmosphere of a broad-spectrum laser pulse may have several consequences:

- Presence of power in frequency components where the absorption coefficient is high. This will increase the total absorbed power and also may cause nonlinear effects such as thermal blooming.
- Presence of a sufficient amount of power in the visible region, where the scattering process may make the laser beam visible. In most cases, in a real operational environment, this will be undesirable for a weapon system.
- Presence of a sufficient amount of power in the region of the spectrum that is not considered eye safe. This will compromise the personnel safety on the ship, especially those who will have eye contact with the beam director during the engagement.
- Finally, the presence of a sufficient amount of power in the microwave regime that may lead to a soft kill mechanism of an incoming missile threat by damaging the electronics the missile.

In the present study, the possible problem of thermal blooming for the proposed FEL weapon design will be examined.

C. THERMAL BLOOMING

The issue of whether the propagation of a MW-level FEL laser beam through the atmosphere causes thermal blooming will be studied next. An FEL operating in pulse mode, as previously seen, leads to power spread in the frequency domain. The worst-case scenario is that from a square optical pulse shape. Figure 13 shows the normalized power spectral density of such a pulse train for the spectrum [10^{12} Hz, $3x10^{15}$ Hz].

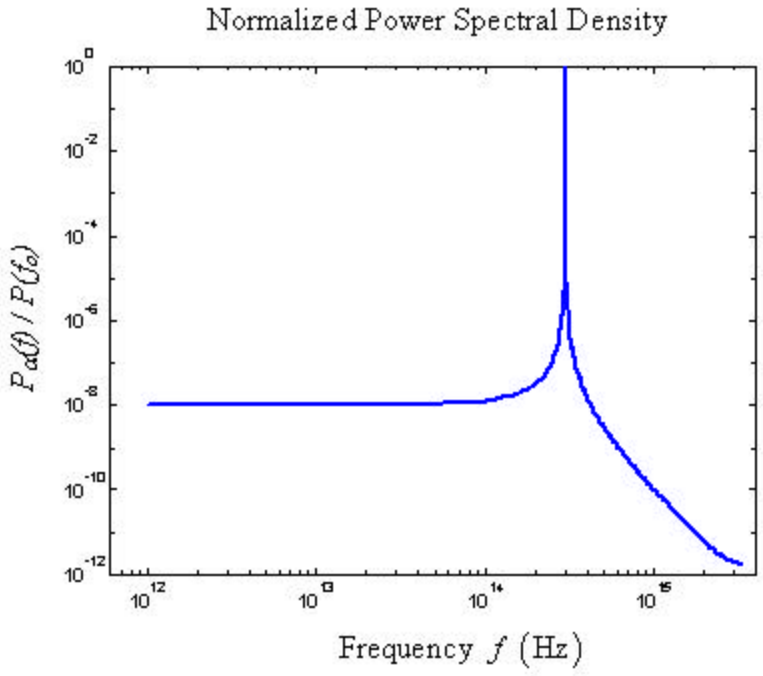

Figure 13. Normalized power spectral density of a square optical pulse shape.

The absorption coefficient profile versus frequency for a moderately clear maritime atmosphere with visibility of 23 km is shown in Figure 14.

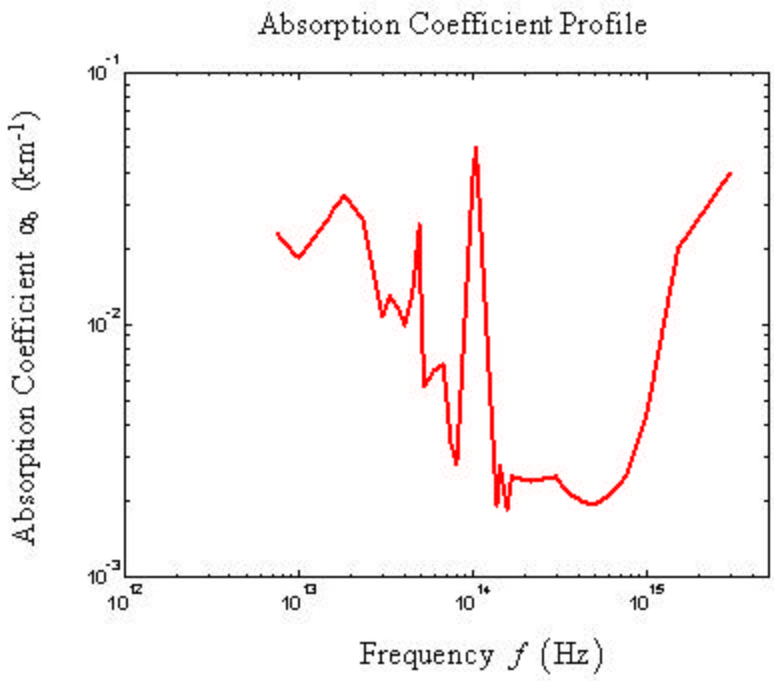

Figure 14. Atmospheric Absorption Coefficient Profile Versus Frequency for Moderately Clear Atmosphere (23 km Visibility).(After [Ref. 7]).

The power that is contained in the spectrum of Figure 13 equals to 999.85 kW. The propagation of that amount of power through the atmosphere will lead to a specific amount of absorbed power. Consider one liter of air that has about the same cross section as the laser beam. Then, based on Equation (3.2) for R=10 cm and the absorption coefficient profile of Figure 13, the absorbed power by 1 liter of air is calculated to be 0.255 W, or an absorbed energy rate $\Delta E/\Delta t = 0.255$ Joule/sec. For a CW FEL (no pulse) operating at the same frequency and at the same atmospheric conditions, the absorbed power would be 0.25 W. From these results, it can be seen that the absorbed power increases only by a small amount (0.005 W) due to spectral spread of the short optical pulse.

The specific heat of air C_v is given by

$$C_v = \frac{\Delta \mathrm{E}}{V \Delta T} \approx 1 \frac{\mathrm{J}}{l\ ^0\mathrm{C}}, \tag{3.16}$$

where V is the air volume and ΔT is the temperature rise of that volume. By considering a dwell time of 1 sec and solving the last equation for ΔT the rate of temperature rise of the air volume equals to is

$$\frac{\Delta T}{\Delta t} = \frac{\Delta \mathrm{E}/\Delta t}{VC_v} = \frac{0.25\ \mathrm{J}/\mathrm{s}}{1l\left(1\frac{\mathrm{J}}{l\ {}^0\mathrm{C}}\right)} = 0.25\frac{{}^0\mathrm{C}}{\mathrm{s}}. \tag{3.17}$$

Taking into account the ship's movement, the incoming missile's velocity, and the local wind direction, a stagnate air column (stagnation zone) can exist somewhere along the laser beam path. Statistically, for a dwell time of 1 sec, the size of a stagnation zone may vary from $\Delta z = 1$ m to 100 m [Ref. 7].

Any small change in the temperature of the stagnate air column causes a small change in the index of refraction of the air. The index of refraction n is given by

$$n = \frac{c}{v_c}, \tag{3.18}$$

where c is the speed of light in vacuum and v_c is the speed of light in air. Then, the small change in the index of refraction will be

$$\Delta n = -\frac{c}{v_c}\frac{\Delta v_c}{v_c} \approx -\frac{\Delta v_c}{c}, \tag{3.19}$$

since $v_c \approx c$. By relating Δn to the temperature change ΔT, [Ref. 7]

$$\Delta n = -10^{-6}\Delta T\left({}^0\mathrm{C}\right). \tag{3.20}$$

From the last two equations, the change in the speed of light is

$$\Delta v_c = -c\,\Delta n = -10^{-6}c\Delta T\left({}^0\mathrm{C}\right). \tag{3.21}$$

This leads to a lens effect. The inner core of the stagnation zone will be hot and the light travels at speed $v_c + \Delta v_c$, while the outer part of the zone is less warm and the light travels at speed v. That difference in light speed leads to a difference in path length, where the light at the inner part of the beam gets ahead of the light at the edge of the beam by

$$\Delta s = \Delta v_c \frac{\Delta z}{c} = -\Delta n \Delta z = 10^{-6} \Delta T \left({}^0\mathrm{C} \right) \Delta z \,, \tag{3.22}$$

after traveling through a stagnation zone of length Δz. The racing of the light traveling through a stagnation zone is shown in Figure 15.

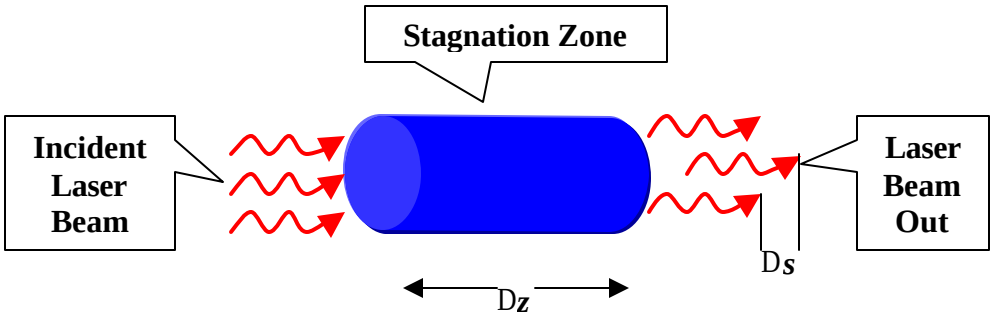

Figure 15. Light Traveling through a Stagnation Zone.

The effect of the stagnation zone is equivalent to a negative lens. Thus, thermal blooming is a result of the atmospheric heating due to absorption, which creates a negative lens in the atmosphere and spreads the beam, as shown in Figure 16.

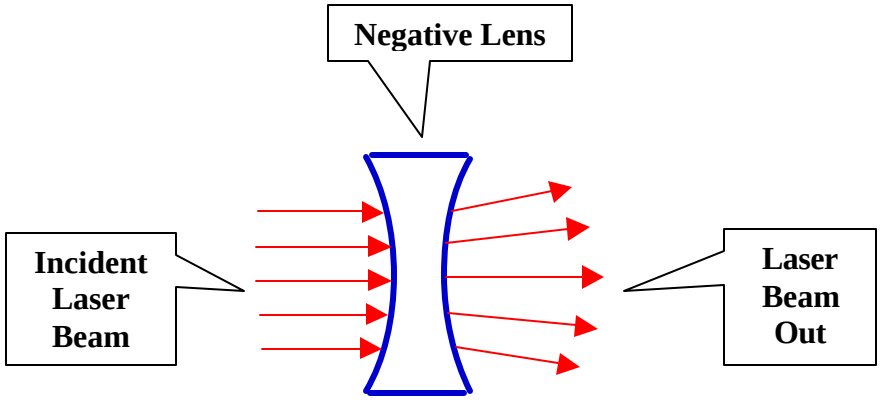

Figure 16. Laser Beam Passing through a Negative Lens.(After [Ref. 4]).

The lens effect is measured by comparing the path difference Δs to the optical wavelength l. Then, from Equation (3.22)

$$\frac{\Delta s}{l} = 10^{-6}\,\Delta T\left({}^{0}\mathrm{C}\right)\frac{\Delta z}{l}. \tag{3.23}$$

Considering a dwell time of 1sec, $l = 1\mu\mathrm{m}$, $\Delta z = 10\,\mathrm{m}$, then $\Delta T = 0.25^{0}\,\mathrm{C}$ and Equation (3.23) becomes

$$\frac{\Delta s}{l} = 10^{-6}\left(0.25\right)\frac{10\mathrm{m}}{1\mu\mathrm{m}} = 2.5. \tag{3.24}$$

If a stagnation zone of length $\Delta z = 50\,\mathrm{m}$ is considered, then $\Delta s/l = 12.5$ wavelengths. Thus, it can be concluded that the blooming effect of a MW level FEL at $l = 1\mu\mathrm{m}$ is not strong for a stagnation zone size less than 10 m, but it gets quite strong for greater values of Δz. Of course, at this point, it is necessary to mention also that our approach is only based on the atmospheric absorption profile for a moderately clear atmosphere. The results may vary for different atmospheric conditions.

Another significant parameter is the position of the stagnation zone along the beam path. Since the stagnation zone tends to spread the laser beam core, even a strong blooming effect close to the target may be preferable to a small stagnation zone that is positioned close to the beam director.

Also, there are more detailed transmission windows in the atmosphere that are not included in Figure 14. The result for a window with higher transmission would decrease absorption and blooming.

D. THE EFFECT OF THERMAL BLOOMING ON THE LASER BEAM

Beginning from Maxwell's wave equation, the dimensionless parabolic wave equation in free space (Equation 2.50) can be obtained which describes the diffraction of the laser beam from the beam director to the target. One solution of Equation (2.51) is a Gaussian laser beam described by Equations (2.53) and (2.54).

As seen previously, the atmospheric absorption in a stagnation zone causes thermal blooming. Considering that the beam during the propagation to the target hits a stagnation zone at a position defined by the dimensionless time t_c, then the phase distortion caused at the beam by the thermal blooming is described by [Ref. 7]

$$a_{out}\left(x,y,t_c\right) = e^{-i\left|a(x,y,t_c)\right|^2 df_s}\,a_{in}\left(x,y,t_c\right), \tag{3.25}$$

where a_{in} is the field entering the zone, a_{out} is the field after the zone, and df_s is the strength of the zone lens. The phase change factor of the last equation can be related to the lens effect measured by the path difference Δs over the optical wavelength l ,

$$\left|a(x,y,t_c)\right|^2 df_s = \frac{\Delta s}{l}. \tag{3.26}$$

Using a simulation code, it was possible to solve Equation (2.50) numerically for the Gaussian laser beam described by Equations (2.53) and (2.54). The program follows the evolution of the laser field over many small time steps dt in a transverse window consisting of *nx* bin elements in both the *x* and *y* directions. The simulation shows the effect of the diffraction on a laser beam that is focused on the target with or without thermal blooming.

The results of the simulation are plotted in Figures 17 and 18. The color intensity of each plot represents the field intensity strength at each bin as shown at the bottom of each plot. Each figure contains two plots. The plot on the left is a side view of a slice through the laser beam as the field $a(x, nx/2, t)$ evolves in dimensionless time from $t = 0$ to 1. The plot on the right side represents the spot of the laser beam at the target, $\left|a(x, y, t = 1)\right|$.

Both plots in Figure 17 indicate a focusing beam due to the diffraction in the absence of thermal blooming, while Figure 18 shows a distortion produced at the laser beam by the stagnation zone of strength $df_s = 10$ at the position $t_c = 0.7$. Since the dimensionless optical field amplitude was chosen to be unity, the stagnation zone has a length of about 50 m. The stagnation zone creates a “hole” in the laser beam, which is obvious in both the side and the front view plots.

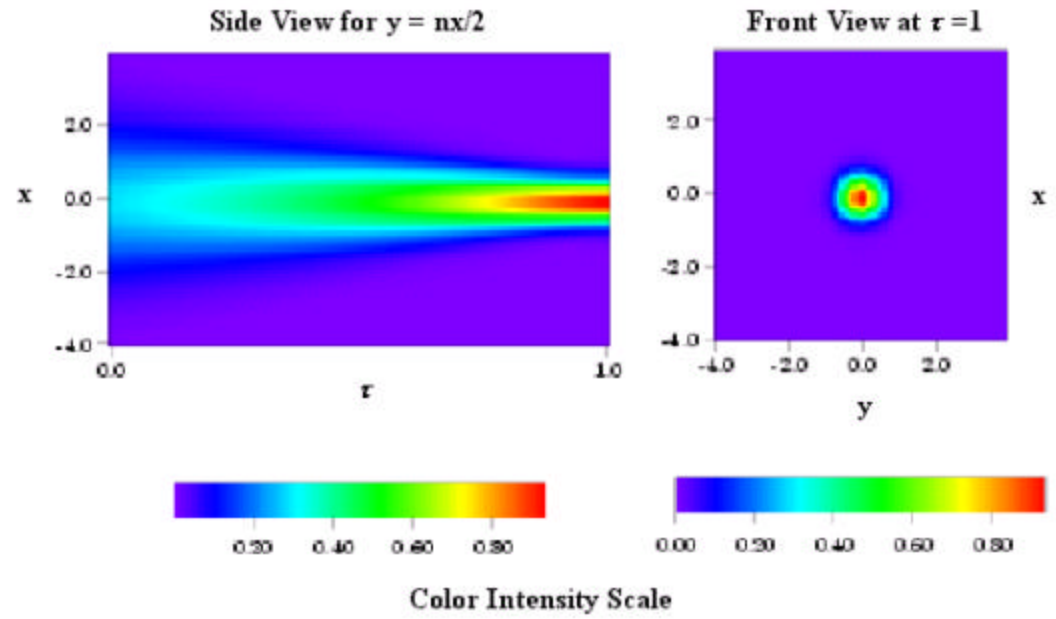

Figure 17. Laser Beam Focused on the Target Due to Diffraction.

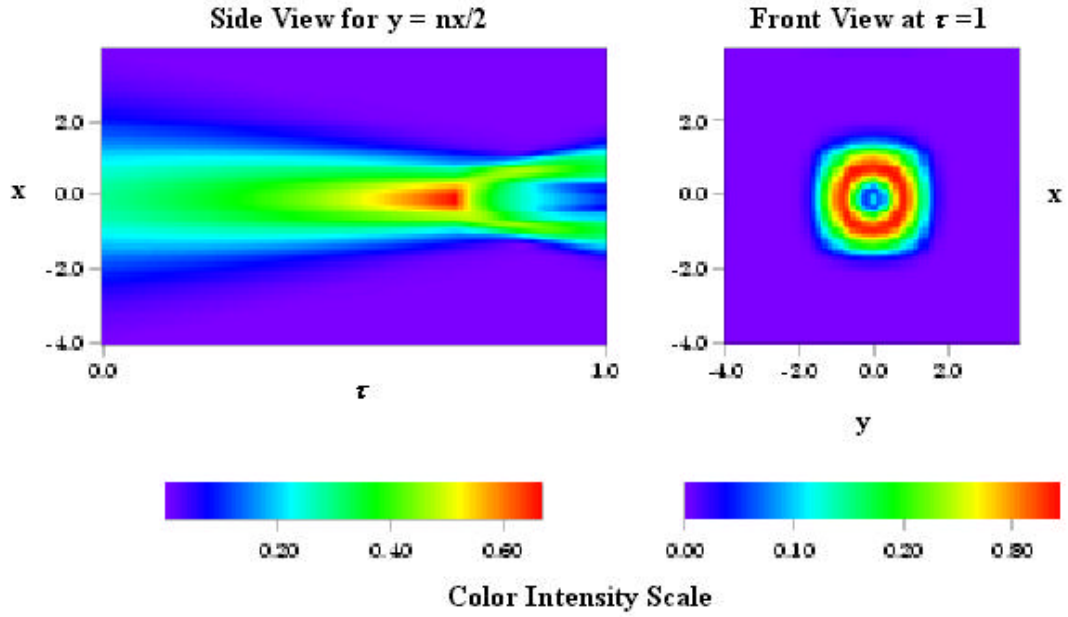

Figure 18. Laser Beam Focused on the Target Due to Diffraction While Hitting a Stagnation Zone at $t_c = 0.7$.

E. CONCLUSIONS

In this Chapter, the spectrum of the laser beam output from the proposed FEL weapon design is obtained. The proposed FEL operates in a pulse mode, producing optical micropulses 1 ps long at a pulse repetition frequency of $\Omega = 750$ MHz. The spectrum may cover many absorption lines. The absorbed laser energy heats the air and may lead to non-linear effects such as thermal blooming. It is found that thermal blooming is not an issue for a moderate clear atmosphere when the stagnation zone size remains less than 10 m.

The next Chapter presents the simulation results of the proposed FEL weapon system. The effects of the electron beam focusing and electron beam off-axis shifting are studied.

THIS PAGE INTENTIONALLY LEFT BLANK

IV. SIMULATIONS OF THE 1 MW WEAPON DESIGN FEL WITH STRONGLY FOCUSED ELECTRON AND OPTICAL BEAMS

A. SHIPBOARD FEL COMBAT SYSTEM

A Naval FEL application is defense from anti-ship missiles at ranges around 5 km. As seen previously, the destruction of a missile at that range requires a laser beam of about 1 MW power at around 1 μm wavelength for an engagement that lasts a few seconds.

The naval application also requires a compact configuration with the laser components packaged into a rectangular module placed onboard a ship. The proposed FEL MW design has an estimated size of 12 m x 4 m x 2 m and is shown in Figure 19. The figure represents a top and a side view of the module. The accelerator runs along one side of the box while the optical resonator lies on the opposite side, leaving the support components in the area between these two. The whole system is estimated to weigh about 40 tons with an estimated cost of about $60 M [Ref. 11]. A possible arrangement of the shipboard FEL system, as presented during the 2001 FEL workshop in Newport News VA, is shown in Figure 20 [Ref. 1]. The modular support systems, such as the RF klystrons (red boxes), are located separately but near the other components. This layout shows the system in a horizontal orientation near the keel penetrating a single water-tight bulkhead, which is an undesirable but tolerable feature.

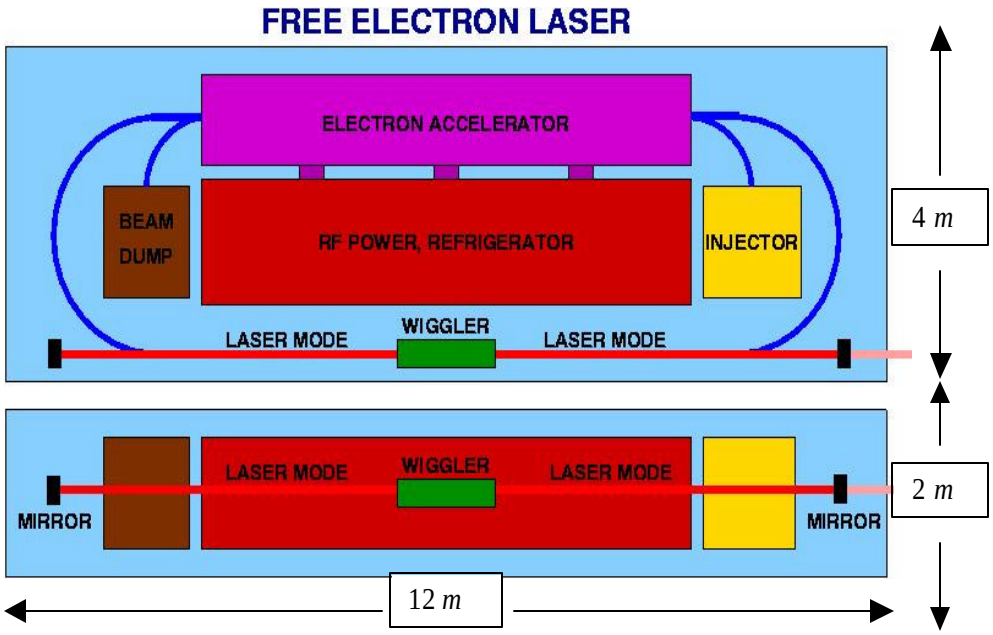

Figure 19. Proposed FEL MW Design. (From [Ref. 11]).

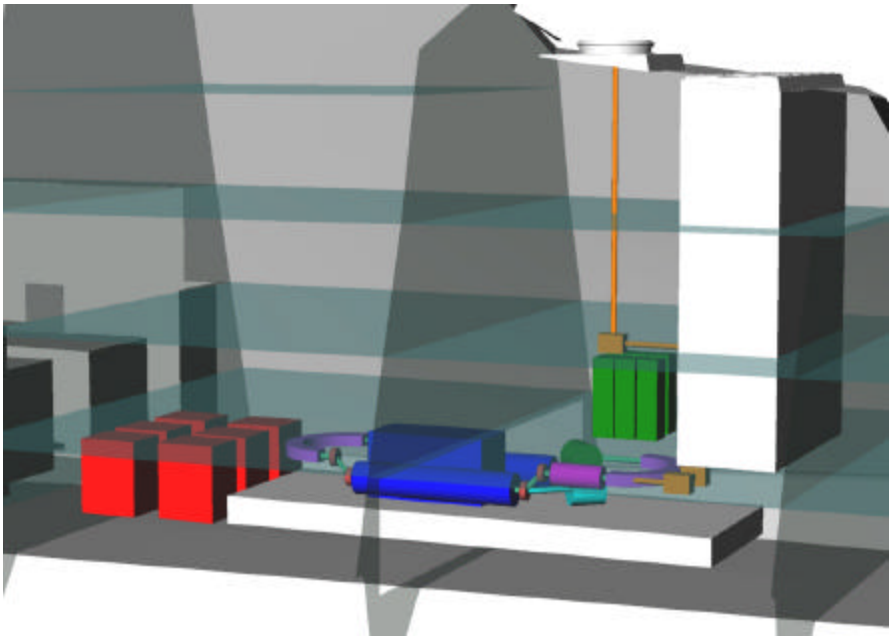

Figure 20. Conceptual FEL Weapon System Ship Arrangement (red boxes: RF klystrons, RF power components - blue boxes: refrigerator, accelerator, wiggler – purple boxes: bending magnets). (From [Ref. 1]).

The requirement of high output power from a small compact FEL onboard a ship raises some challenging issues, such as the optical intensity on the mirrors and vibrationally induced misalignments of the electron beam and the cavity mirrors [Ref. 1].

1. Short Rayleigh Length

The large intracavity power and a small optical beam size lead to high intensity on the cavity mirrors, making them vulnerable to damage. This problem could be solved by inventing more robust mirrors, by lengthening the cavity in order to increase the mode area at the mirrors by diffraction, or by using a shorter Rayleigh length [Ref. 12]. In the current design, however, the resonator length is limited to S = 12 m. Additionally, it is estimated that cooled sapphire mirrors with a transmissive coating can handle an intensity of $\approx$200-300 kW/cm^2 [Ref. 11]. Thus, the use of a short Rayleigh length resonator is required to increase the spot size on the mirrors, leaving a very small optical mode waist for the intense FEL interaction.

The requirement of a short Rayleigh length resonator for a high power FEL can be derived as follows. A typical FEL has an undulator length of $L = 3$ m and a Rayleigh length of $Z_o \approx L/3 = 1$ m. For $l = 1$ μm, the optical mode waist according to Equation (2.51), $Z_o l = pW_o^2$, would be about 0.6 mm. Then, from Equation (2.52) for $z = S/2 = 6$ m, the laser spot size at the mirrors would still be a few mm $(W \approx 3.6$ mm$)$. Assuming 25% output coupling, 1 MW output power requires a power stored inside the cavity of 4 MW. The intensity on the mirrors would then be about 10 MW/cm^2, which, of course, will lead to mirror damage. By reducing the Rayleigh length to $Z_o = 1.8$ cm, the spot size of the beam at the mirrors is 2.5 cm, and the intensity is reduced to 210 kW/cm^2. This is within the tolerance of the mirrors. However, for $Z_o = 1.8$ cm, the optical mode waist is very narrow in the center of the cavity, $W_o = 0.08$ mm.

A short Rayleigh length implies a very small optical mode waist and a beam which expands rapidly towards the end of the undulator. In the case where the electron beam radius is greater than the mode waist radius, $r_e > W_o$, many electrons will not overlap with the intense optical field in the interaction region near the cavity center. Thus, a narrow electron beam is desirable. Additionally, the undulator length must be short in order to avoid damaging the undulator magnets by the intense rapidly-expanding laser beam.

2. High Power FEL Parameters

The goal is to design an FEL with 1 MW output power, using a short Rayleigh length optical cavity. Therefore, the optical resonator could have the characteristics shown in the table below.

OPTICAL RESONATOR PARAMETERS	
Resonator Length	$S = 12$ m
Optical Wavelength	$l = 1$ μm
Mode Waist	$W_o = 0.08$ mm
Quality Factor	$Q_n = 3$ (28% power transmission per pass)
Rayleigh Length	$Z_o = 1.8$ cm
Intensity on Mirrors	$210\ \text{kW}/\text{cm}^2$

Optical Resonator Parameters for a MW Level FEL.(From [Ref. 13]).

As previously seen, the short Rayleigh length limits the undulator length. In this case, the linearly polarized undulator has a length of only $1/20^{th}$ of the resonator length. In this manner, fewer undulator periods are used, which enhances the extraction efficiency according to Equation (2.33). The magnetic undulator has the characteristics shown below.

MAGNETIC UNDULATOR PARAMETERS	
Undulator Length	$L = 60$ cm
Undulator Period	$l_o = 3$ cm
Number of periods	$N = 20$
Undulator rms Parameter	$K = 2.8$

Magnetic Undulator Parameters for a MW Level FEL. (From [Ref. 13]).

Finally, the MW FEL design calls for an electron beam with the characteristics shown below.

ELECTRON BEAM PARAMETERS	
Electron Beam Energy	$K_e = 185$ MeV
Average Current	$\overline{I} = 0.8$ A
Peak Current	$\hat{I} = 3.2$ kA
Pulse Length	$l_e = 0.1$mm
Electron Beam Radius	$r_e = 0.14$ mm
Pulse Repetition Frequency	$\Omega = 750$ MHz
Bunch Charge	$q = 1.1$nC
Electron Beam Emittance(normalized)	$e_n = 24$mmrad
Extraction Efficiency	$h \geq 0.7\%$

Electron Beam Parameters for a MW level FEL. (From [Ref. 13]).

B. BETATRON MOTION

The FEL weapon design uses a linearly polarized undulator. Thus, it is necessary to calculate the electron motion in this kind of undulator. The undulator magnetic field can be written as

$$\vec{B}_u = B\left[0, \sin\left(k_o z\right)\cosh\left(k_o y\right), \cos\left(k_o z\right)\sinh\left(k_o y\right)\right], \tag{4.1}$$

where $k_o = 2p/l_o$ is once more the undulator wavenumber. The magnetic field near the undulator *z*-axis $(y \approx 0)$ is

$$\vec{B}_u = B\sin\left(k_o z\right)\hat{y}. \tag{4.2}$$

By squaring and averaging over an undulator period to remove the fast electron wiggling motion Equation (4.1) we have

$$\begin{aligned}\overline{\left|\vec{B}_u\right|^2} &= \frac{B^2}{2}\left[\cosh^2\left(k_o y\right)+\sinh^2\left(k_o y\right)\right] \\ &= B^2\left[\frac{1}{2}+\sinh^2\left(k_o y\right)\right] \\ &\approx B^2\left[\frac{1}{2}+\left(k_o y\right)^2+\ldots\right].\end{aligned} \tag{4.3}$$

Thus, the rms value of the magnetic field is given by

$$B_{rms} = \sqrt{\overline{\left|\vec{B}_u\right|^2}} \approx \frac{B}{\sqrt{2}}\left(1+\left(k_o y\right)^2+\ldots\right). \tag{4.4}$$

From the last equation, it is obvious that the field increases off-axis with y, focusing the electrons back towards the undulator axis. Near the undulator axis, $k_o y \approx 0$, the undulator field is approximately $B_{rms} \approx B/\sqrt{2}$.

The total force acting on the electron comes from the Lorentz force Equation (2.13), with the magnetic field given by Equation (4.1). Assuming no light is present $\left(\dot{g}=0, \vec{E}_s=0\right)$,

$$\begin{aligned}\dot{b}_x &= -\frac{eB}{g\,m_e c^2}\left[\dot{y}\cos\left(k_o z\right)\sinh\left(k_o y\right)-\dot{z}\sin\left(k_o z\right)\cosh\left(k_o y\right)\right], \\ \dot{b}_y &= \frac{eB}{g\,m_e c^2}\dot{x}\cos\left(k_o z\right)\sinh\left(k_o y\right), \\ \dot{b}_z &= -\frac{eB}{g\,m_e c^2}\dot{x}\sin\left(k_o z\right)\cosh\left(k_o y\right).\end{aligned} \tag{4.5}$$

The first equation can be solved exactly by integration. Assuming perfect electron injection near the undulator axis in order for the integration constant to be zero, it becomes

$$\begin{aligned}b_x &= -\frac{eB}{k_o g\,m_e c^2}\cos\left(k_o z\right)\cosh\left(k_o y\right) \\ &= -\frac{\sqrt{2}}{g}\frac{eB_{rms}\,l_o}{2p\,m_e c^2}\cos\left(k_o z\right)\cosh\left(k_o y\right) \\ &= -\frac{\sqrt{2}K}{g}\cos\left(k_o z\right)\cosh\left(k_o y\right),\end{aligned} \tag{4.6}$$

where K is the undulator parameter, given by Equation (2.3). Combining the last two equations we have

$$\begin{aligned} \dot{b}_y &= -\frac{cK^2 k_o}{g^2}\cos^2(k_o z)\sinh(2k_o y), \\ \dot{b}_z &= \frac{cK^2 k_o}{g^2}\sin(2k_o z)\cosh^2(k_o y). \end{aligned} \tag{4.7}$$

For an electron near the undulator axis, $(k_o y << 1)$, the electron motion over many undulator periods can be determined. Averaging Equation (4.7) over many l_o, gives $\overline{\dot{b}_z} \approx 0$ or $\overline{b_z} = b_o$, and $\overline{\dot{b}_y} \approx -\left(cK^2 k_o / g^2\right) y$. Therefore, the averaged equation of motion in the y direction is

$$\ddot{y} = -\frac{c^2 K^2 k_o^2}{2g^2}\sinh(2k_o y) \approx -\left(\frac{cKk_o}{g}\right)^2 y. \tag{4.8}$$

Again introducing the dimensionless time $t \equiv ct/L$ and the dimensionless derivatives $\dot{(...)} = d(...)/dt$, the last equation becomes

$$\ddot{y} = -\left(\frac{Kk_o L}{g}\right)^2 y. \tag{4.9}$$

From Equation (4.9), it is obvious that the electron motion in the y direction is that of a simple harmonic oscillator, with a dimensionless betatron frequency

$$w_b = \frac{Kk_o L}{g} = \frac{2pNK}{g}. \tag{4.10}$$

For the parameters of the weapon design $w_b \approx 2p/8$, the electron executes only $1/8$ of a betatron oscillation along the undulator axis. Thus, the electron undergoes a slow oscillation with frequency w_b in the y direction along the undulator axis.

A general solution of Equation (4.9) has the form

$$y(t) = y_o \cos(w_b t) + \frac{Lq_{y_o}}{w_b}\sin(w_b t), \tag{4.11}$$

where y_o is the initial ($t = 0$) offset *y*-coordinate of the electron entering the undulator, $q_{y_o} = \dot{y}(0)/L$ is the initial angle of the electron velocity with respect the undulator axis on the *yz* plane, and $\dot{y}(0)$ is the initial electron *y*-component velocity.

The betatron motion of an electron with initial coordinates y_o and q_{y_o} in the *y* direction was studied. Since the field is independent of the *x* coordinate, the trajectory can be displaced in the *x* direction without any change in $\overline{b_z}$ or the resonance condition. In an experiment, any displacement of the electron trajectory in the *x* direction is confined by the extent of the optical mode, or by using additional focusing magnetic fields. However, an angle q_{x_o} does affect the resonance condition according to Equation (2.31) by changing $\overline{b_z}$ for a given g. Since an electron's phase velocity is given by $v = L\left[\left(k + k_o\right) b_z - k\right]$, it can be shown that an electron injected with a displacement y_o and an angle $q_o = \sqrt{q_{x_o}^2 + q_{y_o}^2}$ reduces the phase velocity by [Ref. 5]

$$\Delta v = -\frac{2p N}{1+K^2}\left(K^2 k_o^2 y_o^2 + g^2 q_o^2\right). \tag{4.12}$$

In reality, the beam consists of a very large number of electrons that enter the undulator with a random distribution of displacements and angles with mean values $\overline{y_o}$ and $\overline{q_o}$. The product of these two mean values defines the beam emittance. In most cases, the contributions of these two values are matched using focusing magnetic fields, so that the beam does not expand too much as it moves along the undulator and the phase velocity spread is minimized [Ref. 14].

C. THREE – DIMENSIONAL SIMULATIONS

It is important that the shipboard FEL combat system be isolated from shock or vibrations from the ship's deck and hull. The vibrations may lead to an electron beam misalignment, either an offset or a tilt, or to a cavity mirror misalignment. Given a small optical mode waist radius ($W_o = 0.08$ mm), a slight misalignment of the electron beam

could conceivably reduce the overlap between the electrons and the intense optical field in the interaction region.

A given accelerator has a fixed normalized beam emittance,

$$e_n = g\, r_e \bar{q}_o , \tag{4.13}$$

where $\bar{q}_o$ is the electron beam rms angular spread, and r_e is the rms electron beam radius. In most cases, r_e and $\bar{q}_o$ are matched so that the beam does not expand too much as it moves along the undulator [Ref. 13]. For a typical Rayleigh length cavity, a matched electron beam optimizes overlap with the optical mode. In a short Rayleigh length cavity, the electron beam could be focused with additional external magnets along the undulator, decreasing r_e and increasing $\bar{q}_o$. The electron beam focusing optimizes the overlap with the optical mode, which has a very small waist in the interaction region, and thus enhances the gain and efficiency. However, the induced energy spread in the electron beam increases and is given [Ref. 5]

$$\frac{\Delta E}{E} = \frac{\Delta g}{g} = \frac{\Delta v}{4p\, N} , \tag{4.14}$$

where Δv is the induced electron phase velocity spread due to the FEL interaction.

In the simulations presented here, the effects of the electron beam off-axis shift in the *y* direction for a high power FEL with the parameters mentioned in the Tables 1 through 3 are studied. Figure 21 indicates the geometry of the problem. The figure shows the optical mode (blue lines) of a short Rayleigh length undulator inside the optical cavity. The electron beam (red line) is shifted from the undulator axis (green line) by a distance y_o. The experimental design tolerances assume the beam will be aligned to within 0.01 mm of the undulator axis [Ref. 13].

Additionally, the electron beam focusing is studied. Figure 22 shows that the electron beam (red line) is focused to overlap the narrow and intense optical mode (blue line) in the center of the undulator. During the focusing process, the electron beam waist radius r_e is reduced, while the angular spread of the beam is increased in order to keep the emittance constant.

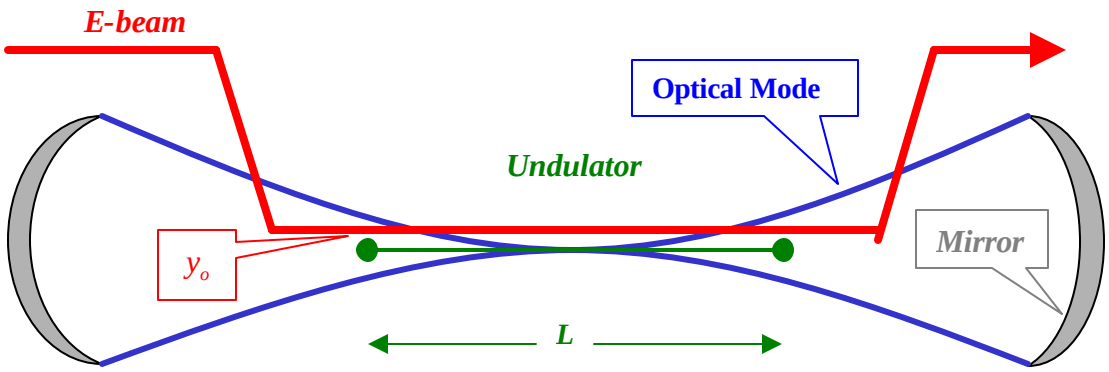

Figure 21. Electron Beam Shift.

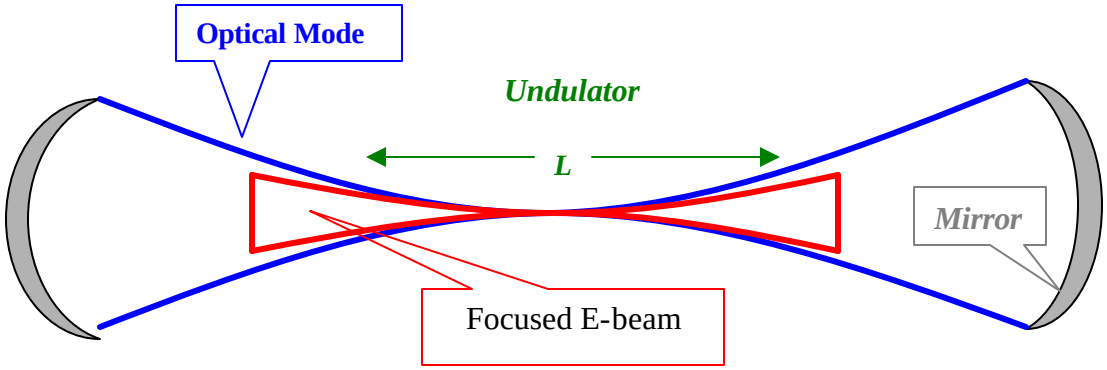

Figure 22. Electron Beam Focusing.

1. Simulation Methods

In a real FEL experiment, an optical wavefront with finite transverse dimensions will have multiple transverse modes determined by the interaction with the electron beam and the mirrors of the optical cavity. The three-dimensional simulations in *x*, *y*, and *t* include the effects of diffraction, optical mode distortion, mirror transmission and edge losses. The undulator is oriented along the *z*-axis, with the magnets normal to the *y*-axis. The simulations use dimensionless coordinates. The longitudinal lengths in the *z* direction are normalized to the undulator length L, the transverse lengths in x and y directions are divided by the characteristic mode radius $(L\,l/p)^{1/2}$, and the angles are divided by $(l/p\,L)^{1/2}$. Thus, the dimensionless parameters for the high power FEL presented here are

DIMENSIONLESS PARAMETERS	
Current Density	$j = 210$
Electron Beam Radius	$s_e = s_x = s_y = r_e / (L l / p)^{1/2} = 0.3$
Rayleigh Length	$z_o = Z_o / L = 0.03$
Mode Waist	$w_o = W_o / (L l / p)^{1/2} = 0.2$

Electron Beam Parameters for a MW level FEL. (From [Ref. 13])

The electrons are given an initial spread in positions (*x*,*y*) and angles (q_x,q_y) determined by the beam radius, beam emittance and focusing. They may also have an offset in position or angle, to study the effects of beam misalignment. They evolve in longitudinal phase space according to the FEL pendulum equation (2.28). In addition, they undergo betatron oscillations in the *yz*-plane. From Equation (4.11), which describes the betatron oscillation for a single electron

$$y(t) = (y_o + \Delta y)\cos\left[w_b\left(t - t_b\right)\right] + \frac{q_{y_o} + \Delta q_y}{w_b}\sin\left[w_b\left(t - t_b\right)\right], \qquad (4.15)$$

where y_o is the initial electron beam offset, q_{y_o} is the initial electron beam tilt, Δy is a random spread in electron position due to emittance and the beam radius r_e, and Δq_y is an electron random angular spread due to emittance also. The dimensionless time $t = ct/L$ corresponds to the electron's position along the undulator axis, and t_b is the position where the electron beam is focused to its minimum size. For the present study, the electron beam is shifted and focused at the undulator center with no tilt, $y_o \neq 0$, $q_{y_o} = 0$, and $t_b = 0.5$. The electron phase velocity will be reduced due to the beam misalignment according to Equation (4.12).

The optical wavefront evolution is described by the parabolic wave equation, starting with an initial Gaussian profile and evolving over many passes until a steady-

state mode is obtained. Then the single-pass extraction efficiency is calculated using Equation (2.33),

$$h = -\frac{\langle \Delta v \rangle}{4p\,N}, \tag{4.16}$$

where $\langle \Delta v \rangle$ is the shift in average electron phase velocity due to the FEL interaction.

2. Three-Dimensional Simulation Output Format

The output from a three-dimensional simulation of the proposed MW level FEL, using a short Rayleigh length of $z_o = 0.03$, is shown in Figure 23. The dimensionless parameters for this experiment appear in the upper-right window. The electron beam has a current density $j = 210$, a radius in both x and y directions of $s_{x,y} = 0.3$, and for this experiment, there is no electron beam shift or tilt (so $y_o = 0$, $q_{y_o} = 0$). At each pass, the electrons are injected with an initial phase velocity $v_o = 10.66$ and zero initial Gaussian spread in phase velocity ($s_G = 0$), which optimizes the extraction efficiency ($h = 2.5\%$).

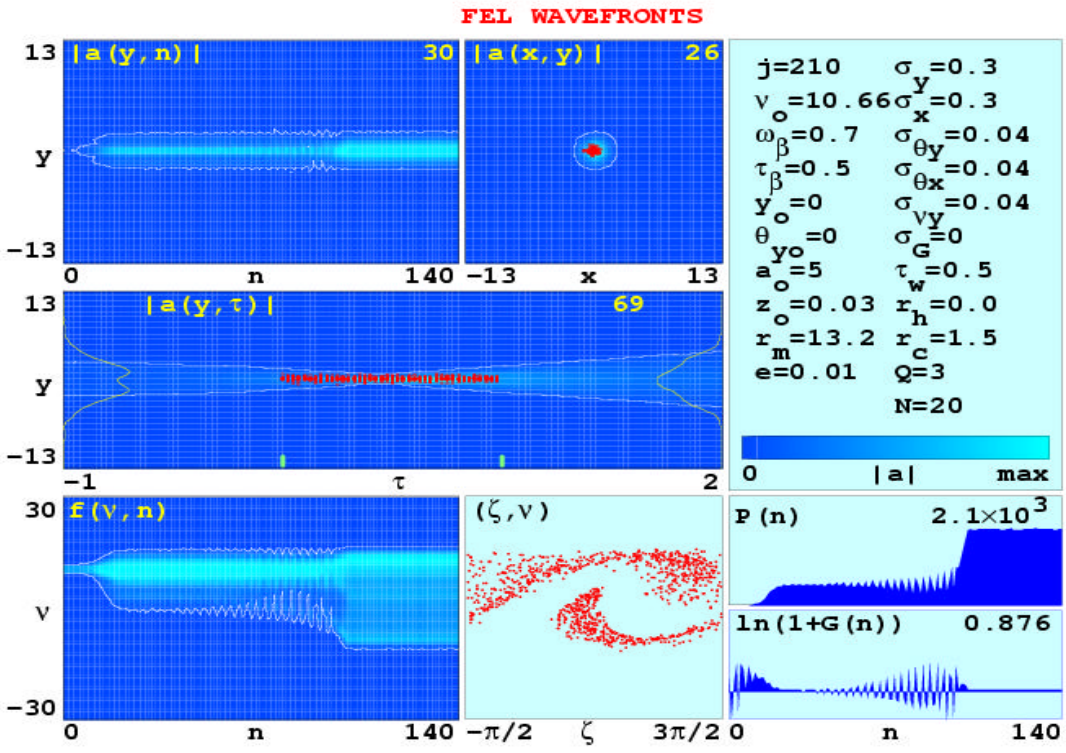

Figure 23. Three-Dimensional Simulation Output for the Proposed MW Level FEL Using a Short Rayleigh Length with a perfectly-aligned Electron Beam.

The electron beam is focused at the undulator center ($t_b = 0.5$) and has an angular spread $s_{q_{x,y}} = 0.04$, which is determined by the matching requirement $s_{q_{x,y}} = w_b^2 s_{x,y}^2$ [Ref. 14]. The dimensionless mirror radius is $r_m = 13.2$, which allows 1% (e=0.01) edge losses per pass, and the dimensionless radius of curvature is $r_c = 1.5$, determining the Rayleigh length [Ref. 14]. The color intensity scale, shown on the right, is used for the optical field amplitude intensity plots. The scale runs from dark blue, corresponding to zero amplitude, to light blue, corresponding to maximum amplitude. The white contour line corresponds to a field amplitude at 5% of the maximum value.

The upper portion of the figure shows two intensity plots of the optical field. At the upper left is the side view of a slice through the optical wavefront as the field $|a(y,n)|$ evolves over $n = 140$ passes. The one in the upper center represents the spot of the final wavefront at the undulator exit $|a(x,y)|$ after $n = 140$ passes. In the same wavefront plot, the red dots show the position of sample electrons, indicating any offset or misalignment of the beam. The center plot presents a side view of a slice through the optical wavefront $|a(y,t)|$ during the final pass. The red dots correspond to sample electrons as they move from the beginning of the undulator ($t = 0$) to the end ($t = 1$). The optical wave amplitude profile, corresponding to the power distribution at the mirrors, is shown with the yellow contour lines. In this simulation, the mirror separation is only three times the undulator length, for numerical convenience.

The simulation starts with a weak optical field amplitude of $a_o = 5$ and after about 100 passes saturates to its final value of $|a| = 69$. This is also shown in the lower right plot of the optical power $P(n)$ and gain $G(n)$ evolution, where the oscillator saturates after about 100 passes. The lower left plot is the evolution of the electron spectrum $f(v,n)$. Here, it is shown that the initial electron phase velocity is $v_o = 10.66$. It is also shown that the energy spread of the electron beam increase due to the FEL

interaction until the laser saturates. The last plot in the lower center shows the final electron phase-space evolution where evidence of bunching is shown.

3. Simulation Results

a. Electron Beam Shift

The simulations for the MW level FEL design are run using a short Rayleigh length for various electron beam shifts y_o. The normalized electron beam shift was varied from $y_o = 0$ to $y_o = 1$ in steps of 0.1. As mentioned previously in this chapter, the experimental design tolerance assumes that the beam will be aligned to within 0.01 mm of the undulator axis. The normalized beam shift that corresponds to 0.01 mm is $y_o = 0.023$. At each value of y_o, the initial phase velocity v_o was also varied, in order to determine the peak efficiency $\hat{h}$. The efficiency is calculated according to Equation (4.16) after steady-state is reached.

The steady-state FEL efficiency h versus the initial phase velocity for four values of the normalized electron beam shift ($y_o = 0, 0.2, 0.4, 0.6$) is plotted in Figure 24.

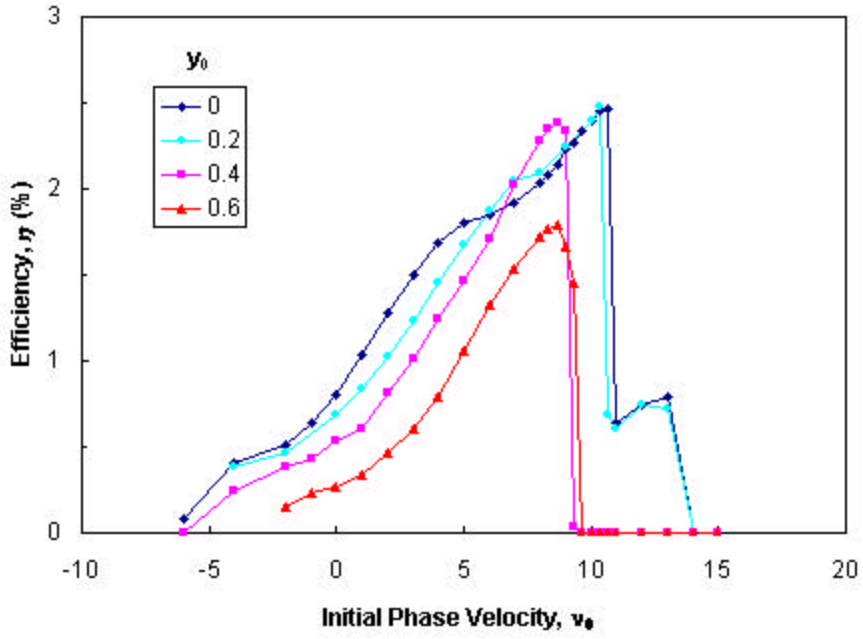

Figure 24. Single-Pass Extraction Efficiency h Versus the Initial Phase Velocity v_o for Four Values of the Normalized Electron Beam Shift y_o.

For each value of the electron beam shift, the efficiency steadily increases as the phase velocity increases, with a sharp drop-off just after the peak. The peak corresponds to the value of v_o where the FEL gain drops below threshold. It can be seen that with no electron beam shift ($y_o = 0$), the FEL has the highest peak efficiency of $\hat{h} = 2.5\%$, which corresponds to initial phase velocity $v_o = 10.66$. This was expected to be the peak, since for zero shift, the electron beam is almost perfectly aligned with the optical mode. The peak efficiency decreases as the electron beam is shifted from the undulator axis. Additionally, the electron beam shift changes the initial phase velocity for which the laser reaches the peak efficiency. However, the phase velocity varies with the optical wavelength as $\Delta v = 2pN(\Delta l / l)$. Thus, an electron beam shift can change the optical wavelength.

Figure 25 shows the output of a single simulation with the electron beam shifted off-axis by $y_o = 0.6$. The FEL interaction takes place close to the undulator center as the electron moves toward the end of the undulator. The electron beam is not aligned with the intense optical mode in the interaction region due to the beam shift. This causes the optical mode to tilt, which is obvious in the $|a(y,t)|$ plot. Nevertheless, the optical power $P(n)$ reaches steady-state, but the extraction efficiency is reduced from 2.5% to 1.8%. The phase velocity is reduced according to Equation (4.12) by $\Delta v = -w_b^2 y_o^2 \approx 0.2$.

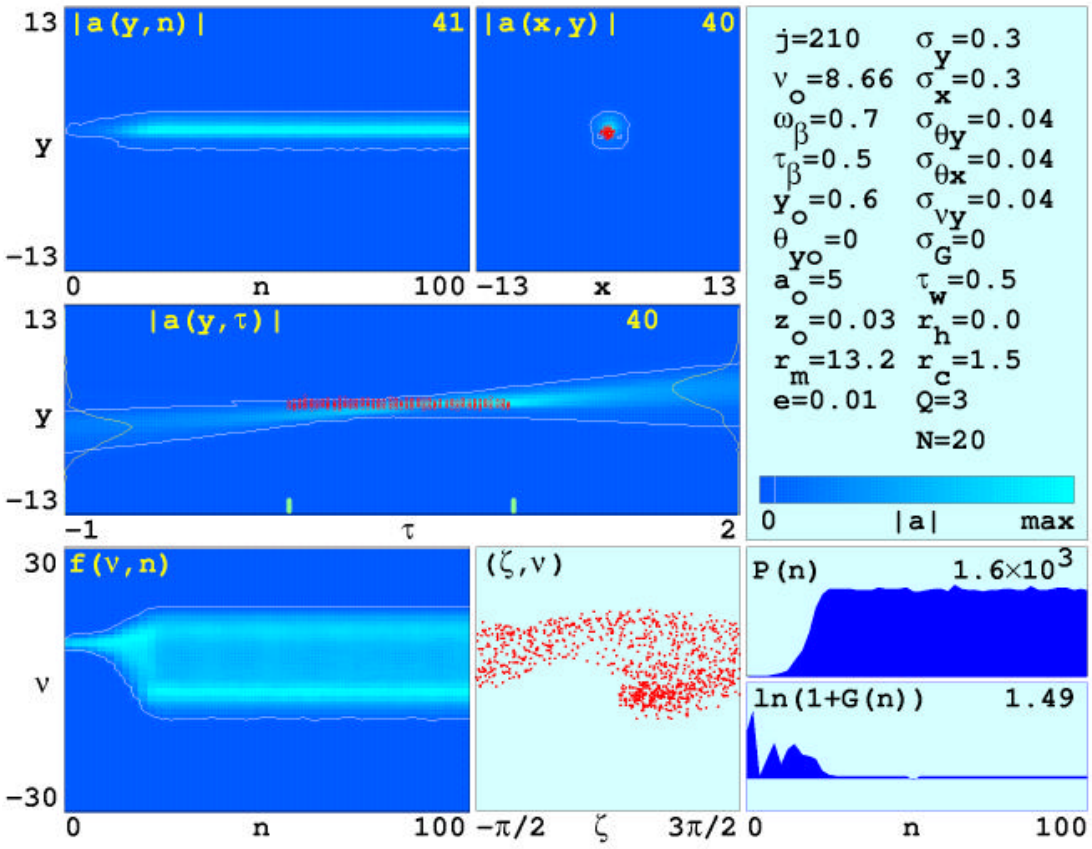

Figure 25. Three-Dimensional Simulation Output for the Proposed MW Level FEL Using a Short Rayleigh Length with an Electron Beam Shift $y_o = 0.6$.

Figure 26 summarizes the results of the simulations. It shows the peak single-pass extraction efficiency versus the normalized electron beam shift varied from $y_o = 0$ to $y_o = 1$ in steps of 0.1.

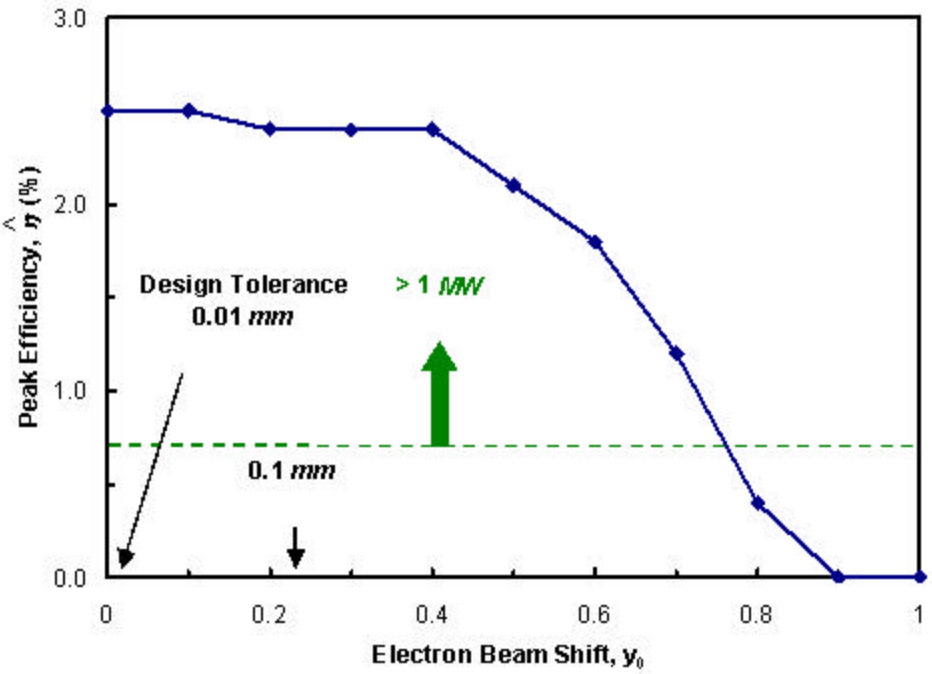

Figure 26. Peak Single-Pass Extraction Efficiency $\hat{\eta}$ Versus the Normalized Electron Beam Shifts y_o.

In this figure, the normalized shift that corresponds to 0.1 mm is indicated for reference by an arrow on the horizontal axis at $y_o = 0.23$. In the same way, the normalized experimental design tolerance that corresponds to 0.01 mm beam shift is indicated at $y_o = 0.023$. The required efficiency to achieve the 1 MW goal is indicated by a dashed line at $\hat{\eta} = 0.7\ \%$. Here, it is once more clear that the peak efficiency steadily decreases, as the beam is further offset from the undulator axis, but remains above the goal for $y_o \le 0.75 (\approx 0.3\text{mm})$. This value is well beyond the design tolerance of $y_o = 0.023 (0.01\text{mm})$.

Additionally, as was presented by the NPS FEL group at the 25th International FEL Conference of 2002 in Argonne, IL, the electron beam tilt ($q_{y_o} \neq 0$)

with no offset shift ($y_o = 0$), gives similar results [Ref. 13]. The efficiency remains above the 0.7% extraction efficiency goal for $q_{y_o} \le 8(6\text{mrad})$ when the beam is tilted about the undulator center ($t_b = 0.5$), and for $q_{y_o} \le 1.5(1\text{mrad})$ when the beam is tilted about the undulator entrance ($t_b = 0$). Both values of the electron beam tilt are well beyond the design tolerance of $20\ \mu\text{rad}$, which corresponds to normalized $q_{y_o} = 0.03$. Thus, it can be concluded that the shipboard MW level FEL design is unaffected by any electron beam misalignment (an offset or a tilt) due to vibrations, if the system is isolated within the previously mentioned design tolerances.

b. Electron Beam Focusing

All the results presented so far have used a matched electron beam, without using any focusing to enhance the overlap between the electron beam and the optical mode. The beam can be focused, by varying the electron beam waist radius r_e, while keeping the total current and emittance fixed. In the simulations, the normalized electron beam radius $s_e = r_e / (L l / p)^{1/2}$ is used.

Figure 27 shows the simulation results for the peak efficiency $\hat{h}$ versus the normalized electron beam radius, which is varied from $s_e = 0.3$ to 0.15 in steps of 0.05. The normalized beam radius that corresponds to 0.1 mm is indicated by an arrow on the horizontal axis at $s_e = 0.23$. The largest value of $s_e = 0.3$ corresponds to a matched beam for the parameters of this FEL design. As s_e is reduced by focusing the beam, the peak efficiency increases from $\hat{h} = 2.5\%$ to 4 %, which is far beyond the goal value of 0.7 %. This indicates that it may be possible to reduce the average current and still obtain the goal of 1 MW output power. In the same figure, the induced energy spread is also shown, which is given by Equation (4.14). The energy spread needs to be kept below the maximum allowable limit for safe electron beam recirculation of about 15 % [Ref. 15]. The results indicate that the induced energy spread increases from 11% to 14% as the beam is focused from $s_e = 0.3$ to 0.15.

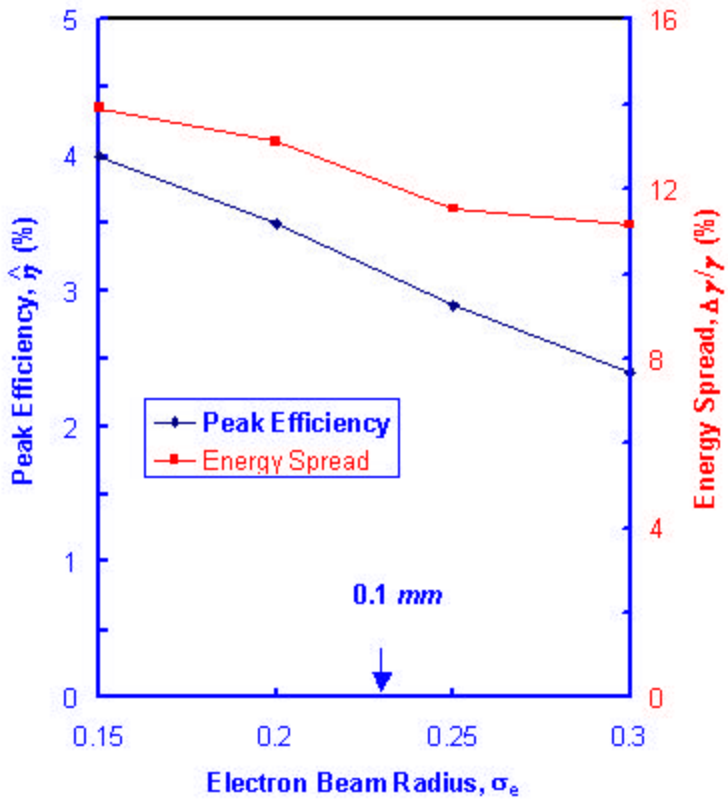

Figure 27. Peak Single-Pass Extraction Efficiency $\hat{\eta}$ and Induced Energy Spread $\Delta E/E$ Versus the Normalized Electron Beam Shifts y_o.

Figure 28 shows the output of a single simulation where the electron beam is focused to $s_e = 0.15$. Since the electron beam radius has been reduced by a factor of 2, the electron density r is increased by a factor of 4. The dimensionless beam current density $(j \propto r)$ is likewise increased by a factor of 4 to $j = 840$. The electron beam angular spread is also increased according to the requirement $s_{q_{x,y}} = w_b^2 s_{x,y}^2 = 0.16$ to keep the emittance constant. Beginning with an initial velocity $v_o = 12.8$ and initial optical field amplitude of $a_o = 20$, the optical power $P(n)$ reaches a steady-state after ≈ 50 passes.

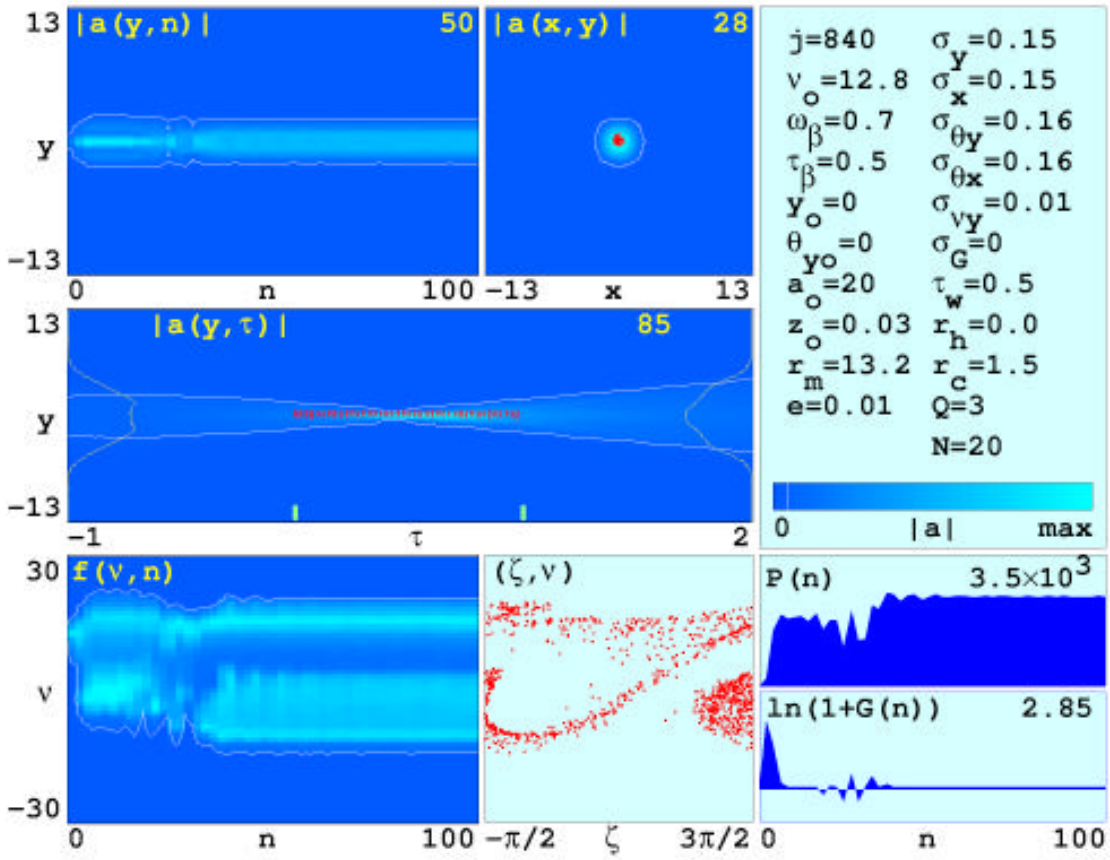

Figure 28. Three-Dimensional Simulation Output for the Proposed MW level FEL Using a Short Rayleigh Length and Focused Electron Beam.

The initial phase velocity increased from $v_o = 12.8$ to 13 when the simulation was run again as presented in Figure 29. This change represents a very small change (0.1%) in optical wavelength. This time the optical mode $|a(y,t)|$, the optical power $P(n)$, and the extraction efficiency oscillate over many passes, without reaching a steady-state condition. The complicated pattern of the $|a(y,t)|$ plot shows the presence of multiple transverse optical modes in the cavity. The laser has not reached a steady-state after even 600 passes, but expresses an extended oscillatory behavior.

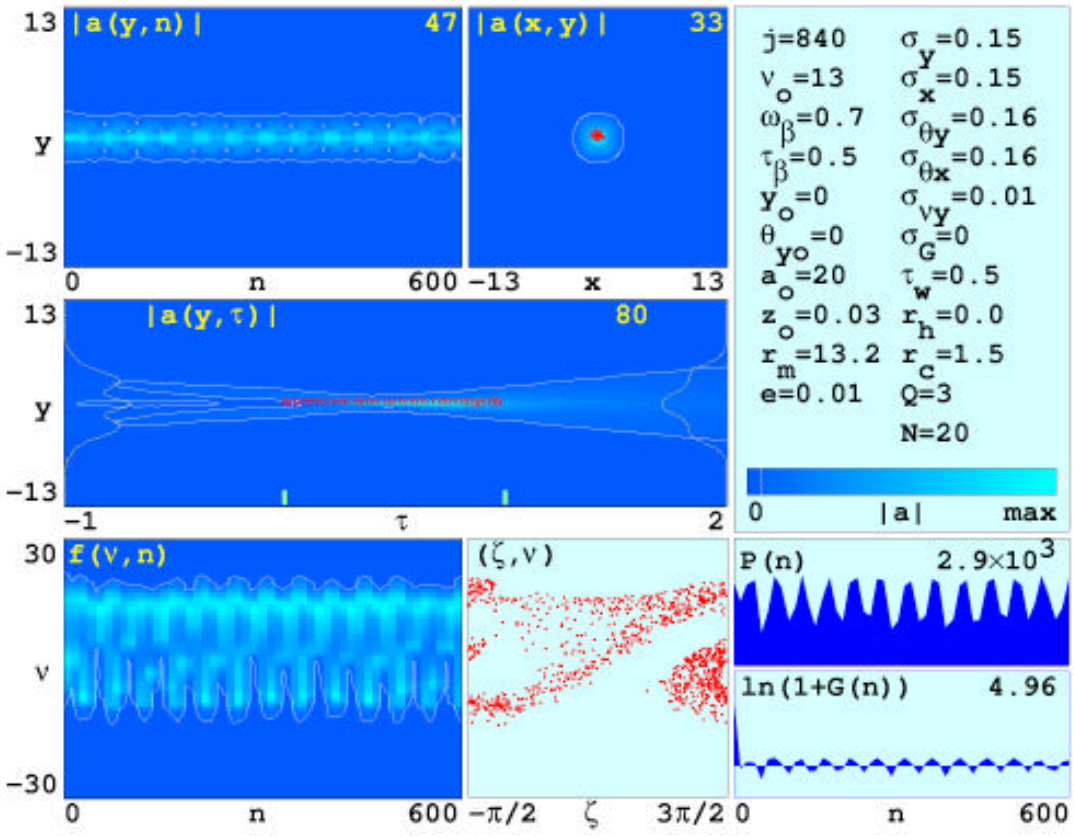

Figure 29. Three-Dimensional Simulation Output for the Proposed MW Level FEL Using a Short Rayleigh Length and Focused Electron with Extended Oscillations.

D. CONCLUSIONS

The proposed FEL weapon design uses a short Rayleigh length undulator to increase the optical beam spot size at the mirrors. But a short Rayleigh length implies a small optical mode waist in the center of the cavity. A slight misalignment of the electron beam reduces the overlap between the electrons and the optical mode in the interaction region, resulting in less gain and efficiency. Using three-dimensional simulations, it is found that the shipboard MW level FEL design is unaffected by any electron beam misalignment (an offset or a tilt) due to vibrations, if the system is isolated within the expected design tolerances. It is also found that that the electron beam focusing enhances the FEL extraction efficiency.

Next chapter presents the simulation results of the upgraded to 100 kW Thomas Jefferson National Accelerator Facility (TJNAF) FEL using a step-tapered undulator.

THIS PAGE INTENTIONALLY LEFT BLANK

V. SIMULATIONS OF THE 100 KW TJNAF FEL USING A STEP-TAPERED UNDULATOR

A. INTRODUCTION

The Thomas Jefferson National Accelerator Facility (TJNAF) has developed and demonstrated the most powerful FEL in the world, with an average output power of 2 kW that is tunable in the infrared. This output power is not considered enough for a military DEW weapon system. But a major upgrade of the TJNAF FEL system to 10 kW is underway, and further extension of the system to 100 kW has already been proposed. This begins to open a credible path to the desired MW level FEL [Ref.1].

A schematic representation of the TJNAF FEL was shown in Figure 5 of Chapter II. The system recirculates the electron beam to recover the excess energy of the electron beam. It extracts the maximum energy from the electron beam in a single pass through the undulator while inducing the minimum amount of energy spread for beam recirculation (energy spread $\Delta g/g < 15\%$).

At the Naval Postgraduate School, in collaboration with TJNAF, we have explored the use of a step-tapered undulator. This undulator design alters undulator field in order to alter the resonance condition halfway through the undulator to improve the performance of the proposed 100 kW TJNAF FEL. The use of short electron pulses complicates the desired interaction. The results of the experiment were presented during the 23rd International FEL Conference of August 2001 in Darmstadt, Germany [Ref. 16].

B. STEP-TAPERED UNDULATOR

Unlike the conventional undulator, which has a periodic field and wavelength, the step-tapered undulator abruptly changes the value of the field and therefore the undulator parameter *K* halfway through the undulator. This could be done by having two separate undulator segments, each with different value of the magnetic field and *K*.

A step-tapered undulator results in a modified pendulum equation [Ref. 5, 14–16]

$$\overset{\circ}{v} = \overset{\circ\circ}{z} = \Theta\left(t - \frac{1}{2}\right)\Delta + a\cos\left(z + f\right), \tag{5.1}$$

where $z = (k + k_o)z - wt$ is the electron phase, k is the optical wavenumber, $k_o = 2p/l_o$ is the undulator wavenumber, w is the optical frequency, v is the electron phase velocity, f is the optical phase, a is the dimensionless optical field amplitude, $\Theta(z)$ is the step function,

$$\Theta(z) = \begin{cases} 0, & z < 0 \\ 1, & z \geq 0 \end{cases}, \tag{5.2}$$

and Δ is the phase acceleration caused by the step taper $\Delta K/K$ at $t = z/N l_o = 0.5$ along the undulator and is equal to

$$\Delta = -\left(\frac{4p\,NK^2}{1+K^2}\right)\left(\frac{\Delta K}{K}\right). \tag{5.3}$$

Thus the stepped field is decreased when $\Delta > 0$, or increased when $\Delta < 0$.

C. 100 KW TJNAF FEL PARMETERS

The TJNAF FEL can be upgraded to operate at increased output power of 100 kW by increasing the kinetic energy of the electron beam from the accelerator to $K_e = 210\text{MeV}$. The electron beam consists of pulses with length $l_e = 0.1\text{mm}$, pulse repetition frequency $\Omega = 750\text{MHz}$, and peak current $\hat{I} = 270\,\text{A}$. The average electron beam power would then be

$$P_e = \frac{K_e \hat{I} \Omega l_e}{c} = 14\text{MW}. \tag{5.4}$$

So an output optical power of 100 kW requires an extraction efficiency of $h \approx 0.7\%$. The undulator period is $l_o = 8$ cm over $N = 36$ periods with an rms undulator parameter $K = 1.7$.

The electron beam is described by dimensionless peak current $j = 5$ and dimensionless electron pulse length $s_z = l_e/N l = 3$. The resonator quality factor is $Q_n = 4.2$, which corresponds to cavity losses per each pass of $1/Q_n = 24\%$.

D. STEADY STATE POWER

To study this FEL, we run the simulations starting with a weak optical field $(a < p)$ for many passes until the power reaches a steady state condition. The step-taper

is varied from $\Delta = -2p$ to $\Delta = 2p$ in steps of p. At each value of Δ, the desynchronism $d = -2\Delta S / Nl$ is also varied, in order to determine the peak efficiency (Equation 4.16) and study the pulse slippage effects. The desynchronism, as we have seen earlier in Chapter II, measures the shortening of the resonator cavity length by ΔS compared to the slippage distance Nl. Specifically, the desynchronism between the electron pulse and the optical pulse is varied from $d = 0$ to $d = 0.3$.

The steady-state efficiency versus the desynchronism for a step-tapered undulator is plotted in Figure 30. The required efficiency to achieve the 100 kW is indicated by a dashed line at $h = 0.7\%$. From this figure, it is obvious that we obtain the target efficiency and power with the conventional undulator with no taper ($\Delta = 0$), or with a negative step-taper undulator of $\Delta = -p$. The desynchronism is within the interval $d = 0.03$ to 0.07, with the best results for $d = 0.04$. For the first case ($\Delta = 0$), the efficiency reaches the value of 0.8%. For the negative taper ($\Delta = -p$), the efficiency is increased to 0.86% which corresponds to an output power of 116 kW. For larger absolute values of tapering or for values of desynchronism out the interval $0.03 < d < 0.07$, the efficiency remains below the target value.

The same figure verifies that at exact synchronism between the electron and the optical pulses ($d = 0$) there is no output power. Increasing *d* by a small amount, there is a sharp rise in the output power until the peak point of $d = 0.04$ for these parameters. Increasing *d* beyond this point, the power slowly drops off, until eventually there is again no output power.

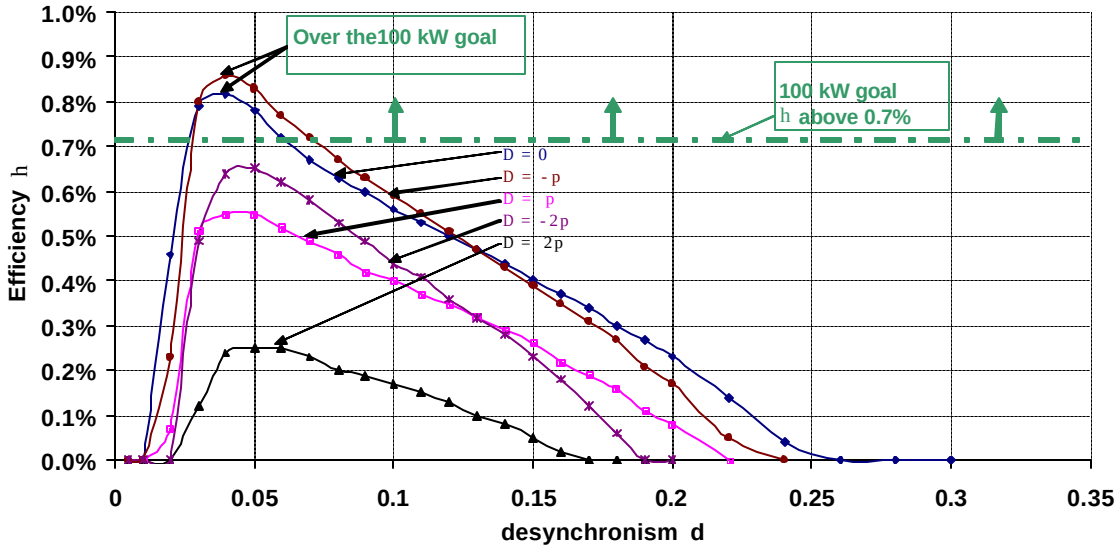

Figure 30. Efficiency h Versus Desynchronism d for Step-taper with $Q_n = 4.2$

Figure 31 presents a simulation output for $\Delta = -p$ with a desynchronism value of $d = 0.04$. The lower-left window shows the parabolic electron pulse position at $t = 0$ and $t = 1$. The middle-left window corresponds to the field $|a(z,n)|$ evolution over $n = 500$ passes with the final pulse shape $|a(z)|$ shown in the upper left window. The color intensity scale is located on the top of this window and represents the optical field amplitude with the largest value of $|a(z)| = 15.69$ shown as red and zero as blue. The white contour line corresponds to a field amplitude of 50% of its maximum value.

The middle lower window shows the weak field gain spectrum $G(v)$. The window above that represents the evolution of the optical power spectrum $P(v,n)$ over $n = 500$ passes with the final power spectrum $P(v)$ shown on the top window. The triangular tick mark indicates the initial resonance wavelength, and the rectangular tick mark represents the center of the final spectrum.

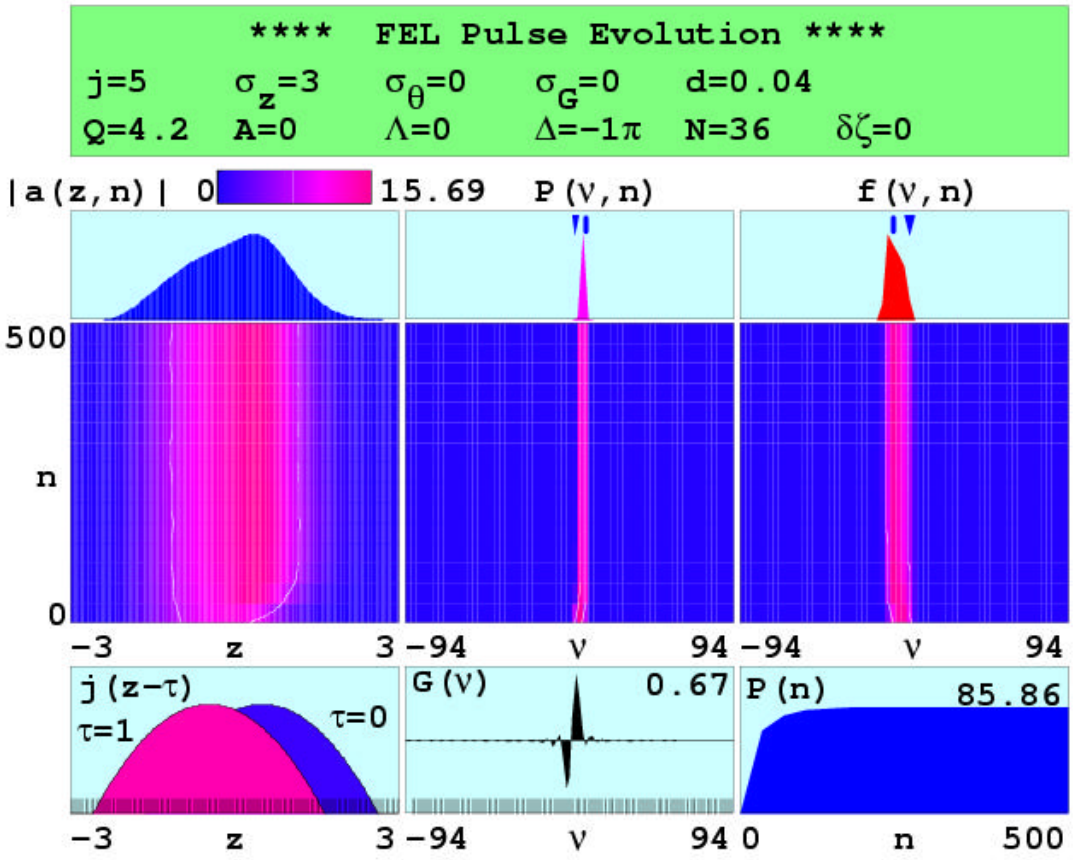

Figure 31. Simulation output for inverse step-tapered undulator.

At the lower right window we have the dimensionless optical power evolution plotted after each pass over 500 passes. The optical power reaches a steady-state after $n \approx 50$ passes. The middle-right window shows the evolution of the electron spectrum $f(v,n)$ over $n = 500$ passes with the final electron spectrum $f(v)$ shown on the window above it. Once more, the triangular tick mark indicates the initial resonance phase velocity and the rectangular tick mark represents the center of the final spectrum.

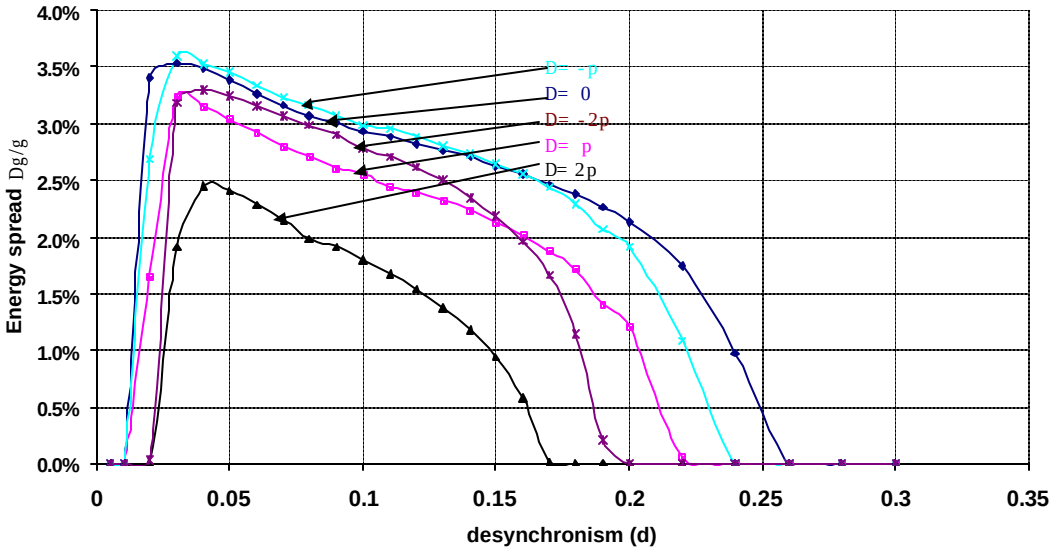

Figure 32. Energy Spread $\Delta g/g$ Versus Desynchronism for Step-tapered Undulator.

The slight improvement obtained with a small negative taper leads to a small increase of the induced energy spread $\Delta g/g$ (Equation 4.14). Figure 32 plots the energy spread versus the desynchronism for various values of step-taper. The maximum values of the energy spread are found for conditions where the maximum efficiency occurs. For no taper $(\Delta = 0)$ and for $\Delta = -p$, the energy spread becomes $\Delta g/g = 3.5\%$ and $\Delta g/g = 3.8\%$ respectively. Both values are well below the limit of 15% required for electron beam recirculation.

We considered the possibility of decreasing undulator losses to improve FEL performance. The small values of the induced energy spread allow increasing the quality factor Q_n from 4.2 to 10. The new resonator cavity has only 10% losses per pass leading to larger efficiency values that exceed 1% for some values of Δ and d. Specifically, in the $\Delta = -p$ case, the efficiency increases from 0.9% to 1.4%. With larger Q_n only for values of $\Delta = \pm 4p$ and for $d > 1.2$ did the FEL failed to exceed the efficiency limit of 0.7% [Ref. 16].

In conclusion, the simulation results of the upgraded to 100 kW TJNAF FEL show that there is a slight improvement in efficiency with a small negative taper and the induced energy spread stays well below the 15% limit for the parameters investigated. In contrast, previously published results showed as much as a 75% efficiency enhancement with a negative step-tapered undulator based on simulations and experimental results from CLIO and FELIX [Ref. 16]. The results of our research show that the step-taper cannot always be as effective as found earlier, and that an FEL must be far into strong field saturation before tapering can extend the saturation limit.

In the next Chapter the solid-state laser is studied. The physics behind the solid-state lasers is first discussed. Accordingly, their potential to be developed as directed energy weapon systems is presented.

THIS PAGE INTENTIONALLY LEFT BLANK

VI. SOLID STATE LASER

A. INTRODUCTION

The solid-state laser is an optical oscillator. It consists of a power supply, a resonant optical amplifier and a feedback loop, as shown in Figure 33. An input signal is essential to starting the lasing process. The input is amplified and the output is fed back to the input with matching phase, where it undergoes further amplification. This process continues until the amplifier gain saturates and the system reaches a steady state with an output signal at the resonant frequency of the amplifier.

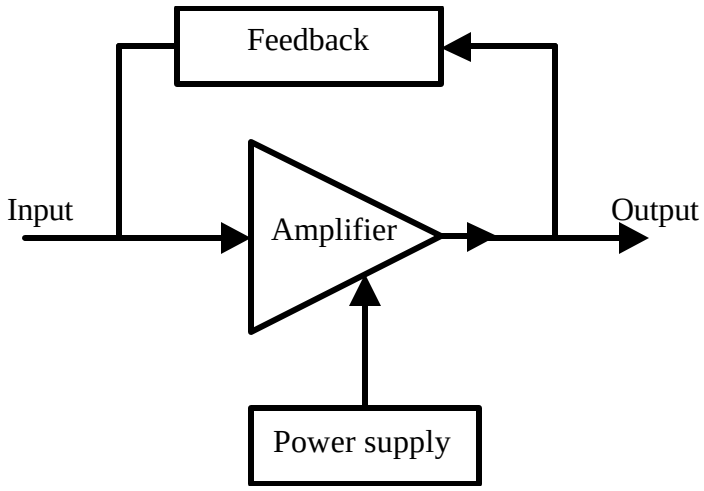

Figure 33. An Optical Oscillator. (After [Ref. 17]).

An optical amplifier is a device that increases the amplitude of an optical field. If the amplification takes place while maintaining the optical field's phase, the amplifier is coherent and is the result of a process called stimulated emission of radiation. In this process, atoms, or ions at an upper energy level, are stimulated by photons to emit their excess energy to the input optical field coherently. Thus, the photon of the input light stimulates the atom in an upper energy level to undergo a transition to a lower energy level and emit an identical photon at the same frequency, phase, and polarization, propagating in the same direction. The process is continuously repeated, resulting in coherent light amplification. The frequency of the amplified coherent light is determined by the energy level difference of the amplifier material.

An essential ingredient for achieving laser amplification is the presence of a greater number of atoms in the upper energy level than in the lower level of the amplifier material. This is called a population inversion and is induced by the power supply, which excites the atoms to the higher energy level. This is a pumped active medium. The feedback is achieved by placing the gain medium in an optical cavity with two reflecting mirrors. The output is accomplished by making one of the mirrors partially transmitting or by constructing an unstable optical cavity. The modes of oscillation in the cavity or the frequency selection of the light amplification depend on the amplifier and on the resonator. The components of a laser are shown in Figure 34.

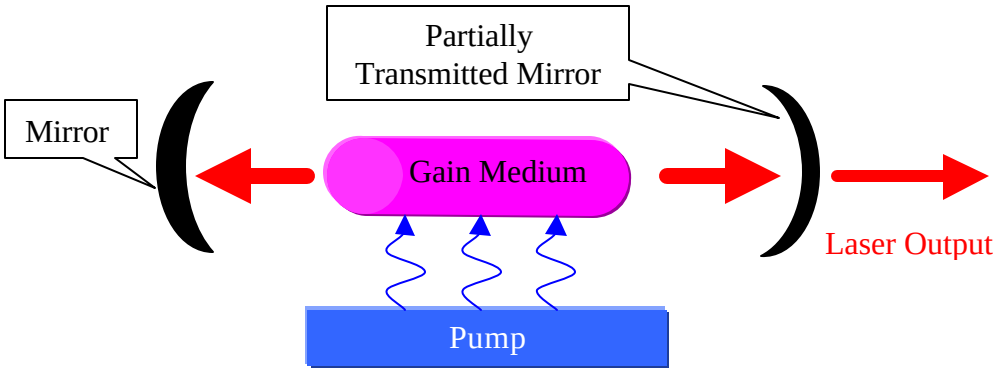

Figure 34. Basic Components of a Laser.

The solid-state lasers use solid-state material as a gain medium that can be electrically or optically pumped. The most common types are the neodymium-doped yttrium-aluminum garnet laser amplifier (Nd:YAG), the ruby (Cr^{3+}:Al_2O_3) laser amplifier, and the erbium-doped (Er^{3+}:Silica Fiber) laser amplifier. The lasing frequencies extend from the visible range to the mid-infrared while the average output power can be scaled to high powers (~100 kW).

B. BASIC SOLID STATE LASER PHYSICS

1. Radiative Processes

Quantum theory considers the discrete energy levels in atoms and ions. The laser is a quantum device that is based on the interaction between the photons and the atoms placed in a resonator.

The atomic transition between two discrete energy levels, E_1 and E_2, results in a radiation of a frequency f_o, where $hf_o = E_2 - E_1$. In a laser, there are three radiative processes possible: spontaneous emission, absorption, and stimulated emission.

Spontaneous emission is the process where atoms that are initially in an upper energy level E_2 decay spontaneously to a lower state E_1, releasing their excess of energy in the form of photons. This transition is independent of the number of photons that already exist in the same mode. If the population density in state 2 is N_2, then the decay rate of this state will be

$$\frac{dN_2}{dt} = -A_{21}N_2, \tag{6.1}$$

where A_{21} is known as the Einstein's A coefficient. The A coefficient represents the number of transitions/sec, and is equal to the inverse time constant t_o, known as the spontaneous emission lifetime of the transition from state 2 to state 1. The inverse of the spontaneous emission lifetime expresses the probability density of spontaneous emission [Ref. 17].

Absorption is the process where an atom in the lower state 1 absorbs a photon from the incident field and transits to a higher energy state 2. The rate of this process depends on the absorbing material and the incident field,

$$\frac{dN_2}{dt} = B_{12}N_1 r(f) = -\frac{dN_1}{dt}, \tag{6.2}$$

where N_1, N_2 are the population densities in states 1, 2, respectively, B_{12} is known as the Einstein's B coefficient, and $r(f)$ is the spectral energy density of the electromagnetic field inside the cavity which is given by

$$r(f) = \frac{8\pi f^2}{c^3}\frac{hf}{e^{hf/kT_e} - 1} = \frac{8\pi hf^3}{c^3}\frac{1}{e^{hf/kT_e} - 1}, \tag{6.3}$$

$$< E >= \frac{hf}{e^{hf/kT_e} - 1}, \tag{6.4}$$

where k is the Boltzmann's constant, h is the Planck's constant, c is the light's propagation speed, and $<E>$ is the average energy per mode in thermal equilibrium.

Stimulated emission is a reverse process of absorption, where the atom is in the upper energy level and is stimulated to emit a photon into the same mode of the incident field, resulting in coherent photon amplification. The rate of the stimulated emission process is given by

$$\frac{dN_2}{dt} = -B_{21}N_2 r(f) = -\frac{dN_1}{dt}. \tag{6.5}$$

These three radiative processes are shown in Figure 35.

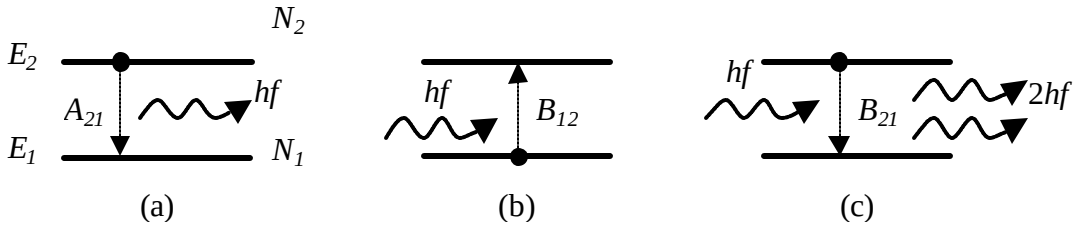

Figure 35. (a) Spontaneous Emission (b) Absorption (c) Stimulated Emission.

The total rate of change of the population in state 2 or in state 1 of the material as a result of the radiative process is the sum of Equations (6.1), (6.2), and (6.5),

$$\frac{dN_2}{dt} = -A_{21}N_2 + B_{12}N_1 r(f) - B_{21}N_2 r(f) = -\frac{dN_1}{dt}. \tag{6.6}$$

At thermal equilibrium, the total rate must be zero, and Equation (6.6) provides the ratio of the population of the two states,

$$\frac{N_2}{N_1} = \frac{B_{12}r(f)}{A_{21} + B_{21}r(f)}. \tag{6.7}$$

The ratio of the population of the two states according to the Boltzmann probability distribution is given by,

$$\frac{N_2}{N_1} = \frac{g_2}{g_1} e^{-hf/kT_e}. \tag{6.8}$$

The degeneracy parameters g_1, g_2 represent the number of states corresponding to the energy levels E_1 and E_2 respectively. If Equations (6.7) and (6.8) are combined, solved for $r(f)$ and set that value equal to Equation (6.3), the relation between the Einstein's coefficients will be given as,

$$\frac{B_{12}}{B_{21}} = \frac{g_2}{g_1}, \tag{6.9a}$$

$$\frac{A_{21}}{B_{21}} = \frac{8p\,hf^3}{c^3}. \tag{6.9b}$$

2. Spectral Line Widths

In reality, a system consists of many atoms and there is an inherent uncertainty in state energies due to finite upper state lifetimes, Doppler shift of moving atoms, and collisions between the atoms. This means that there is a distribution of energies around the mean values of state energies, as shown in Figure 36a, and the atomic emission or absorption has a relative narrow spectral distribution. Thus, the system emits or absorbs radiation in a narrow band of frequencies of width Δf. This relative distribution is called the lineshape function $g(f)$ and represents the relative strength of the atomic interaction with photons of different frequencies. The lineshape function is centered at central frequency f_0 and is normalized so that

$$\int_0^\infty g(f')df' = 1. \tag{6.10}$$

Therefore, transitions are most likely to occur for photons of frequencies $f \approx f_o$. The width of the function $g(f)$ is the transition linewidth Δf and is defined as the width of $g(f)$ at its half maximum value (FWHM). The function $g(f)$ is shown in Figure 36b.

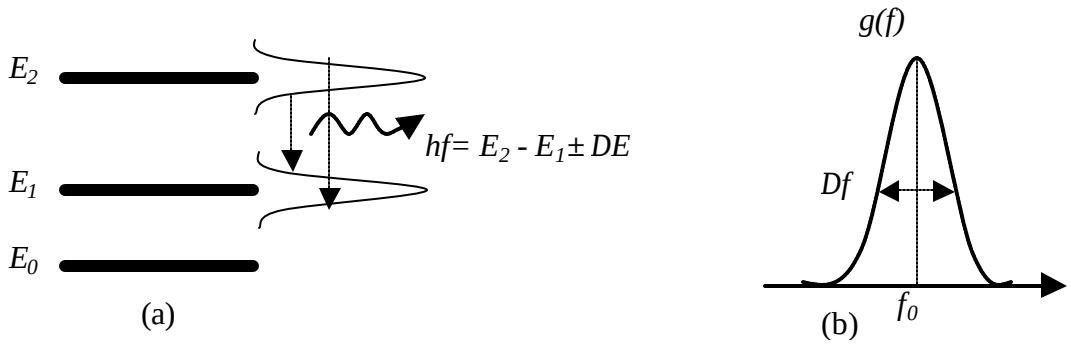

Figure 36. (a) Energy Level Diagram (b) Lineshape Function *g(f).*

The atoms in the material are not identical, and they have different lineshape functions and even different central frequencies. In this case, the composite lineshape is defined, which is the average lineshape with its peak shifted from either central frequency.

Taking into account finite linewidths, the radiative rate Equation (6.6) for N_2 becomes

$$\frac{dN_2}{dt} = -A_{21}N_2\int_0^\infty g(f')df' + B_{12}N_1\int_0^\infty r(f')g(f')df' - B_{21}N_2\int_0^\infty r(f')g(f')df'. \quad (6.11)$$

Assume that the spectral width $r(f)$ is very small compared to $g(f)$. So $r(f)$ can be approximately represented as a $d-$function, $r(f) \approx r_f d(f'-f)$. Then the rate equation becomes

$$\frac{dN_2}{dt} = -A_{21}N_2 + B_{12}N_1 r_f g(f) - B_{21}N_2 r_f g(f). \quad (6.12)$$

Combining the last equation with Equations (6.9a) and (6.9b), we get

$$\frac{dN_2}{dt} = -A_{21}N_2 - \left[N_2 - \frac{g_2}{g_1}N_1\right]\frac{I_f}{hf}s(f), \quad (6.13)$$

where $I_f = r_f(c/n)$ is the light's intensity, n is the index of refraction of the material, and $s(f)$ is the stimulated emission cross section area,

$$s(f) = A_{21}\frac{l^2}{8\pi n^2}g(f). \quad (6.14)$$

3. Laser Amplification

Light transmitted through a material in thermal equilibrium is attenuated due to absorption by the large population in the lower energy level. With the population inversion where $N_2 > N_1$, a nonequilibrium situation is achieved and therefore laser amplification is possible due to stimulated and spontaneous emission.

Let I_f be the incident light intensity to the amplifier material of length dz. The incremental emitted intensity dI_f from within that length will be

$$\frac{dI_f}{dz} = -hf\frac{dN_2}{dt}. \tag{6.15}$$

The radiation due to spontaneous emission is spread uniformly into a solid angle of $4p$ steradians. Therefore, of the spontaneously emitted photons, only those in a solid angle $d\Omega$ are in the correct direction and only half of that fraction has the proper polarization. Thus, Equation (6.15) can be rewritten,

$$\frac{dI_f}{dz} = hf\left[\frac{1}{2}\frac{d\Omega}{4p}N_2A_{21} + \left(N_2 - \frac{g_2}{g_1}N_1\right)\frac{I_f}{hf}s(f)\right]. \tag{6.16}$$

If considering only the coherent amplification and ignore the spontaneous emission, we have

$$\frac{dI_f}{dz} = \left(N_2 - \frac{g_2}{g_1}N_1\right)s(f)I_f \equiv g(f)I_f, \tag{6.17}$$

where $g(f)$ is the gain coefficient and represents the net gain in the light intensity per unit length of the medium. The solution of Equation (6.17) is the exponentially increasing function,

$$I_f(z) = I_f(0)e^{zg(f)}. \tag{6.18}$$

It is obvious that the gain coefficient is $g(f)$ proportional to the population difference of the two energy levels. With population inversion, the gain coefficient is positive and there is light amplification. In the absence of population inversion, the gain

coefficient is negative and the medium will attenuate rather than amplify the light traveling though it.

For a total length L of the material, the overall gain $G(f)$ of the laser amplifier is the ratio of the light intensity at the output to the light intensity at the input, so that,

$$G(f) = e^{Lg(f)}. \tag{6.19}$$

From Equations (6.14), (6.17), and (6.19), it is obvious that the gain coefficient $g(f)$ and the gain $G(f)$ are proportional to the lineshape function $g(f)$ and are dependent on the frequency of the incident light f. Therefore, the laser amplifier is a resonant device, with a resonant frequency and bandwidth determined by the lineshape function $g(f)$.

4. Gain Saturation

Consider the energy diagram of a two level system with a ground state energy level E_0 as shown in Figure 37. The levels 1 and 2 have overall lifetimes t_1 and t_2 respectively, for transitions to lower levels. If R_1 and R_2 are the pumping rates of the levels 1 and 2 respectively, then the basic Einstein's rate Equation (6.13) will be for level 2,

$$\frac{dN_2}{dt} = R_2(t) - A_{21}N_2 - W(f)\left[N_2 - N_1\right] - A_{20}N_2, \tag{6.20}$$

and for level 1,

$$\frac{dN_1}{dt} = R_1(t) + A_{21}N_2 + W(f)\left[N_2 - N_1\right] - A_{10}N_1, \tag{6.21}$$

where now $g_1 = g_2$ and $W(f) = s(f)I_f / hf$. Since the rates of transition are inversely proportional to the decay times and A_{20} is usually small, the last two equations can be rewritten as,

$$\frac{dN_2}{dt} = R_2(t) - \frac{N_2}{t_2} - W(f)\left[N_2 - N_1\right], \tag{6.22}$$

$$\frac{dN_1}{dt} = R_1(t) + \frac{N_2}{t_2} + W(f)\left[N_2 - N_1\right] - \frac{N_1}{t_1}, \tag{6.23}$$

where $t_2^{-1} = t_{21}^{-1} + t_{20}^{-1}$.

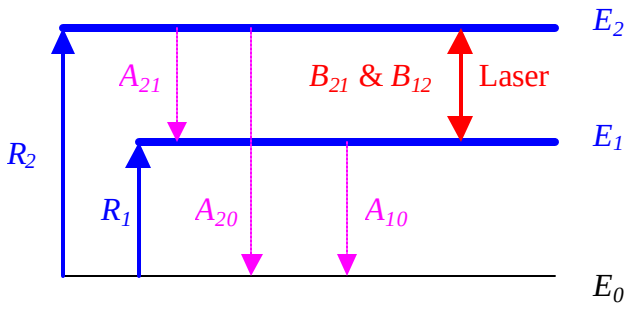

Figure 37. Two Energy Level 1 and 2 System with Ground State E_0.

For steady-state conditions of the populations of the levels 1 and 2, the last two equations for the population difference ΔN can be solved

$$\Delta N = N_2 - N_1 = \frac{R_2 t_2 - (R_1 + R_2) t_1}{1 + t_2 W(f)}. \tag{6.24}$$

At $t = 0$ there is no field, $W(f) = 0$ and the population difference at this time has its maximum value $\Delta N(0) = R_2 t_2 - (R_1 + R_2) t_1$, which represent the steady-state population difference in the absence of amplifier radiation. Therefore, in the presence of amplifier radiation the steady state population will become

$$N_2 - N_1 = \frac{\Delta N(0)}{1 + \frac{I_f}{I_s}}, \tag{6.25}$$

where $I_s = hf / s(f) t_2$ is the saturation intensity. When $I_f = I_s$, the population difference is one half the maximum value $\Delta N(0)$. As previously seen from the Equation (6.17), the gain coefficient is proportional to the population difference. Thus, the saturated gain coefficient $g(f)$ can be defined as

$$g(f) = \frac{g_o(f)}{1 + \frac{I_f}{I_s}}, \tag{6.26}$$

where $g_o(f) = \Delta N(0) s(f)$. It is obvious that the gain coefficient is a decreasing function of the intensity I_f. The saturation intensity is defined as the intensity that reduces the gain coefficient by a factor of 2.

5. Three and Four Level Lasers

A population inversion arises when more atoms are in a higher state of excitation than in a lower state. This can occur when the upper state has a longer lifetime. A large number of atoms can be excited and held in this state leaving an almost empty state below it. The atoms can stay in this metastable state while the population inversion is built up.

In reality, it is not possible to have lasing based on absorption and emission between only two energy states. For any pair of states, the rate at which the upper level is populated by absorption equals the rate at which atoms decay to the lower level by stimulated emission. Three or four energy levels schemes are used in practice to achieve a population inversion.

A three level system is shown in Figure 38. The atoms are pumped to the upper, short-lived level (E_2), which is called the pump level. A rapid spontaneous decay occurs from the pump level to the metastable level, which lies between the pump level and the ground state. Laser emission occurs between the metastable level and the ground state.

An improvement on this scheme is obtained with a four level structure which is shown in Figure 39. Laser transition takes place between the third and the second excited states. The depopulation of the highest and the lower laser level is rapid in order to ensure that always a population inversion exists.

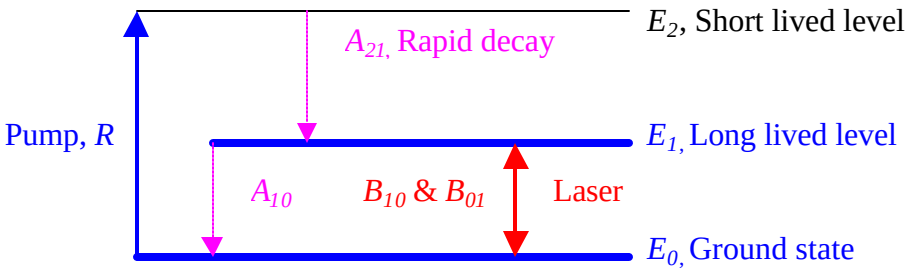

Figure 38. Three Energy Level System.

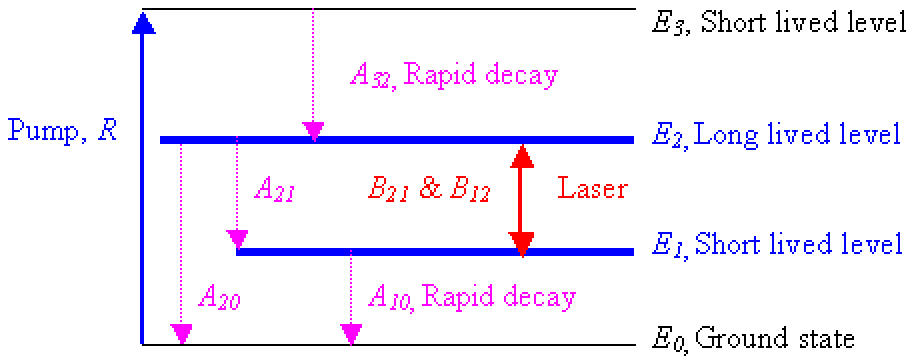

Figure 39. Four Energy Level System.

6. Optical Resonant Cavity

It has been demonstrated that to obtain light amplification from a given medium it is necessary to establish a population inversion between a chosen pair of energy levels and promote stimulated emission. This by itself is not enough to sustain laser action. The lasing medium must be bounded between two mirrors, of which, one is totally reflecting and the other is partially reflecting. This forms an optical resonant cavity where the light oscillates between the mirrors. The cavity provides a method of optical feedback where the light is reflected several times between the mirrors to enable further stimulated emission.

A cavity of length *S* supports only the modes such that *S* corresponds to integral multiples of half a wavelength. The resonator mode spacing due to the round trip phase shift is *c*/2*S*, where *c* is the speed of light in the medium. Furthermore, laser amplification can occur only for the modes of frequencies for which the signal gain coefficient $g_o(f)$ is greater than the loss coefficient a_r in the cavity. The coefficient loss expresses the total number of photons lost per unit length, and can be defined as [Ref. 17]

$$a_r = \frac{1}{t_p c}, \tag{6.27}$$

where t_p represents the photon lifetime. After a short time of laser operation, the gain saturates to *g(f)* and only a single or a few modes close to the central mode survive. Finally, all the emitted photons have the same wavelength, phase, and amplitude. The

process of mode competition is shown in Figure 40. The plot on the left shows that, when the laser is turned on, all the resonator modal frequencies for which the gain coefficient is greater than the loss coefficient (presented as blue lines) begin to grow, with the central mode growing at the highest rate. The modal frequencies for which the loss exceeds the gain are indicated as red lines. When the gain saturates, only a single mode survives as shown on the right plot.

The laser can support either a continuous wave (CW) beam or a pulsed beam. The pulsed laser beam is achieved either by controlling the pumping rate (gain switching) or by controlling the cavity losses (Q-switching). In a gain switching laser, the pumping rate is turned on and off periodically. In a Q-switching laser, the loss coefficient a_r is switched between a large value during the off time and a small value during the on time.

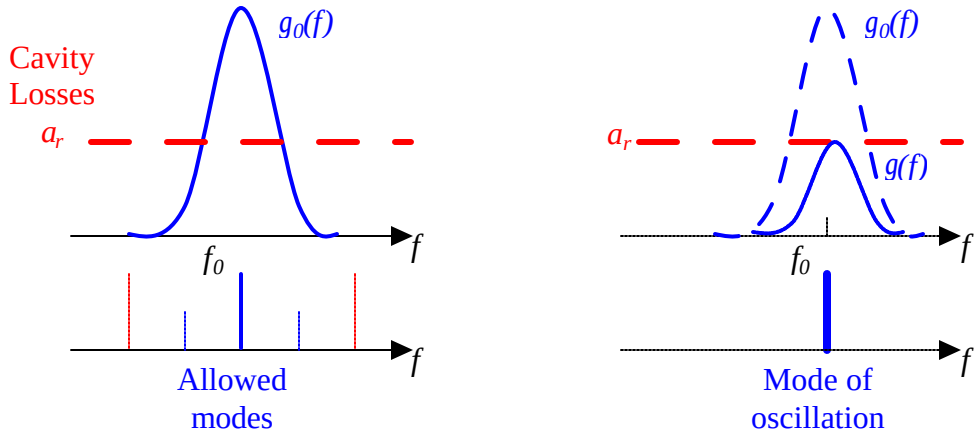

Figure 40. Mode Competition.

C. SOLID STATE LASER MATERIALS

This section will discuss some of the large number of solid sate materials that have the potential to be scaled to high average output power for military applications.

1. Nd: Lasers

Neodymium-doped laser materials are the most commonly used as they have a combination of properties uniquely favorable for laser operation. They are excited near 808 nm and emit near 1.06 μm .

The neodymium-doped yttrium aluminum garnet (Nd:YAG) laser, because of its high gain, is the most important. The YAG material is hard, of good optical quality, and has high thermal conductivity.

The Nd:YAG laser is a four level system. Under normal operating conditions at room temperature, the energy levels allow a transition at 1.0641 μm wavelength. However, it is possible to obtain lasing at other wavelengths either by inserting etalons or prisms in the resonator, or by designing a resonant reflector as an output mirror. A design and operation of a high power Nd:YAG laser oscillating at 1.3 μm has been reported. In the long pulse mode the laser has achieved an output up to 8 J per pulse at 5 Hz and up to 165 W of laser output at 50 Hz [Ref. 18].

Lithium yttrium fluoride lasing material has been improved and is suitable for many applications. The Nd:YLF has a relatively large thermal conductivity which allows efficient heat extraction, but less than Nd:YAG. Its excited state lifetime is twice as long as Nd:YAG. Since lifetime is a measure of the energy storage capability in Q-switched operation, Nd:YLF is currently being used in Q-switched laser amplifiers. The stimulated emission cross section area (6.14) for YLF is also half that of YAG. Depending on the polarization of the light, two wavelengths are obtained, 1.05 μm and 1.3 μm.

Another material is the neodymium-doped yttrium vanadate (Nd:YVO4), which has a large stimulated emission cross section area, five times higher than Nd:YAG, and a strong broadband absorption. The achieved high gain combined with the strong absorption allows us to use a crystal only a few mm in length. Pump absorption is polarization dependent. The strongest absorption occurs for pump light polarized in the same direction as the light propagation. However, the thermal conductivity is only half as high as Nd:YAG and somewhat lower than Nd:YLF. The excited state lifetime is also shorter than Nd:YAG. Therefore, the large cross section is partially offset by its shorter lifetime.

2. Yb: Lasers

Ytterbium-doped materials (Yb:YAG, Yb:FAP) have been known for years but were never considered interesting due to their low absorption and emission cross-

sections. Moreover, they appear to have a quasi-three-energy-level nature, since the terminal state can be thermally populated. By comparison, the separation between the terminal laser level and the ground state in Nd:YAG at room temperature is ten times bigger than in Yb:YAG. The crystal of Yb:YAG has only a single absorption line at 942 nm, which requires extremely high pump irradiance with conventional pump sources in the visible band to achieve lasing threshold. However, since bright diode-pump arrays of InGaAs are available, which emit at 942 nm, the Yb:YAG has become attractive.

The Yb:YAG is a quasi-three-energy-level laser amplifier and the wavelength of oscillation is 1.03 μm. Its performance is strongly dependent on the operating temperature and can be improved by cooling the crystal. In this way, the thermal population is reduced and the stimulated emission is increased. To accomplish this, the crystal is mounted on a heat sink, which could be cooled to low temperatures. Thus, laser efficiency and the cost of the pump source can be traded for overall system efficiency that includes power and refrigeration requirements.

Despite these difficulties, Yb:YAG has attractive properties and the potential for reaching higher output power than other materials. The thermal load generated in a laser medium is a great concern for high power scaling. A reduction in heat load can lead to higher power systems with good beam quality. A unique advantage of Yb:YAG is that, when pumped with an InGaAs pump source, it produces a smaller amount of crystal heating than any other known material. The required pump radiation in this material is only about one-third compared to Nd:YAG. Another unique advantage is that it has a broad absorption line at 942 nm, which is ten times broader than the 809 nm absorption line in Nd:YAG. It has also a long lifetime which reduces the number of pump diodes required for a given energy per pulse output. As will be seen, the pump diodes are power limited, and the long lifetime permits a long pump pulse, which generates high power output. In addition, the InGaAs family of diodes offers greater lifetime and higher reliability than any other diode family.

The obvious advantages of very low thermal load, broad absorption at the InGaAs wavelength, and long lifetime of Yb:YAG have raised the prospect of reaching high

average power. This feature has motivated the research and development of ytterbium-doped materials. Figure 41 indicates the progress in development of the Yb:YAG laser over the past few years.

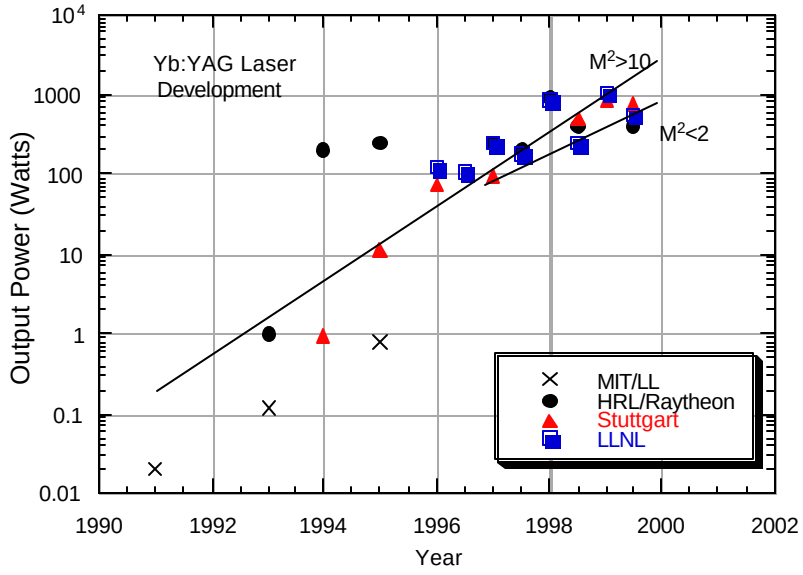

Figure 41. Output Power of Yb:YAG Lasers over the Past Decade. M^2 is a Representation of Beam Quality.(From [Ref. 2]).

D. SOLID STATE LASER PUMP SOURCES

The pump source of a solid-state laser emits radiation in a spectral region close to the absorption bands of the lasing material. The most efficient laser pump radiates at wavelengths that match the useful absorption band of the lasing medium. The pump source is supplied by electrical energy, either continuous or pulsed, which the pump converts into optical radiation. An optical system may be used to couple the radiation from the pump source to the laser medium.

Today, the pump sources that are of practical interest are flashlamps, cw arc lamps, and laser diodes. Coherent pump sources, such as laser diodes, permit concentration of the pump radiation into the active material with few losses. For lamp sources, only a fraction of the omnidirectional radiation can be concentrated into the active medium. Typical overall electrical efficiency for a lamp pumped laser is 1%, for an arc lamp about 3%, and for a diode pumped lasers 10-15% [Ref. 18]. Until recently, the

low power output, low packing density, and extremely high cost of diode lasers prevented any potential application of them. The rapid advances in laser diode technology have made the diode pump sources the most efficient method of pump.

Actually, flashlamps have higher radiation output to electrical input efficiency (70%) compared to laser diodes (30%). However, the diode pump is the most efficient way to produce population inversion in the laser material because there is an excellent spectral match between the output from the diode pump and the laser medium. This reduces the amount of heat deposited in the laser material and therefore leads to better beam quality. Since the output of a diode array is directional, the radiation can be transferred to the laser medium with little loss. Moreover, the diodes are coherent devices and their beams can be focused and adjusted to match the resonator modes of the laser, which in turn, leads to a high brightness laser output.

The diode pump can be configured in two ways: the side pump and the end pump. In the side pump geometry, the diode arrays are placed along the laser material while in the end pump geometry, the pump radiation is focused into the laser material collinear with the resonator mode.

Laser diode arrays have lifetimes on the order of 10^4 hours in cw operation or 10^9 shots in the pulsed mode [Ref. 2]. This is a critical factor as it influences the system lifetime and reliability. Moreover, new laser diodes, such as the InGaAs family, enable the use of laser materials such as Yb:YAG, which seems to be very promising for reaching high average power output.

Diode laser arrays have a major impact on the entire laser system's performance, cost, and reliability. Primary diode array characteristics are output power and duty factor, operating temperature and cooling, spatial and spectral characteristics, reliability, lifetime, and cost. Diode array performance is affected by the characteristics of the diode bars themselves, by the coolers on which they are mounted, and by the laser environment. Technological advances in these areas are required in order for solid-state lasers to realize their potential for directed energy weapons applications.

E. THERMO-OPTIC EFFECTS AND HEAT REMOVAL

The pumping process of the gain medium in the solid-state laser is associated with the generation of heat, causing various thermal effects. The thermal effects are considered the primary design problem for high average output power systems. The generation of heat in the laser medium during the pumping process is caused by:

- Quantum defect heating, which is the energy lost as heat to the lattice since there is an energy difference between the pump band and the upper laser level. In a typical laser system, the transition frequencies between these two levels fall within the frequency range of the vibration spectrum of the lattice. Therefore, these transitions are accomplished by direct nonradiative decay (emitting phonons), which leads to the generation of heat.
- Similarly, the energy difference between the lower energy level and the ground state.
- The fact that the quantum efficiency of the emission processes in the laser is less than unity. The quantum efficiency relates the number of independent ionic transitions to the number of photons generated by this process, and depends solely on the position of the energy levels [Ref. 18].
- The bw pump efficiency especially when arc lamps or flashlamps are used.

The heat from the pump radiation and the surface cooling of the laser medium cause a nonuniform temperature distribution across the laser medium. This temperature variation leads to a variation of the index of refraction and thermal effects such as thermal lensing and stress birefringence (induced birefringence that leads to beam depolarization). Both of these affect the laser beam quality. Moreover, thermal load causes stress on the material. If the temperature of the material exceeds its tensile strength, stress fractures occur in the medium.

A method to correct for thermal effects on the laser beam is the phase conjugation technique [Ref. 18]. Suppose a uniform flat wavefront which is distorted in the amplifier medium. An ordinary cavity mirror inverts the distortion as it reflects the beam, keeping the distortion fixed with respect to the propagation direction. With a second pass through the amplifier, the distortion is doubled. Using a phase-conjugate mirror, the distortion is reversed relative to the wave propagation direction. Thus, the same region of the

amplifier that created the distortion compensates it during the second pass through the amplifier.

Phase conjugation has been used successfully to correct the aberrations induced to the laser beam by thermal and stress effects for multi-pass, single solid-state amplifier configurations. In this area, TRW has already demonstrated clean-up of a 200 W average power beam [Ref. 2]. Still, there is progress to be made in using phase conjugation to combine multiple solid state amplifiers in phase in order to achieve high average power sources. Until now, Lawrence Livermore National Laboratory (LLNL) and Raytheon have independently demonstrated phase combining of four or more amplifier chains [Ref. 2].

There are several methods to remove the unwanted heat from the laser system such as liquid cooling, air or gas cooling, and conductive cooling. The cooling techniques remove the heat generated in the laser medium, pump source and laser cavity. In liquid cooling, the coolant flow is under pressure over the lasing medium and the pump source surface. Air or gas cooling is usually used for low average power lasers. In conductive cooling, a heat sink is mounted directly to the laser material and the heat is removed through conductivity.

Cooling is a very important process for laser operation, especially for a MW level solid-state laser. The role of the cooling process is obvious when considering the energy flow inside the system for a single engagement. An engagement using this type of weapon system requires an output of 1 megajoule (MJ) energy from the beam director. A typical laser medium is only 40% efficient, which means that the required energy from the pump source is 2.5 MJ. The pump source itself, as mentioned in the previous section, is expected to be 50% efficient. Thus, the electrical power supply should provide a total energy of 5 MJ. An energy flow diagram from the power supply to the laser output is shown in the Figure 42. From that figure, it can be seen that the cooling process should absorb 4 MJ unwanted heat from the weapon system components.

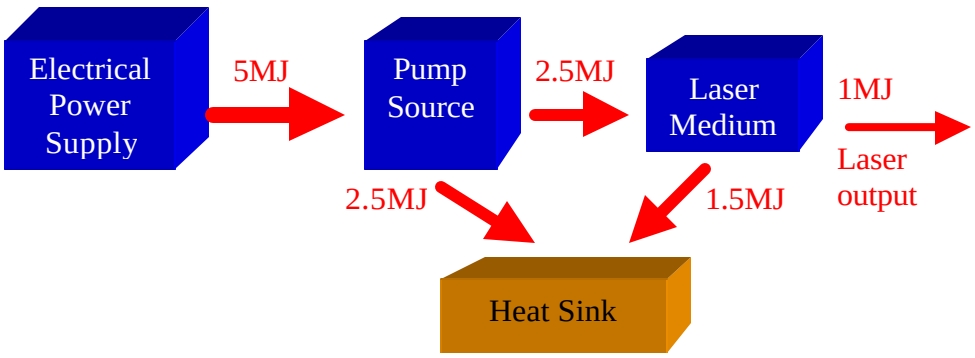

Figure 42. Energy Flow for a Single Engagement.(After [Ref. 2]).

F. HIGH ENERGY SOLID STATE LASER DESIGNS

A considerable amount of progress has been made over the last 15 years in scaling solid-state lasers to higher powers. Kilowatt average power levels are now routine and 10 kW output will soon be demonstrated. Systems at the 100 kW level are being designed today, and conceptual designs for MW level devices have been developed by multiple industrial sources.

Solid-state lasers with an average power of 0.1-10 kW are currently in use for many military applications. In addition to their typical role as designators and illuminators, lasers of this category can be used for countermeasures and sensor denial, but they are not generally considered directed energy weapon systems.

Solid-state lasers with an average power of 10-100 kW can place a sufficient amount of energy density on military targets to cause their destruction. However, at this power level, the lethal engagement of the target is limited to close ranges, especially when the laser weapon system has to accomplish its mission in the maritime environment.

Lasers with an average power of 100-500 kW are typically associated with high-energy laser weapons. The Theater High Energy Laser (THEL), developed for defense against Katyusha rockets, the Heat Capacity Laser being developed for use in the Army's Enhanced Area Air Defense mission, and the proposed Advanced Tactical Laser (ATL) are in this class. These types of lasers produce lethal energy fluence on a target during

short engagement times, at ranges from 3 to 50 km depending upon the target, engagement altitude and local atmospheric conditions.

Lasers with an average power of over 500 kW are of interest to the Navy for point defense against missiles, and for strategic applications for ballistic missile defense over long distances. The Airborne Laser and the Space-Based Laser fall into this class.

High power solid-state lasers can be grouped into four classes: diode lasers, fiber lasers, continuously cooled lasers and heat capacity lasers.

1. Diode Lasers

Diode lasers use a variety of semiconductor compounds and can be either electrically or optically pumped. Lasing has been demonstrated throughout the visible range and extends well into the mid-infrared wavelengths, with the highest achieved average powers in the near infrared band.

Single diode lasers, using special semiconductor architectures, have achieved power levels of 1 W in CW mode. In order to achieve high average power output, multiple diode amplifier chains must be used. Diode arrays have demonstrated more than 1 kW/cm^2 output intensity.

Incoherent beam combining (IBC) has been used successfully to couple multiple diode lasers. An experiment has demonstrated an output of 5 W with acceptable beam quality. Current research at the Air Force Research Laboratory (AFRL) is trying to scale the power output to multiple tens of Watts with good beam quality, and a laboratory demonstration is expected within the next years. However, this technology is still immature, and it remains to be seen whether it is a scaleable technology. The potential exists for achieving 60% efficiency with excellent beam quality by combining multiple diode emitters.

The Phase Integrated Laser Optics Technology (PILOT) program, conducted at AFRL during the late 1980s and early 1990s, demonstrated coherent phasing of 900 diode elements, but the total output power was less than 10 W. The PILOT research and development effort was discontinued, but similar phasing techniques may be applied to current fiber laser designs [Ref. 2].

2. Fiber Lasers

Low power versions of these lasers are commonly used in fiber optic communication systems. High power fiber lasers have become enabled by the development of fibers that have a doped core separate from the cladding. This configuration provides a much larger aperture coupling in the pump light, so higher pumping levels are achievable, which leads to higher average power output. Continuous wave cladding-pumped fiber lasers have achieved an average power exceeding 120 W and a conversion efficiency of diode pump light to output laser radiation exceeding 60%.

Figure 43 displays the different configurations of the fiber lasers. On the left, a conventional fiber amplifier is shown where an end diode pump process is configured. Separating the core from the cladding, a side pump process is accomplished as shown on the right. The fiber core is indicated as a red cylinder while the cladding is indicated as a yellow cylinder.

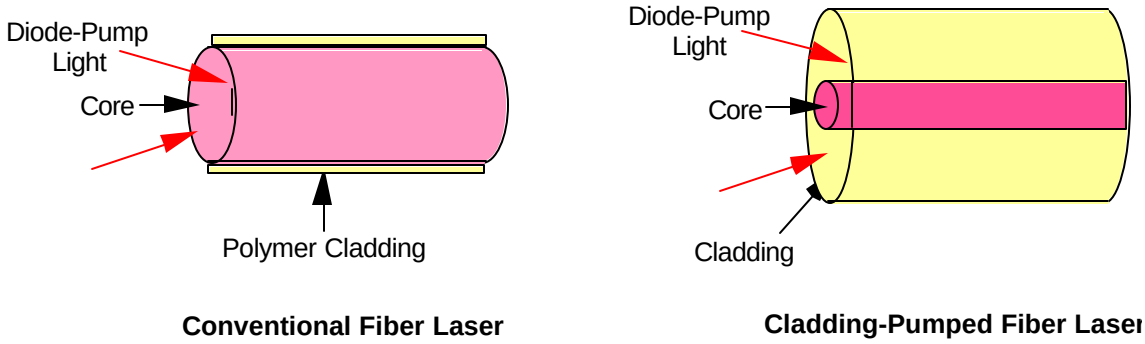

Figure 43. Conventional and Cladding-Pumped Fiber Laser Configurations.(From [Ref. 2]).

The potential of fiber lasers for directed energy weapons applications lies in two unique features:

- The central core can be designed as a single-transverse-mode waveguide
- the pump aperture of any individual fiber is on the order of 200 microns.

The single-transverse mode operation is achieved when the central core is limited to less than 10 microns. These small core fibers will produce diffraction-limited output, but are limited in power to approximately 100 W by nonlinear phenomena in the fiber such as Stimulated Raman and Brilluouin scattering. New methods of photonically

engineered fibers with a radially varying refractive index profile within the core offer the possibility of a larger single-mode.

By combining one thousand fibers, each carrying an average power of 100 W, a 100 kW laser system with a cross sectional aperture less than 1 cm^2 in area could be produced. However, at this point, it is necessary to deal again with the phase combining problem. Each individual fiber is an independent laser and, as a result, the output of the individual fibers adds incoherently. Thus, the fiber array indeed produces 100 kW output power, but in a highly divergent beam, with a time-dependent, random coherence. The brightness of the light beam of incoherently combined arrays will be limited compared to coherently combined arrays, but may still be sufficiently large to be valuable for some applications.

In Figure 44, an array of independent fibers produces a highly divergent beam, which is also a characteristic of a single fiber output with a very small aperture and a time-dependent speckle pattern. In the same figure, the desired output beam of the coherently phase combined fibers can be seen. In this case, the beam is free of speckle and exhibits the divergence characteristics of the effective aperture of the entire array.

The promise of fiber lasers for high-energy applications can be realized if the technology to coherently phase combine the output of individual fibers can be developed. This is an active research area in many laboratories. The state-of-the-art achievement is two low power fibers successfully phase-combined together producing a coherent output of 100 mW [Ref. 2]. However, in order to accomplish the goal of a MW output, phase combining of a large number of fiber lasers is required.

Figure 44. A Beam from an Array of Independent Fibers and a Beam from Coherently Phased Fibers.(From [Ref. 2]).

3. Continuously-Cooled Lasers

The continuously cooled lasers have already achieved over 1 kW output power. During their operation, the cooling process of the laser medium occurs simultaneously. Both the amplifier medium and the cooling method were discussed in previous sections. The most promising configuration, as demonstrated, is that using ytterbium-doped amplifier materials pumped by the InGaAs diodes. The phase combining of a large number of these apertures has the potential to achieve the desired output power for solid-state laser weapon.

4. Heat Capacity Lasers

The heat capacity laser has already achieved an output of 1.4 kW power at LLNL, and a power scaling up to 100 kW is expected in the near future. In contrast to the continuously cooled lasers, lasing and cooling occur separately in the heat capacity laser. With this method, there are two cycles of the laser operation: the lasing cycle followed by the cooling cycle. After each laser emission, which means a target engagement for the weapon design system, the cooling cycle removes the heat that has been deposited in the system. Typically, with current cooling technology, after an engagement of a couple of seconds, a cooling period of 1 to 5 minutes follows.

The heat capacity laser has been chosen for the Army's tactical high-energy laser (HELSTAR). The program is based on the solid-state heat capacity laser developed at LLNL. This type of laser operates in pulsed mode with a typical width of several hundred microseconds and a repetition rate of several hundred Hertz. In order to achieve the goal of 100 kW output power, a diode pumped design will replace the current flashlamp pumped laser system and Nd:GGG crystalline will replace the current amplifier material of Nd:glass.

G. CONCLUSIONS

In this Chapter the solid-state laser was studied. This laser also offers significant potential for a directed energy weapon system since it has already demonstrated a kW level output power. In order for solid-state lasers to realize their potential for directed energy application, promising laser designs, such as the fiber, continuously cooled and

heat capacity lasers must develop independent technologies dealing with the laser materials, pump process, thermal management and beam control.

Finally, the following Chapter summarizes the results presented in this thesis.

VII. CONCLUSIONS

High-energy laser (HEL) systems provide military units the opportunity to improve their capabilities and tactics in a variety of mission areas. A naval HEL application is anti-ship missile defense at a range much greater than that offered by currently used weapon systems. The Navy has supported research that is expected to arm future ships with free electron or solid-state lasers.

At the Naval Postgraduate School, a high power (MW level) FEL is being designed in collaboration with Jefferson Laboratory and Advanced Energy Systems. The designed FEL should have a small footprint and compact configuration in order to be placed onboard a Navy ship. To satisfy the size requirements, the size of the optical cavity is limited and the mirrors are vulnerable to the powerful optical beam. The use of a short Rayleigh length undulator may be the solution to the problem since it increases the spot size at the mirrors and leaves a small optical mode waist in the center of the cavity. For a small optical mode waist, a slight misalignment of the electron beam, either an offset or a tilt, reduces the overlap between the electrons and the optical mode in the interaction region, resulting in less gain and efficiency.

In this thesis, a three-dimensional simulation is used to demonstrate that the electron beam shift can change the optical wavelength, and reduce the peak efficiency as the electron beam is offset further from the undulator axis. It is found that the required efficiency for the 1 MW goal (0.7%) is achieved for electron beam shifts less than 0.3 mm, which is well beyond the experimental design tolerance of 0.01 mm. Electron beam focusing was also studied by varying the electron waist radius while keeping the total current fixed. This focusing enhances the overlap between the electron beam and the optical mode. It is found that the focused electron beam increases the extraction efficiency far beyond the desired value of 0.7%, and indicates that it may be possible to obtain MW operation at a lower average current. The induced electron energy spread for the focused beam is increased, but remains within the design goal of 15%.

The proposed FEL design operates in a pulse mode, producing optical micropulses 1 ps long at a pulse repetition frequency of $\Omega = 750$ Mhz. The pulse mode of operation leads to frequency spread depending on the FEL pulse shape in the time domain. Propagation of a broad-spectrum laser pulse through the atmosphere increases the power in frequency components where the absorption coefficient can be high. This increases the total absorbed power, which may cause thermal blooming. It is found that thermal blooming increase is not an issue for a moderately clear atmosphere when the stagnation zone size remains less than 10 m.

The TJNAF FEL can be upgraded to operate at 100 kW in the near future. It was shown that there is a slight improvement in efficiency with the use of a small negative step-tapered undulator, while the induced energy spread stays well below the 15% limit.

In the last chapter of this thesis, the solid-state laser was studied. This laser also offers significant advantages in the design of the directed energy weapon system. However, in order for solid state lasers to realize their potential for a directed energy weapons application, they must be developed as high average power, high energy pulse, lightweight, compact systems. In this area, technological advances are required in both the supporting technologies and the laser itself. The heat capacity laser is about to reach 100 kW showing tremendous progress, but this is still a laboratory device and not a field system. Moreover, the 100 kW average power is still not enough for the Navy's requirements for a megawatt class laser design.

LIST OF REFERENCES

[1] *Free Electron Laser Development for Naval Applications Workshop*, Workshop Report, Virginia, June 2001.

[2] *High Energy Laser Executive Review Panel*, DOD Laser Master Plan Vol. II, August 2000.

[3] H. Inteyan, "Evolution of High Brighteness SSL," TRW Space and Electronics, NPS Presentation, October 18, 2002.

[4] Roger D. McGinnis, "High Energy Lasers Efforts," PMS 405 Presentation, March 19, 2002.

[5] W. B. Colson, C. Pellegrini and A. Renieri , *Laser Handbook*, Vol. 6, North-Holland, Amsterdam, 1990.

[6] D. J. Griffiths, *Introduction to Electrodynamics*, Third Edition, Prentice Hall, New Jersey, 1999.

[7] W. B. Colson, Notes for PH 4911 (Simulation of Physical and Weapon Systems), Naval Postgraduate School, 2002 (Unpublished).

[8] R. D. McGinnis, "FEL Development for Directed Energy," PhD Dissertation, Naval Postgraduate School, Monterey, California, December 2000.

[9] T. S. Rappaport, *Wireless Communications*, pp. 229-232, Prentice Hall, New Jersey, 1996.

[10] L. W. Couch, *Digital and Analog Communication Systems*, Sixth Edition, Prentice Hall, New Jersey, 2001.

[11] W. B. Colson, A. M. Todd, and G. R. Neil, "FEL With Short Rayleigh Length," *Nucl. Instr. and Meth.* A483, pp. II-9 (2002).

[12] D. W. Small, R. K. Wong, W. B. Colson, and R. L. Armstead, "A High Power FEL Using a Short Rayleigh Length," *Nucl. Instr. and Meth.* A393, pp. 262-264 (1997).

[13] J. Blau, V. Bouras, A. Kalfoutzos, G. Allgaier, T. Fontana, P. P. Crooker, and W. B. Colson, "Simulations of High Power FEL with Strongly Focused Electron and Optical Beams," Accepted by *Nucl. Instr. and Meth.,* presented at the 25th International FEL Conference, Argone, IL, 2002.

[14] J. Blau, "Multimode Simulations of FEL," PhD Dissertation, Naval Postgraduate School, Monterey, California, March 2002.

[15] K. Polykandriotis, "Simulations of the Proposed 100 kW TJNAF FEL and Comparison With TJNAF Low Power Experiments," Master's Thesis, Naval Postgraduate School, Monterey, California, December 2001.

[16] J. Blau, V. Bouras, W. B. Colson, K. Polykandriotis, A. Kalfoutzos, S. V. Benson, and G. R. Neil, "Simulations of the 100 kW TJNAF FEL Using a Step-tapered Undulator," *Nucl. Instr. and Meth.* A483, pp. 138-141 (2002).

[17] E. A. Saleh and M. C. Teich, *Fundamental of Photonics,* J. Willey and Sons, New York, 1991.

[18] W. Koechner, *Solid-state Laser Engineering,* Fifth Edition, Springer, New York, 1999.

[19] J. T. Verdeyen, *Laser Electronics,* Third Edition, Prestice Hall, New Jersey, 2000.

INITIAL DISTRIBUTION LIST

1. Defense Technical Information Center
   Ft. Belvoir, Virginia

2. Dudley Knox Library
   Naval Postgraduate School
   Monterey, California

3. Professor William B. Colson, Code PHCW
   Department of Physics
   Monterey, California

4. Professor Phillip E. Pace, Code EC/PC
   Department of Electrical and Computer Engineering
   Monterey, California

5. Professor Joseph Blau, Code PHBL
   Department of Physics
   Monterey, California

6. Professor Peter Crooker, Code PHCP
   Department of Physics
   Monterey, California

7. Professor Robert L. Armstead, Code PHAR
   Department of Physics
   Monterey, California

8. Chairman, Physics Department, Code PHMW
   Naval Postgraduate School
   Monterey, California

9. Chairman, Electrical and Computer Engineering Department, Code ECPO
   Naval Postgraduate School
   Monterey, California

10. Engineering & Technology Curricular Office (Code 34)
    Naval Postgraduate School
    Monterey, California

11. CDR Roger McGinnis, USN
    Naval Sea Systems Command
    Washington D.C.

12. Dr. George Neil
TJNAF
Newport News, Virginia

13. Dr. Steve Benson
TJNAF/MS6A
Newport News, Virginia

14. Dr. Fred Dylla
TJNAF
Newport News, Virginia

15. Dr. Alan Todd
Advanced Energy System
Princeton, New Jersey

16. Dr. Dinh C. Nguyen
Los Alamos National Laboratory
Los Alamos, New Mexico

17. Professor Patrick G. O'Shea
Institute of Plasma Research and
Department of Electrical Engineering
Energy Research Facility, University of Maryland

18. Dr. Gil Graff
Office of Naval Research
Arlington, Virginia

19. Michael B. Deitchman
Office of Naval Research
Arlington, Virginia

20. LT Aristeidis Kalfoutzos H.N.
Athens, Greece